CFD modelling of air flow through a finned coil heat exchanger to improve heat transfer and pressure drop predictions

M Heystek

Orcid.org/0000-0003-4158-8173

Dissertation accepted in partial fulfilment of the requirements for the degree *Master of Engineering in Mechanical Engineering* at the North-West University

Supervisor:	Prof M van Eldik
Co-supervisor:	Dr PVZ Venter

Graduation:	May 2020
Student number:	23446870

Abstract

Keywords: CFD; Finned coil heat exchangers; fin profile, STAR-CCM+, parametric study

In the current study, a method of lessening computational expense and model design effort is investigated for finned coil heat exchangers (FCHXs) by using STAR-CCM+ as simulation tool. The simulation model prediction accuracy, in terms of the air side thermal-hydraulic characteristics of a staggered tube, true-to-industry (TTI) sized FCHX model, is compared to a repeatable, representative segment (RS) model of the same FCHX across a wide air flow continuum ranging between laminar to fully turbulent. The level of confidence of these models is validated based on a comparison with previous experimental data from a renowned source using the Colburn j-factor and Fanning friction factor (f-factor) as reference and illustrate a reasonable agreement. The RS model type is found to be a suitable approach, limiting computational expense compared to the TTI model, which showed a minor improvement of the heat transfer and pressure drop predictions by only 1.18% and 1.83%, respectively.

In order to reduce simulation model design effort in the next phase of the study, the model prediction results of a plain fin RS model are compared to a wavy fin RS model. Wavy fin FCHXs are commonly found in industry and create a few extra design challenges for simulation purposes when compared to a plain fin FCHX. The results of a plain fin RS model is found to yield large inaccuracies compared to the wavy fin RS model and beckons the need to parametrically test the effects of geometrically modifying a plain fin RS model in order to increase model prediction accuracy. Detailed analysis of the effect on the heat transfer and pressure drop performance is done by evaluating related parameters such as the fin pitch, longitudinal tube pitch and transverse tube pitch.

The increase in fin pitch is found to cause an increase in heat transfer performance (in terms of the Nusselt number) due to a substantial hydraulic diameter increase, although a decrease in the heat transfer coefficient and pressure drop is seen. A decrease in the longitudinal and transverse tube pitches causes an increase in heat transfer and pressure drop performance, whereby the effect of the transverse tube pitch is found to yield the closest results comparison in relation to the wavy fin RS model's results. The average prediction accuracy for the entire flow range was found for the heat transfer to be predicted with an error deviation of 3.22% and pressure drop of 4.44%, which was acceptably accurate.

Although the variation in transverse tube pitch proved to be acceptable for this study, more research has to be done in future to confirm this finding using a wavy fin model incorporating

a variation of waviness heights (and waviness angles) and a different set of geometrical parameters before a final conclusion can be made.

Acknowledgements

List of abbreviations and acronyms

CAD	Computer Aided Design
CFD	Computational Fluid dynamics
FCHX	Finned Coil Heat Exchanger
FIDAP	Fluid Dynamics Analysis Package
HVAC&R	Heating, Ventilation, Air Conditioning and refrigeration
HX	Heat Exchanger
LES	Large-eddy Simulation
MIT	Mesh Independency Test
RAM	Random Access Memory
RANS	Reynolds Averaged Navier Stokes
RS	Representative segment
SST	Shear Stress Transport
STAR-CD	Computational Dynamics
STAR-CCM+	Computational Continuum Mechanics
TTI	True-to-industry

Nomenclature

A	Heat transfer area $[m^2]$
A_{min}	Minimum free-flow cross-sectional area $[m^2]$
c_p	Specific heat capacity $[J/kg.K]$
d_c	Diameter where convection takes place $[m]$
D_h	Hydraulic diameter $[m]$
d_i	Inner diameter $[m]$
d_o	Outer diameter $[m]$
d_r	Effective fin diameter $[m]$
f	Fanning friction factor [-]
F_s	Fin spacing $[m]$
F_p	Fin pitch $[m]$
G	Mass velocity $[kg/s.m^2]$
h	Heat transfer coefficient $[W/m^2.\text{C}]$
j	Colburn j-factor [-]
k	Thermal conductivity $[W/m.K]$
L	Characteristic linear dimension $[m]$
L_1, L_2, L_3	Heat exchanger length, depth and height $[m]$
Nu	Nusselt number [-]
Δp_f	Friction factor pressure drop $[Pa]$
P_l	Longitudinal tube pitch $[m]$
P_{min}	Minimum free-flow cross-sectional perimeter $[m]$
P_t	Transverse tube pitch $[m]$
Pr	Prandtl number [-]
R	Direction of friction [-]
Re	Reynolds number [-]

St	Stanton number [-]
T	Temperature [℃]
T_H	Thickness of heat exchanger header [m]
t_f	Fin thickness [m]
U	Air free stream velocity [m/s]
v	Kinematic viscosity [$N.s/m^2$]
V	Air velocity [m/s]
V_n	Normal component of velocity [m/s]
W	Waviness [-]
y+	Dimensionless wall distance [-]
Δy	First node distance [m]

Greek symbols

α	Thermal diffusivity [m^2/s]
ρ	Density [kg/m^3]
σ	Free-flow area/frontal area [-]
τ	Viscous shearing force [N/m^2]
μ	Dynamic viscosity [$Pa.s$]
μ_∞	Free stream dynamic viscosity [$Pa.s$]
μ_+	Friction velocity [m/s]

Subscripts

air	Air
h	Height
H	Header
n	Normal
w	Wavy fin
∞	Free stream

Table of Contents

List of figures

List of tables

Chapter 1 : Introduction

1.1. Background

1.1.1. Heat transfer enhancement motivation

Various methods of heat transfer enhancement have been employed in an effort to produce more efficient heat exchangers (HXs) for well over a century. The study of enhanced heat transfer has gained serious momentum during recent years due to increased demands by industry for heat exchange equipment that is less expensive to build and operate than standard heat exchange devices (Stone, 1996). A strong motivation for the development of improved methods of enhancement is the savings in materials and energy use. It is imperative that the HXs are especially compact and lightweight when designing cooling systems for automobiles and spacecraft. Applications like these, as well as numerous others, have led to the development of various enhanced heat transfer surfaces (Stone, 1996).

Enhanced heat transfer surfaces can be used for three purposes. The first purpose is to make HXs more compact in order to reduce their overall volume, and possibly their cost. The second is to reduce the pumping power required for a given heat transfer process, and a third, to increase the overall UA (overall heat transfer coefficient) value of the HX. Manipulation of the UA value is possible in either of two ways: (1) to find an increased heat exchanger rate for fixed fluid inlet temperatures, or (2) to reduce the mean temperature difference for the heat exchange; this leads to an increased thermodynamic process efficiency, which can result in a saving of operating costs (Stone, 1996).

Passive and active enhancement techniques are the two categories most implemented in industry today. Passive methods require no direct application of external power and employs special surface geometries or fluid additives which cause heat transfer enhancement. Active schemes, on the other hand, requires external power for operation such as electromagnetic fields and surface vibration (Bergles, Webb and Junkan, 1979).

The most popular commercial enhancement technique used in industry today is the passive scheme (Stone, 1996). Problems that are associated with vibration or acoustic noise, and costs involved, have cause little commercial interest for active techniques (Kakaç, Shah and Aung, 1987). This study deals only with a passive enhancement technique on the gas-side with the focus on heat transfer enhancement using a wavy fin surface geometry.

1.1.2. Compact HXs and evaluation of heat transfer enhancement

In forced-convection heat transfer between a gas and a liquid, the heat transfer coefficient of the liquid may be 10 to 50 times greater than that of the gas. Specially-configured surfaces can be implemented to reduce the gas-side thermal resistance. This is the motivation behind the design of a category of HXs with reduced size and greatly enhanced gas-side heat transfer, which are referred to as "compact". A compact HX is defined as a HX which incorporates a heat transfer surface having a high "area density" (Stone, 1996).

There are many different techniques that can be used to make HXs more compact. Figure 1.1 shows three general types of extended surface geometries used to increase gas-side heat transfer coefficients with (a) being in the scope of this study (Bergles, Webb and Junkan, 1979).
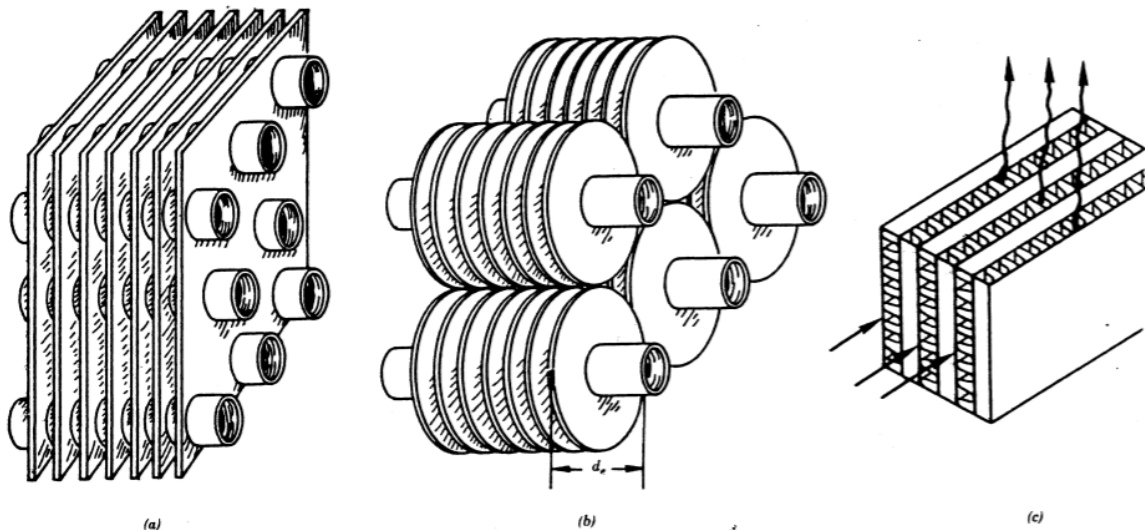
Figure 1.1: (a) Finned coil HX with flat fins, (b) individually finned tubes, (c) plate-fin HX (Bergles, Webb and Junkan, 1979)

In an industrial heat exchange application, one has a large number of options to choose from when considering a special surface geometry. How can one compare the performance improvement given by various enhanced surfaces? Certainly, the heat transfer coefficients, or dimensionless heat transfer parameters (i.e. Nusselt number, Colburn j-factor, etc.) yielded by each enhanced surface can be used to judge the relative heat transfer enhancement. But this will only give a partial indication of performance. Increased fluid flow friction and pressure drop are both the results of enhanced surfaces even though a greater heat transfer coefficient is generated. Sometimes, the benefits gained from heat transfer enhancement are not great enough to offset the increased friction losses (Bergles, Webb and Junkan, 1979). Clearly,

then, a minimum penalty on pumping power is of priority with the performance goal being to gain maximum enhancement of heat transfer. However, this balance is difficult to quantify in a manner that allows straightforward comparisons between enhanced surface geometries (Stone, 1996).

The basic performance data for an enhanced surface are often shown as curves of the Colburn factor, and the Fanning friction factor, plotted against the Reynolds number. Kays and London (1998) did experiments on a large range of different compact surfaces in one of the first comprehensive collections of data on enhanced surfaces for compact HXs (Kays and London, 1998, *3rd edition)*. The book of *Compact Heat Exchangers (1998)* has been considered one of the best references for HX and cold plate design since it was first published in 1955 (Lytron.com, 2019). Kays and London's Colburn and friction factor data have been used in many thermal design software programs and probably used by thousands of thermal engineers over the past five decades (Lytron.com, 2019).

1.1.3. Finned coil heat exchangers (FCHXs)

The continuous FCHX class is the type of compact HX this study will focus on being the popular choice in industry. FCHXs are widely used in the heating-ventilation-air conditioning and refrigeration (HVAC&R) industry. Compared to other types of HXs, FCHXs are easier and more cost effective to manufacture and to maintain. This makes it one of the most commonly used types of HXs in the industry (Lu *et al.*, 2011).

The capacity and configuration of FCHXs can be determined to accommodate application requirements for a specific HX. The construction of FCHXs involves using coil penetrated, wavy fin plates that are connected from start to finish. The fin plates might also vary in terms of waviness, since an increase in fin area impacts the thermal-hydraulic performance of the HX.

Each type of HX is classified according to the method of heat exchange between two or more fluids/gases. When considering an FCHX, the primary fluid flows through the coil and secondary fluid, typically air, flows over the fins perpendicular on the outside of the coil (Sun *et al.*, 2014).

Application specific parameters dictate the physical size of the HX needed. The layout and configuration of FCHX parameters such as the fin pitch, fin width, tube pitch and tube diameters impact the heat transfer and flow characteristics of the fluids. The fins can be plain, corrugated or wavy, perforated or louvered, and the tubes are typically circular, flat rectangular or elliptical (Kong *et al.*, 2016).

1.1.4. Computational Fluid Dynamics (CFD) history and modelling

Researchers have done a great number of studies on various aspects of FCHXs using CFD software as a simulation tool (Aslam Buttha *et al.,* 2012). The aspects that were investigated include the effects of varying component characteristics on air flow patterns, heat transfer areas and pressure drop across the HX.

The field of CFD has rapidly become one of the most powerful and effective tools to be incorporated in the testing and simulation of designs in today's industry. The first milestone achieved in the field of CFD was a 50-page paper written to the Royal society by Richardson (Richardson, 1910). In the study, hand calculations were done at a pace of 2000 operations per week. The development of CFD software as we know it today started in the early 1970's (Khalil, 2012). CFD software can be implemented to simulate various scenarios of fluid- or gas flows. It is widely used in industry including fields like Aerospace & Aeronautics, Automotive, Building HVAC, Chemical, Energy & Power Generation, Manufacturing & Process Engineering, the Oil & Gas Industry as well as Product Development & Design (Patel, 2013). As a mathematical summary, CFD is generalized as a numerical method for the calculation of nonlinear differential equations that describe fluid flow.

Implementation of CFD software has a big impact on saving time and money when used for project development and improvement. Addition of CFD in the development stage of a project or study enables early detection of design problems and in return drastically reduces the development time. An example of such a project is the design and development of Ilmor's Indycar engine which was developed approximately 50% faster with a reduced prototype cost of 75% (Tobe, 2019).

Therefore, CFD software has many advantages and can be a powerful item in an engineer's toolbox. The simulation accuracy, however, depends on the user's insight into the parameters of the project and his/her understanding of the simulation software used. Assuming that the mentioned criteria are met, a model must be designed not requiring a large amount of computational time to ensure that quick and effective model adjustments can be made (Pretechnologies, 2019).

1.1.5. Model complexity

For many years, there have been debates in the CFD community regarding the adequacy of model complexity when approaching different HX applications of the HVAC&R industry. At first glance, it may seem like a perfect solution to incorporate a True-to-industry (TTI) HX model with full complexity and complete in physical size to provide accurate results. In this study, a

TTI model will refer to the multi-channeled, multi-tube row and -fins model of the HX surface which closely resembles the type of FCHX as found in industry. In the beginning stages of CFD software, it had come to the attention of CFD users that a smaller, simplified or representative segment (RS) model might be simulated in applicable scenarios and has been moreover emphasised in the applications of modern-day problems. The RS model, therefore, serves as a computational domain selected as an encapsulated volume of the TTI FCHX model whilst being a repeatable (longitudinally or transversely) building block thereof. This method can provide a solution with acceptable accuracy to typical flow problems with computational expense kept at a minimum (Rossetti, Minetto and Marinetti, 2015).

On the other hand, over-simplification of a model can be done by not including complex fin patterns and using plain fins. This will impact the properties of the FCHX including heat transfer and pressure drop (Rossetti, Minetto and Marinetti, 2015). Further investigation is thus needed in order to sensibly adapt these simplification and parametric sizing techniques in compact HXs (specifically continuous FCHXs). After sufficient research has been done to prove the effectiveness of these techniques, the answers for creating less time-consuming simulation models will become more transparent.

1.2. Problem statement

The simulation of a TTI FCHX is computationally expensive and results in a longer convergence time. The need has been identified to investigate the effect of the implementation of a geometrically simplified, RS model on the accuracy of the air-side heat transfer and pressure drop predictions.

1.3. Purpose of this study

The focus of this study will be to investigate whether a TTI FCHX model can be geometrically simplified into a RS model; whilst still yielding an acceptable level of accuracy of the air-side thermal-hydraulic performance with regards to a trusted reference's TTI FCHX's experimental data.

Thereafter, whilst employing the outcome of a geometrically simplified model, the study will further determine the validity of simulating a geometrically modified plain fin model as a representation of a wavy fin model. The air-side heat transfer and pressure drop data of the wavy fin model will be used as reference to determine the validity of geometrically modifying a plain fin model.

1.4. Methodology

Kays and London, *Compact heat exchangers*, *3rd ed. (1998)* will be implemented as the experimental data reference for heat transfer and pressure drop. This is done as a measure of validation, as the resource is an internationally recognised book and the flagship of various compact HX test data as described in section 1.1.2. This reference will support the purpose of this study by providing accurate experimental test data.

The data presented for FCHXs in *Compact heat exchangers*, *3rd ed.* written by W.M. Kays and A.L. London (1998) illustrates experimental results for geometrically defined FCHX surfaces. These geometric parameters can be used to create an FCHX of any desirable volume, within the geometric constraints, by use of a geometric sizing method. This method involves choosing the number of tube rows and number of fins in order to adhere to application specific requirements. The Colburn j-factors and friction factors vs. Reynolds number experimental data illustrated within *Compact Heat Exchangers*, 3rd *ed.* (1998) are, therefore, applicable to any geometrically sized version of the represented HX surface with identical parameters.

In order to investigate whether the TTI model of a FCHX can be geometrically simplified into a RS model, a plain fin approach will be implemented as the available test data from Kays and London only consists of plain fin FCHX experimental data. Hence, to test the validity of a RS FCHX model approach, the accuracy of the simulation results between the TTI model and RS model, with the same geometric parameters, will be compared with reference to Compact heat exchangers, *3rd ed. (1998).* The simulations will make use of the same experimental input data, which is defined in the following chapters. To be within the scope of this study, the FCHX surface $8.0 - 3/8T$ from *Compact Heat Exchangers*, 3rd *edition (1998)* is selected.

The CFD approach in this study will be performed using STAR-CCM+ as the simulation tool, due to its all-inclusive processing capabilities, making it the only software needed to complete the required simulations.

After the validity of the RS model has been investigated and validated, the results will determine the approach used in the next phase of the study. If the RS modelling approach is proved as viable, plain and wavy fin RS FCHX models with the same design parameters will be simulated (with the only variation being the fin surface). If the prediction accuracy of the RS model is found to be less than acceptably accurate, TTI models will be implemented.

Due to the popularity of wavy finned FCHXs in industry, a further investigation of the study will entail the comparison of the heat transfer and pressure drop results between a geometrically

identical plain fin and wavy fin model (thus only varying fin surfaces). This comparison will give rise to a better understanding as to whether a plain fin model approach would suffice as an acceptably accurate representation of a wavy fin model's results. The geometrical parameters of the models will continue to resemble the geometry from *Compact heat excha*ngers, *3rd ed*. *(1998)*. The wavy fin's waffle height is selected to be a representation of a general value as found in industry defined by Panse (2005).

Due to the added complication of creating an FCHX with wavy fins with the exact profile in the design phase, a need has been identified to investigate a faster design method. Hence, this method will eliminate the need to design wavy fin profiles by implementing a plain fin model approach. It is then imperative to realize that the plain fin model approach can be expected to yield large inaccuracies with reference to a wavy fin model and therefore needs to be geometrically modified to yield acceptable accuracy.

This faster design method would then include varying related geometric parameters of the plain fin model, such as the fin pitch, longitudinal and transversal tube pitch in order to minimise result inaccuracies and is applied using a parametric approach. Each geometric modification includes three variations (chosen within model restrictions) whereby the effect on the heat transfer and pressure drop of each variation is evaluated and compared to the base plain and wavy fin model results.

The logic behind the parameter variation is to achieve the same nature of air flow which is created within the wavy fin FCHX model as the fin waviness leads to more turbulent flow; and ultimately more heat transfer and a higher pressure drop as penalty.

1.5. Study chapter layout

Table 1.1 illustrates the chapter layout of the study.

Table 1.1: Study chapters layout

Chapter	Heading	Short description
1	Introduction.	Introductory chapter.
2	Literature study.	Research of similar studies.
3	Computational model development and theory.	How the simulation model was constructed together with supporting background theory.
4	Full and segment models' validation, results and discussion.	Model validation, discussion and remarks of a true-to-industry scaled FCHX and scaled-down (both plain fins) comparison.
5	Model comparisons.	Attempt to replicate wavy fin model heat transfer and pressure drop results by modification of plain fin model design parameters.
6	Conclusion.	Final study conclusion.

In the following chapter, the literature that is applicable to the study's scope will be further discussed.

Chapter 2 : Literature study

2.1. Introduction

FCHXs' thermal-hydraulic performance has been the key focus of many CFD related studies over the last few decades due to the wide application of this HX type (Aslam Bhutta *et al.*, 2012). To generate a better understanding of the scope related work that has been done on this type of HX, a literature review is presented in this chapter.

The topics that are reviewed in this chapter are divided into two main groups, namely the effects of geometric parameter variation and simulation model related topics. Previous studies' findings with regards to geometric effects of the fin spacing, -thickness, -length, -profile, tube arrangement, -spacing, -rows and -diameter are reviewed. This is followed by the approaches implemented by previous studies with regards to simulation model topics such as the computational domain, mesh, turbulence modelling and steady or unsteady flow modelling.

2.2. Effects of geometric parameter variation

Following in this chapter, the findings of studies with a similar scope are grouped into the effect of each respective FCHX geometric parameter on the air-side heat transfer and pressure drop. Important aspects to note in terms of this study are the geometric effects of the fin spacing (2.2.1), fin profile (2.2.3) and tube spacing (2.2.5) as these aspects will be further investigated in Chapters 4 and 5.

2.2.1. Fin spacing

The fin pitch is connected by a widespread of studies to pressure drop and thus also the heat transfer performance. These studies have been done to find the optimal fin pitch and ultimately increase HX performance. An optimal configuration would thus have a high heat transfer with a low-pressure drop.

When Bhuiyan, Amin and Islam increased the fin pitch, both the heat transfer and pressure drop decreased, but the pressure drop decreased at a higher rate than the heat transfer. This caused a better FCHX efficiency in return when considering the effectiveness factor (j/f [$-$]). A decreased fin pitch resulted in a decrease in HX performance due to a more streamlined air flow. This was also found to be true by Karmo *et al.* in their study (Bhuiyan, Amin and Islam, 2013; Panse, 2005; Borrajo-Peláez *et al.*, 2010; Karmo, Ajib and Khateeb, 2013). Using flue gas instead of air, Erek *et al.* also saw that when the fin pitch was increased, the static and total pressure drops decreased (Erek *et al.*, 2005).

In the study of Romero-Méndez *et al.* it was found that the nature of the flow clearly changed as the fin pitch was varied. When the fin spacing was increased, vortices were formed and in the

downstream region of the tube, the wake was dominant. With an increase in fin spacing, a separation zone was formed behind the tube which was closed at first but opened up to the downstream fluid. It was found that the front of the tube participated much more in the heat transfer process than the back. The fin spacing where a peak was found for the Nusselt number at the horseshoe vortex strongly influenced the Nusselt number and pressure drop. The Nusselt number was very small in the wake region but experienced an increase when the fluid exchange with the downstream flow occurred (Romero-Méndez *et al.,* 2000).

The study from Lu *et al.*, found an optimum value for achieving the best thermal-hydraulic performance at 6-8 fins per inch at a fixed flow rate condition (Lu *et al.*, 2011). This is because higher fin pitch may have resulted in fully developed flow and deteriorated the overall performance, while a substantial rise of heat transfer caused by vortices and unstable air flow were observed when fin surfaces were considerably removed.

2.2.2. Fin thickness and length

Kong *et al.* tested the effect of fin thickness on the heat transfer of an FCHX. The study found that an increase in the thickness of the fins resulted in an enhanced heat transfer rate. When increasing the thickness, the extra cost of material needs to be considered as well as a higher pressure drop (Kong *et al.*, 2016; Lu *et al.*, 2011). It was also seen that the Nusselt number slightly decreased as the fin thickness increased (Borrajo-Peláez *et al.,* 2010).

Borrajo-Peláez *et al.* found that increasing the length of the fin caused the Nusselt number to decrease due to more aluminum that needed to be cooled. This in effect decreased the convection heat transfer coefficient (Borrajo-Peláez *et al.,* 2010).

2.2.3. Fin profile

Various studies were performed on the effect of different fin profiles and the effects thereof on air flow patterns. Increasing air turbulence has been linked to an increase in heat transfer performance but also in an increased pressure drop (Panse, 2005).

For wavy versus plain fins it has been found that the flow structure for plain fins comprises of flow recirculation zones that is located in the trailing edge of the tubes as air flows over the tubes. The wavy fin model showed no recirculation zones, since the flow is guided by the wavy corrugations. The plain fin model obtained a much higher percentage difference for the heat transfer and pressure drop characteristics between the staggered and in-lined tube configurations as compared to the wavy fin model (Panse, 2005).

In the study of Jang and Chen the wavy fin arrangement demonstrated a Colburn j factor and friction factor of $63 - 71\%$ and $75 - 102\%$ higher than the plain fin arrangement, respectively. For a four-row wavy fin arrangement the maximum Nusselt number was found on the second tube from the air

inlet while the Nusselt number for the plain fin arrangement decreased in order from the first to the fourth tube (Jang and Chen, 1997).

From the study of Gholami *et al.* the results revealed that the wavy fins could considerably advance the thermal efficiency of the FCHX with a slight pressure loss penalty. The computational results indicated that the average Nusselt number for the FCHX with wavy fins could be increased up to 20% over the baseline case and the corresponding pressure difference decreased up to 19%. The results also showed that the average value of performance in one wavy and three wavy fins and elliptical tube HXs increased up to 5% and 15% over the baseline case, respectively (Gholami, Wahid and Mohammed, 2017).

2.2.4. Tube arrangement

The tube arrangement of an FCHX plays a crucial role in the thermal-hydraulic performance. Studies have been performed to investigate the impact of a staggered tube arrangement versus an in-lined tube arrangement.

It was found that for laminar and transitional air flow, staggered tubes produced better flow mixing and therefore higher heat transfer and pressure drop characteristics than the in-lined arrangement (Bhuiyan, Amin and Islam, 2013; Jang, Wu and Chang, 1996).

In the study of Ay *et al.* the advantage of implementing a staggered tube configuration was made clear as the heat transfer coefficient was $14 - 32\%$ higher in the staggered configuration compared to the in-lined configuration (Ay, Jang and Yeh, 2002). Because of a better mixed air flow, smaller recirculation zones were obtained in the trailing edge of the tubes of a plain fin staggered tube arrangement than that of a plain fin in-lined configuration (Panse, 2005).

From Jang *et al.*, (1996), however, the pressure drop of the staggered tube configuration was $20 - 25\%$ higher than the opposing in-lined configuration (Jang, Wu and Chang, 1996).

2.2.5. Tube spacing

The tube spacing has been found to have a large impact on the heat transfer and pressure drop. An increase in the longitudinal- and transversal pitch caused a decrease in the heat transfer and pressure drop performance due to a less compact air flow (Bhuiyan, Amin and Islam, 2013; Panse, 2005). Bououd, Hachchadi and Mechaqrane, and Bhuiyan, Amin and Islam found that small transversal and longitudinal tube pitches presented a higher air velocity at the minimum flow area and a stronger flow disturbance which ensured better heat transfer with a higher pressure drop as a penalty (Bououd, Hachchadi and Mechaqrane, 2018, Bhuiyan, Amin and Islam, 2013).

2.2.6. Tube rows

The number of tube rows also contributes toward the overall HX performance. From the study of Panse as well as Tutar and Akkoca it was found that for wavy fin staggered tube configurations that the effect of the number of tube rows becomes very little beyond four rows. When the tube rows are increased from 1 to 6, an increase in pressure drop is seen to occur without any effect on the heat transfer for more than 4 tube rows. A four-row tube configuration may be regarded as the optimum choice for the balance between heat transfer and pressure drop performance (Panse, 2005; Jang, Wu and Chang, 1996; Tutar and Akkoca, 2004).

2.2.7. Tube diameter

Kong *et al.* tested the effect of the tube diameter and found that an increase in the diameter also caused an increase in heat transfer and pressure drop (Kong *et al.,* 2016). In the study of Borrajo-Peláez *et al.* it was seen that a bigger tube diameter increased the convection heat transfer and caused a growth in the Nusselt number. The mechanical performance, however, decreased as the friction coefficient grew drastically (Borrajo-Peláez *et al.,* 2010). Lu *et al.* also concluded that an increase in tube diameter resulted in decreased FCHX performance (Lu *et al.*, 2011). In a study done on much larger tube diameters, Bououd *et al.* also found that the heat transfer increased by 67% when the tube's external diameter was increased from 20mm to 35mm (Bououd, Hachchadi and Mechaqrane, 2018).

2.3. Simulation model aspects

Following in this chapter, the modelling approaches of studies with a similar scope are grouped. All aspects mentioned in this section are important to ensure acceptably accurate simulations are created within the following chapters.

2.3.1. Computational domain

The computational domain is the main control volume used for simulations in the chosen CFD program. The boundary conditions, physics, mesh, etc. are applied to this volume/area where all processing by the software code takes place. It is important to have a visual of the domain, as it serves as a platform to better understand the simulation process and provide an interpretation of the results. The domain is constructed using Computer Aided Design (CAD) software like Solidworks, AutoCAD Inventor etc. or can be internally constructed using a CFD package.

In order to save simulation time, many studies created only a RS model of a TTI scaled FCHX. These studies include: Tahseen, Ishak and Rahman, 2015; Borrajo-Peláez *et al.,* 2010; Lu *et al.*, 2011; Erek *et al.*, 2005; Romero-Méndez *et al.,* 2000; Bhuiyan, Amin and Islam, 2013; Panse, 2005; Jang,

Wu and Chang, 1996; Tutar and Akkoca, 2004; Khudheyer, *et al.,* 2011; Darvish Damavandi, Forouzanmehr and Safikhani, 2017 etc.

2.3.2. Mesh

Creating a mesh for the specified domain is one of the most critical aspects of running a successful simulation. Failure to generate the correct mesh with the correct cell sizes may cause divergence of the residuals and ultimately produce inaccurate results (Sadrehaghighi, 2019). Making use of different meshing software brought about a wide variety of meshing techniques and approaches that was utilized by different studies.

The CFD software generates a grid that is applied to the domain which divides the domain geometry into much smaller non-overlapping volumes referred to as cells. The meshing operator decides whether the cells are tetrahedral, hexahedral, etc. depending on the objective of the simulation and geometric shapes. Polyhedral cells are in most cases the best option (Ferguson, 2005). It is a general rule that the smaller the cells generated with meshing, the more accurate the final results; considering the correct cell types are used (Mavriplis, 1995). In return, creating smaller cells means that more cells are needed to fill the entire geometry volume which requires considerably more computational resources to facilitate. In order to ensure a balance is in place between model accuracy and the number of cells used, a mesh dependency test needs to be created and evaluated in the initial stages. The different meshing techniques from a few studies are shortly discussed below.

Bhuiyan *et al.* created a mesh of unstructured-triangular cells that was aligned with the direction of flow in order to reduce false diffusion. Coarser mesh cells were adopted in the extended areas in order to conserve computational resources. A gradual variation in cell size in and after the fin region was implemented to avoid the undesirable effect of a sudden grid width change (Bhuiyan, Amin and Islam, 2013).

Romero-Méndez *et al.* used eight node brick elements with linear interpolation to mesh the domain that was created. The nodes in the mesh were renumbered using the Renumber command within the CFD code (FIDAP) for a reduced size of the global coefficient matrix (Romero-Méndez *et al.,* 2000).

Erek *et al.* created the mesh using four hexahedral volume elements along the thickness of each half fin and twenty elements in the air region in between. The domain was designed and meshed using Gambit and was then exported to Fluent (Erek *et al.*, 2005).

In the study by Borrajo-Peláez *et al.* the mesh was divided into different zones. This step was done to avoid distortion of the elements that form the grid since distortion has a negative influence on the convergence, stability and computing time of the numerical simulations (Borrajo-Peláez *et al.,* 2010). The type of mesh cell that was implemented was not mentioned.

Lu *et al.* implemented an unstructured grid system that was generated using the "Auto mesh" function provided by simulation software STAR-CD for the air-flow channel. The solid part was meshed using a structured grid (Lu *et al.,* 2011).

Yashar *et al.* found that the geometric spacing pattern with the best accuracy had a geometric transition factor of 1.25. Fine nodes were used closest to the FCHX wall for the upstream and downstream air regions (Yashar *et al.*, 2011).

Karmo *et al.* tested more complex shaped fins and had to make use of a quadrilateral mesh. Grid refinement was also required in areas where steep gradients could occur (Karmo, Ajib and Khateeb, 2013).

Sun *et al.* implemented hexahedral shaped cells to mesh the domain. The areas near the tubes were refined to compensate for possible temperature gradients and high velocities (Sun *et al.,* 2014).

Yaïci *et al.* used an optimised solution-adaptive mesh refinement to predict the air flow field behaviour. More cells were added at locations where substantial flow changes were expected, for example near the walls. The calculation domain was half of the body based on symmetry considerations. Using unstructured grids mesh generator, the final mesh was composed around 1×10^5 elements (Yaïci, Ghorab, and Entchev, 2016).

Lui *et al.* implemented a pave mesh scheme in the fin planes except near the tube wall. At the region next to the tube walls, a map refined mesh was used to accurately calculate the viscous effects of the boundary layer. The square and simple upstream and downstream regions were meshed using a structured map mesh scheme. The computational domain was discretised by nonuniform grids with the grids of the fin coil region being finer and those in the extension domains being coarser (Liu, Yu and Yan, 2016).

Jabbour *et al.* created a polyhedral mesh that allowed identification of the physical phenomenon that exists on the inside of the FCHX segment. The tube thickness was divided into 4 to 7 cells, and the junction between the tube and fins was divided into 4 to 7 cells in width and 2 to 6 cells in height. The air was meshed using refinement around the tubes and fin leading edges to detect the physical phenomena that took place in these regions (Jabbour *et al.*, 2019).

Ünal, Atlar and Gören applied a non-matching block-structured mesh arrangement with quadrilateral elements as proposed by Lilek *et al.* This allowed the generation of smaller sub-domains to obtain a more effective mesh. In order to accurately resolve the boundary layer and the viscous sub-layer, particular attention was paid to the fluid region around the tubes. An O-type mesh structure was applied to achieve the required density for high-resolution demanding flow gradients. A fine H-type mesh was applied for the far wake region in order to resolve the effect of the Karman Street, and finally, the remaining region of the domain was constructed with a much coarser H-type mesh (Lilek *et al.*, 1997).

2.3.3. Turbulence modelling

Modelling turbulence can be one of the most daunting tasks and is still not fully understood (Solmaz, 2019). The accuracy of a simulation is very dependent on the choice of turbulence model and has been the topic of many studies (Ünal, Atlar and Gören, 2010). It is thus essential to choose the most appropriate flow model (laminar or turbulent) when simulating a certain flow regime.

Sodja found that using a RANS (Reynolds Averaged Navier-Stokes) turbulence model drastically reduced the computational costs required by solving the averaged equation system. It was proved that LES (Large-eddy Simulation) was not as efficient as a RANS turbulence model as RANS models have a computing time of only about 5% of the LES models (SODJA, 2019).

Various studies have found that when predicting both the friction factor and heat transfer, the laminar flow model produced the most accurate results within the laminar flow regime and the k-ω turbulence model was more accurate in the transitional- and turbulent flow regimes due to a better wall treatment (Panse, 2005; Khudheyer, *et al.,* 2011; Darvish Damavandi, Forouzanmehr and Safikhani, 2017; Jabbour *et al.,* 2019; Hansen, 2008).

From the study of Ünal, Atlar and Gören the SST (k-ω) model predicted the flow field characteristics of a near-wake region across a circular cylinder in turbulent flow the most accurately (Ünal, Atlar and Gören, 2010). The qualitative and quantitative comparisons revealed more successful predictions for the adverse pressure gradient, a massive flow separation, and vortex shedding than any other turbulence model.

In some studies, the k-ε turbulence model was chosen for heat transfer- and pressure drop simulations of turbulent flow due to the model's good convergence rate and being less memory-intensive (Khudheyer *et al.,* 2011; Sun *et al.,* 2014). This Turbulence model does not, however, perform well in the area close to the wall (Jousef, 2019).

2.3.4. Steady- and transient flow

The selection of a steady- or transient flow has a very large impact on the convergence speed of the simulation and requires the user to have experience in the field. The steady flow model is implemented when simulating constant flow and heat transfer regimes that do not vary with time and requires steady flow phenomenon, constant boundary conditions and constant device (in this case, the HX) behaviour. The transient flow model is implemented when simulating time-varying flow and heat transfer through an iterative implicit process at each time step.

If the simulation absolutely requires the implementation of a transient flow model the convergence of the simulation would be increased by an extensive amount and ultimately defeat the purpose of

this study. Simulations for flow from $Re > 3500 \, to \, 4000$ was found to require unsteady implicit simulations and was therefore not done in this study due to prevent extra computational expense (Fjallman, 2013). Experience in the field would indicate to the user whether or not such a model is necessary and could therefore only be implemented once the criteria are met whilst running the simulations.

Numerous studies were investigated for the use of the steady- and/or unsteady models and the majority were found to implement the steady state flow model (Bhuiyan, Amin and Islam, 2013; Bououd, Hachchadi and Mechaqrane, 2018; Jabbour *et al.*, 2019; Jang and Chen, 1997; Kong et al., 2016; Panse, 2005; Romero-Méndez *et al.,* 2000; Tahseen, Ishak and Rahman, 2015).

In the next section, a brief description of the experimental setup and testing procedure used for the applicable FCHX surface from *Compact heat exchangers, 3rd ed. (1998)* is given. This will serve as a guide to a better understanding of the validation process followed in Chapter 4.

2.4. Kays and London test system and procedure

This section will provide a basic understanding of the testing equipment that was used; and procedures that were followed in 1949 by the authors of the book, *Compact Heat Exchangers, 3rd ed. (1998)*. This set of experimental data is later used in this study as a form of reference in order to perform a reliable validation of simulation results. It is therefore important to replicate the experimental conditions (i.e. the tube wall temperatures, air flow range, air inlet temperatures, etc.) as closely as possible.

The heat transfer characteristics of a HX surface, for application to fluids, can be expressed by the conventional nondimensional relation of the Colburn j-factor versus Reynolds number. The friction characteristics can be generalised using the Fanning friction factor versus Reynolds number. Air can be used as a test medium, and the relations given by the experimental results allow extrapolation to be done to any fluid for which the necessary properties are known (Kays & London, 1950).

Kays and London considered many different testing techniques, including transient and steady-state heat transfer techniques. The technique that was best suited for the testing procedure was a steady-state system implementing condensing steam on the one side of the test core. The steam side was set at a sensibly uniform temperature with a thermal resistance generally less than 5 – 10 per cent of that of the air side.

Figure 2.1 illustrates the testing diagram for the experiments performed by Kays and London.

1   PIEZOMETER RING
2   INSULATED DUCT 12 X 13 IN.
3   JUNCTION BOX FOR THERMOCOUPLE LEADS
4   SELECTOR SWITCH
5   BROWN PRECISION INDICATOR POTENTIOMETER
6   CORE DOWN STREAM THERMOCOUPLES
7   TEST SECTION
8   INTAKE AIR THERMOCOUPLE
9   AIR DUCT, NOT INSULATED 8.5 X 9.75 IN.
10 DRAFT GAGES
11 AIR DUCT ENTRANCE SECTION 28 X 32.62 IN.
12 FAN, 16 IN.
13 WIRE SCREEN, 16 MESH
14 AIR FLOW STRAIGHTENING SECTION

Figure 2.1: Experimental setup (Kays and London, 1950)

The authors of the study stated that a steam system was provided to supply slightly superheated steam to the test core (point nr. 7 on diagram), and instrumentation was provided so that the energy loss of the condensing steam could have been measured and compared to the separately determined energy gain of the air. The energy balance, therefore, provided a continuous partial check on the accuracy of the instrumentation (Kays & London, 1950).

Test data for air flow between $800 \leq Re \leq 8000$ and an inlet temperature of $30°C$ were tested together with steam temperatures varying between $105°C \leq T_{steam} \leq 115°C$. The steam was provided to the test core using the setup illustrated in Figure 2.2.
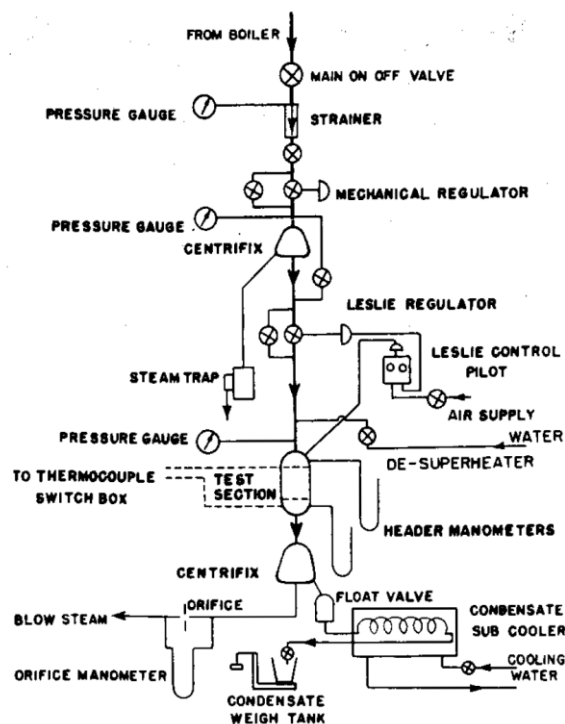
Figure 2.2: Steam system (Kays and London, 1950)

The wet steam for the steam system was generated in a boiler at a pressure which could be regulated from 30 to 100 psig. The steam then entered the regulatory system at boiler pressure. The steam was strained where the pressure was reduced to between 15 and 30 psig removing most of the liquid phase in a centrifugal separator. A small amount of water was injected to provide a close control on the desired 3 to 5°F superheat on entry to the top of the test core. A considerable excess of "blow" steam was passed through the core to prevent the build-up of a thick film of condensate on the transfer surface (Kays & London, 1950).

2.5. Summary

In summary, the information that was retrieved from the examined studies assisted in identifying an appropriate simulation methodology and selection of the best suited FCHX model parameters implemented in this study. Model construction of both the TTI model as well as RS models will be done using the same key aspects. The following is a summary of the physical model parameters and simulation model characteristics that will be constructed and chosen in Chapter 3:

Similar to most studies, the air flow range will be between $100 \leq Re_H \leq 3100$ (air velocities ranging between $0.3 \, m/s < v_{air} < 10.5 \, m/s$ depending on the model) as exceeding this range will start causing inaccuracies due to a lack of communication time between neighbouring mesh cells within the air flow. To counter these inaccuracies would require the simulation to be done using an Implicit unsteady approach, but doing this would slow the residual conversion speed drastically. The simulation will thus be chosen as "steady" which implies that an implicit unsteady model will be avoided due to longer convergence times.

Using the information obtained in the literature study from section 2.2.3, it is clear that the heat transfer and pressure drop values increase as waviness is added to the fins. The geometrical parameters of the plain fin model (fin pitch, longitudinal and transversal tube spacing) will therefore be adjusted using a parametric approach to reproduce the heat transfer and pressure drop results of a wavy fin model as stated in Chapter 1. The ideal method of inducing more turbulence within the plain fin model is by implementation of an increased fin pitch, and a decreased longitudinal and transversal tube pitch as literature have found.

One of the most important aspects to take into consideration for the study is that of the mesh. This is a critical part of the study as when not performed correctly, will produce erroneous results. The mesh type to be used depends on the complexity and thickness of the fins being simulated. This has been chosen to be a mesh of Polyhedral type cells due to a faster convergence rate and less cells required as compared to hexahedral and tetrahedral cells, as well as prism layer mesh cells next to the predefined walls (Jabbour *et al.*, 2019; Symscape, 2019). Refinement is required using smaller

cells in areas where steep gradients can be expected and prism layer cells between the air- and fin regions in order to capture the thermal boundary layer. It is also critical to perform a mesh independency test (MIT) to ensure the simulations can be run as effectively as possible.

A steady-state flow will also be implemented with all simulations in Chapter 4 and 5 as previously mentioned. The turbulence model that will be implemented is the SST (k-ω) model which is a sub-group of the RANS models. Being very important to the scope of this study, the heat transfer and pressure drop characteristics must be captured at an acceptable accuracy level in regions such as the near-wake of the tubes and the air-fin boundary layers. This turbulence model will thus be the best approach as indicated by Panse, 2005; Khudheyer *et al*., 2011, Darvish Damavandi, Forouzanmehr and Safikhani, 2017 and Jabbour *et al*., 2019.

In the next Chapter, the development of the models is discussed together with the accompanying background theory.

Chapter 3 : Computational model development and theory

In the previous chapter, a literature study was performed to get an extensive insight into some work that has already been put into the CFD simulations on continuous FCHXs. Following in this chapter, the development of the computational model and rationale thereof is discussed to ensure a coherent understanding. Then, where applicable, the relevant background theory associated with certain simulation models is provided.

The following section describes relevant dimensionless numbers important to assist in comprehending previous studies performed within the field, and the simulation results as depicted in Chapters 4 and 5.

3.1. Reynolds number, Colburn j-factor and Fanning Friction factor f

The validation in Chapter 4 is performed by creating two plain fin models (a TTI FCHX model and a representable segment thereof; RS model) according to the dimensions (surface $8.0 - 3/8\,T$) as found in *Compact heat exchangers (Kays and London, 1998, 3rd edition);* an internationally recognised source. The validation will be done using an experimental test result graph which comprises the Colburn-j factor and friction factor f versus the Reynolds number.

The Colburn j-factor, also known as the Chilton-Colburn j-factor analogy, is one of the most successful analogies used today defining the relationship between heat, momentum and mass transfer. As part of the dimensionless group, the Colburn j-factor is classified as a "modified Stanton number to take into account the moderate variations in the Prandtl number for $0.5 < Pr < 10$ in turbulent flow" (Shah and Sekuliâc, 2012). It is defined as

$$j = St \cdot Pr^{2/3} = \frac{Nu \cdot Pr^{-1/3}}{Re} \tag{3.1}$$

Where St is the Stanton number (equation 3.2), Pr the Prandtl number (equation 3.3), Nu the Nusselt number (equation 3.4) and Re the Reynolds number (equation 3.5). These dimensionless numbers will be briefly discussed.

The Stanton number is used to represent the heat transfer coefficient without dimensions, thus being part of the dimensionless group. The Stanton number is the ratio of convected heat transfer (per unit duct surface area) to the enthalpy rate change of the fluid reaching the wall temperature (Shah and Sekuliâc, 2012). The primary advantage of the j-factor is its use in determining the heat transfer coefficient (found in equation 3.2) in the design and performance prediction of HXs, particularly compact HXs. It is defined as:

$$St = \frac{h}{G\,c_p} = \frac{h}{\rho u_{max} c_p} \tag{3.2}$$

Where h is the heat transfer coefficient, G is the mass velocity, C_p is the specific heat capacity and U_{max} is the maximum free-flow velocity.

Comprehension of the heat transfer coefficient h is critical as it serves as an important connection between the simulation results and the Colburn *j*-factor for the FCHX airside. The heat transfer coefficient is a quantitative characteristic of convective heat transfer between a fluid medium (air and water) and the surface (aluminium fins and copper tubes) covered by the fluid (Kurganov, 2019).

The Prandtl number is used solely as a fluid property modulus and is defined as the ratio of momentum diffusivity to the thermal diffusivity of the fluid:

$$Pr = \frac{v}{\alpha} = \frac{\mu c_p}{k} \tag{3.3}$$

Where v is the kinematic viscosity, α is the thermal diffusivity, μ is the dynamic viscosity and k is the thermal conductivity.

It is important to note the range of Prandtl number for different substances, with gases' range being applicable to this study (Shah and Sekuliâc, 2012). See Table 3.1 below:

Table 3.1: Prandtl range for various substances (Shah and Sekuliâc, 2012)

Prandtl number range	Substance
$0.001 - 0.03$	Liquid metals
$0.2 - 1$	Gases
$1 - 13$	Water
$5 - 50$	Light organic liquids
$50 - 10^5$	Oils
$2000 - 10^5$	Glycerine

The Nusselt number is also a dimensionless representation of the heat transfer coefficient. It is defined as the ratio of the convective conductance h to the pure molecular thermal conductance k/D_h for an internal flow:

$$Nu = \frac{h}{k/D_h} = \frac{h\,D_h}{k} \tag{3.4}$$

Where D_h denotes the hydraulic diameter.

When predicting fluid flow patterns, the dimensionless Reynolds number (Re) plays a prominent role in foreseeing the patterns in a fluid's behaviour (Simscale.com, 2018). The three flow regimes, known as laminar-, transitional- and turbulent flow, can be predicted using the Re number whilst using the hydraulic diameter (D_h) as reference. By calculating the Re number in advance, one can determine which numerical flow model to implement as the Re number is seen as one of the main controlling parameters in all viscous flows. It is defined as the ration of the inertia forces to the viscous forces, or

$$Re = \frac{inertia\ forces}{viscous\ forces} = \frac{GD_h}{\mu} \tag{3.5}$$

And,

$$G = \frac{\rho_{air}.U_\infty}{\sigma} \tag{3.6}$$

D_h is defined as

$$D_h = 4\frac{A_c}{P_c} \tag{3.7}$$

Where A_c is the minimum free-flow cross-sectional area, regardless of where this minimum occurs (Kakaç, Liu and Pramuanjaroenkij, 2012). L is defined as the flow length of the HX matrix, ρ_a defines the air density and P_c is the minimum flow passage perimeter. Once the Reynolds number is determined, the heat transfer coefficient and friction factor f can be calculated. In Chapter 4, the Reynolds number is calculated using the hydraulic diameter method as *Compact Heat Exchangers, 3rd ed. (1998).* This is changed in Chapter 5 whereby the fin spacing is used as the hydraulic diameter. Panse (2005) also used this method to calculate Reynolds numbers.

The flow patterns over the fin- and tube surfaces depend on the Reynolds number. Capturing these flow patterns is essential to running successful simulations due to the impact thereof on heat transfer and pressure drop. The choice of laminar/turbulent models and meshing strategies that will capture these flow patterns within the boundary layer are further discussed in sections 3.3 and 3.4.

Various occurring flow phenomena for different Reynolds numbers (Re_D) over tubes are illustrated in figure 3.1 below. These flow patterns and vortices are expected to be seen in the simulation results of Chapters 4 and 5.
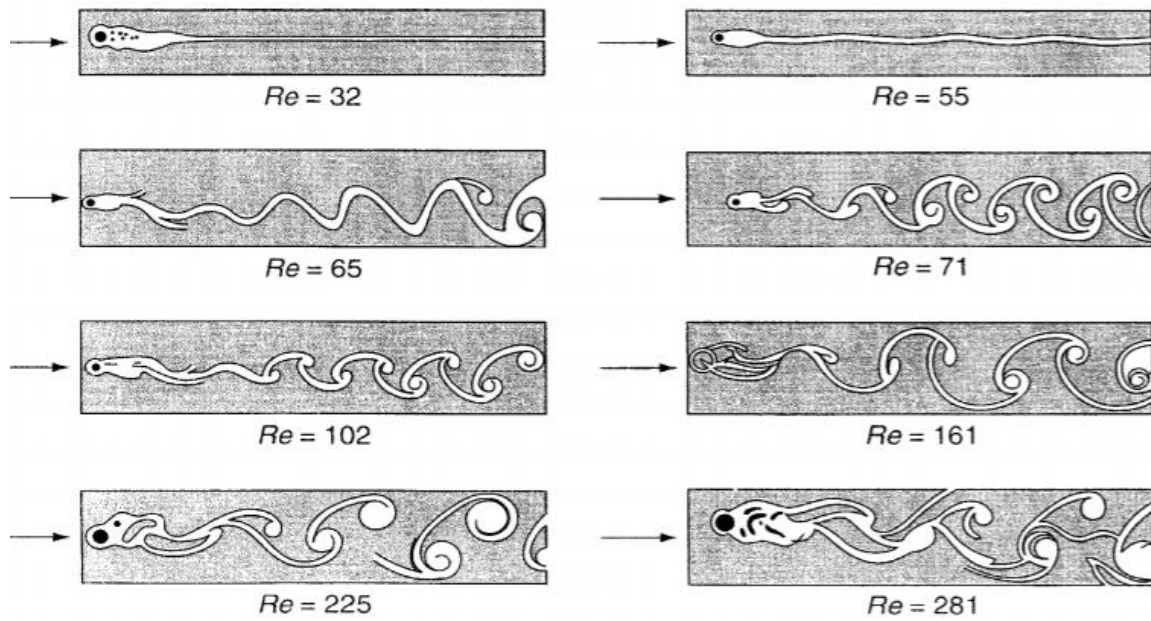
Figure 3.1: The effect of the Reynolds number on the flow past a cylinder (White, 1991)

The flow behind the tubes with a Reynolds number of 65 and above is seen to break away or "separate" from the rear surface, forming a broad, pulsating wake. It is important to note that the wake comprises pairs of vortices and sheds alternately from the upper and lower part of the rear surface. This type of vortices is known as Kármán vortex streets and defined as a stable configuration for vortex pairs in the paper by Kármán (Kármán, 1911). It is seen that as the Reynolds number increases, the wake becomes more complex and turbulent (White, 1991).

The Fanning friction factor is a dimensionless number used as a local parameter in continuum mechanics calculations and is defined as the ration between the local shear stress and local flow kinetic energy density (Simscale.com, 2018). To determine the friction factor f, equation 3.8 is used as follows:

$$f = \frac{(\Delta p_f).(2\,\rho_{air})}{G^2.\frac{A_i}{A_c}} \tag{3.8}$$

Where Δp_f denotes the pressure drop across the HX and:

$$\frac{A_i}{A_c} = \frac{4 \times L}{D_h} \tag{3.9}$$

Because of the significant need to improve the performance of HXs, many variations of compact HXs were researched and further developed. Regarding HX parameters, a variety of studies did a great amount of experimental and numerical work to enhance heat transfer and reducing pressure drop to achieve the maximum HX efficiency. When considering an air-cooled HX's thermal efficiency,

the reduction of thermal resistance on the airside is of utmost importance as mentioned in Chapter 1 (Yuan *et al.*, 2000).

A method has been developed in the 1940's to quantify this heat transfer capability with pressure drop in mind, and is described as the goodness factor. The ratio of the Colburn factor and the Fanning friction factor is plotted versus the Reynolds number . This factor is therefore an excellent alternative to quantifying a HX efficiency by describing a HX with a certain surface having a higher $j/f\ factor$ as good because it will require a lower free-flow area and hence a lower frontal area (Fugmann, Laurenz and Schnabel, 2019). Equation 3.10 calculates this factor.

$$Goodness\ factor = j/f$$

(3.10)

3.2. Model development

In this section, the rationale and reasoning behind the simulation model development is provided. This entails the construction of a TTI FCHX model, and two RS models. The TTI FCHX model and RS model thereof are both constructed with plain fins based on the HX surface specifications from *Compact heat exchangers, 3rd edition (1998)*. More attention will be placed on the wavy fin RS models in Chapter 5 but it can be noted that the model development thereof was identical to the plain fin RS model.

The model development was done by using a plain fin RS model as a visual aid and represents the construction of all three model types implemented in this study. Construction of the TTI- and RS models were fundamentally identical, but where differences were encountered a definitive explanation was given.

Focus is also put on how the repeatable, flow passage (for the RS model) was identified and, using an AutoCAD system, transformed into the models to be used for simulation purposes.

3.2.1. Model identification

For the FCHX configuration investigated, warm water flows inside the tubes and is cooled down by air flowing on the outside, unmixed across the staggered finned coil. The materials used for the construction of the HX include copper for the tubes and aluminium for the fins, but it should be noted that the water and copper tubes will not be created to limit computational expenses. More detail is provided later in this section on the approach that will be followed without the copper tubes- and water regions.

In order to follow the pre-determined, international standards for identifying the different physical fin- and tube parameters, the parameters are briefly discussed following figure 3.2.
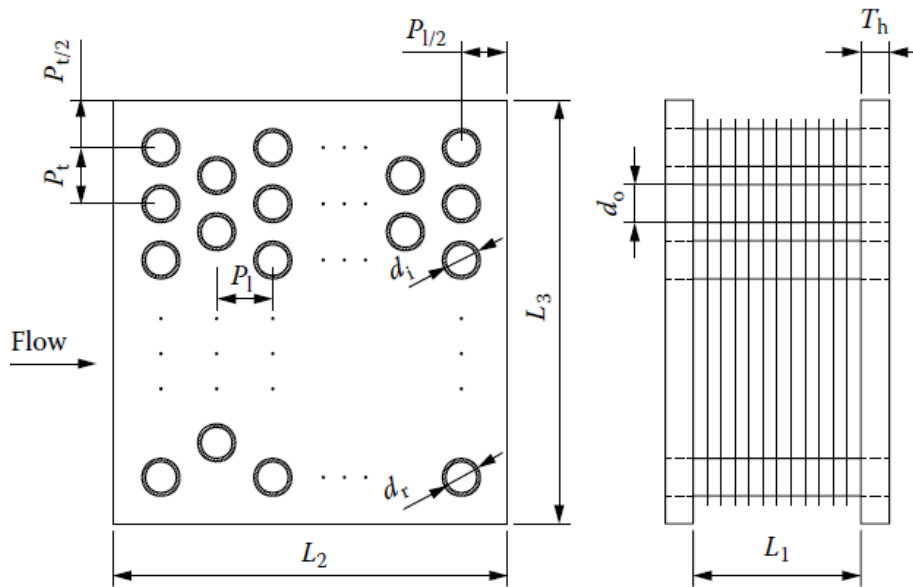
Figure 3.2: FCHX international physical dimensioning system for staggered tube configuration (Thulukkanam, 2013)

Where L_1, L_2, L_3 represent the HX length, -depth and -height respectively; P_t, P_l represent the transverse- and longitudinal tube pitch; T_H is the thickness of the header; d_i, d_o, d_r represent the inner-, outer- and effective fin diameter at the collar (Thulukkanam, 2013). A good understanding of these parameters and the role thereof in the FCHX's physical assembly is critical. The correct implementation of these parameters will govern the repeatability of the model.

Having a thorough understanding of the manufacturing process of an FCHX should assist in the correct development of the simulation models. Typically, as manufactured in the industry, the aluminium of the fins mechanically wraps the copper coil that contains the warm water (as illustrated in Figure 3.3). The copper coil is thus completely contained within the aluminium fins in such a manner that only aluminium has contact with the air. This helps prevent the copper from oxidising due to air with a relatively high humidity and becoming less effective after a long time. Heat transfer is the main decisive factor with cost considerations coming in at second. The combination of using aluminium for the fins and copper for the coil offers the most effective heat transfer at the most effective cost (Capital Coil & Air, 2018). Most fins are mechanically rolled into the specified profile (if needed) and have a lot of variations depending on the application.
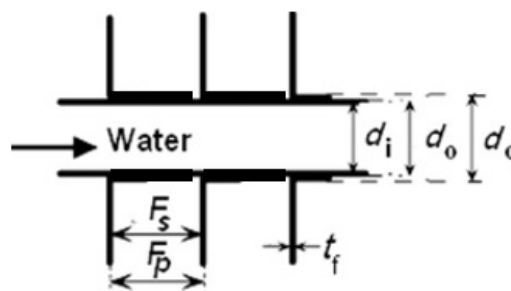
Figure 3.3: Fin to coil mechanical fitting illustration

Where d_i, d_o and d_c denote the coil inner- and outer diameter as well as the diameter where convection takes place respectively. The parameters F_s, F_p and t_f represent the fin spacing, fin pitch and fin thickness respectively. Full thickness fins and multiple segments (air flow passages) were constructed as a single model for the construction of the TTI FCHX model. Both the plain- and wavy models representing a segment of the FCHX (i.e. the RS models) focused on one of these air passages with half-thickness fins adjacent on both sides.

Less focus is put on how heat energy is transferred from the water to the fins as the experimental results from *Compact heat exchangers, 3rd edition (1998)* focus only on the airside of the HX. A tube wall temperature was therefore set as representation of the copper coil containing warm water in order to model an FCHX that is commonly found in the industry as performed by numerous studies in the past (Tahseen, Ishak and Rahman, 2015; Borrajo-Peláez *et al.,* 2010; Lu *et al.*, 2011; Erek *et al.*, 2005; Romero-Méndez *et al.,* 2000; Bhuiyan, Amin and Islam, 2013; Panse, 2005; Jang, Wu and Chang, 1996; Tutar and Akkoca, 2004; Khudheyer, *et al.,* 2011; Darvish Damavandi, Forouzanmehr and Safikhani, 2017, etc.). A constant wall heat flux is therefore achieved for both the TTI- and RS models and is viable assumption because of the high temperatures and flow rates implemented within the experimental procedure.

For the FCHX RS models, selecting the computational domain must be representative and repeatable segment of the TTI FCHX model. The domain section includes the three main air regions, namely the upstream-, main- and downstream air regions as illustrated in figure 3.4.
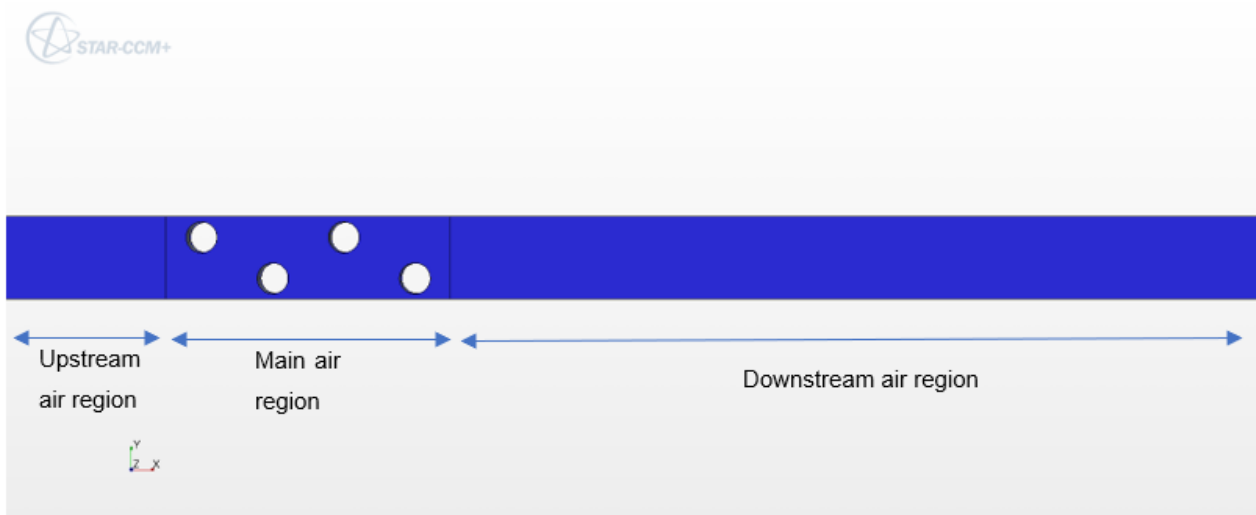
Figure 3.4: Side view of plain fin air flow passage and domain regions

The upstream air region is designed with the purpose to represent the air entering the main region in order to enable the leading fin edge effect within the air flow pattern. Only serving a single purpose, the upstream air region does not have to take up a considerable amount of computational resources and is therefore restricted in cell count. The main air region contains the aluminium, adjacent half-

26

fins and tube (staggered configuration) positions where turbulence is induced. The success of the whole simulation depends on the main air region's thermal-hydraulic performance and needs to be modelled with an acceptable accuracy. Following the main air region is the downstream air region where the turbulent air flow patterns are further developed. The downstream air region is designed to be five times the length of the upstream air region to capture all relevant flow patterns and air outlet temperature variations (Lu *et al.*,2010).

3.2.2. Computational domain construction

The design parameters, domain materials and measurements of the HX with a surface $8.0 - 3/8T$ from *Compact heat exchangers, 3rd edition (1998)* are illustrated in figure 3.5 and tabulated below using table 3.2.

Tube outside diameter, D_o = 10.2 mm
Fin pitch = 315 per meter
Flow passage hydraulic diameter, D_h = 3.63 mm
Fin thickness = 0.330 mm
Free-flow area/frontal area, σ = 0.534
Heat transfer area/total volume, α = 587 m^2/m^3
Fin area/total area = 0.913
Note: Minimum free-flow area is in spaces transverse to flow.
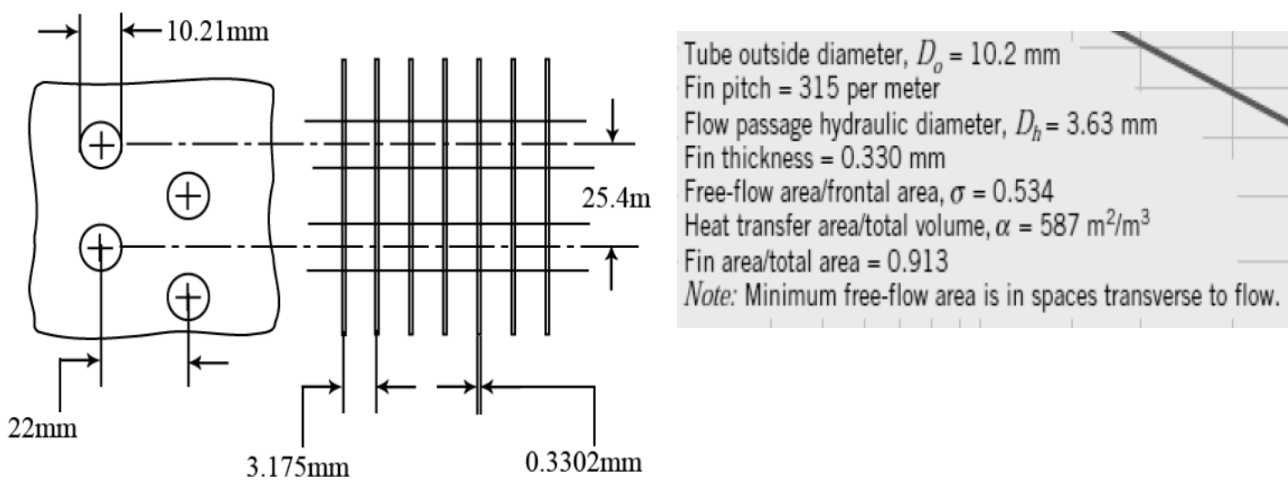
Figure 3.5: Surface 8.0 - 3/8T physical dimensions (Fchart.com, 2018)

Figure 3.5 illustrates the basic geometric parameters of the FCHX surface. It can be seen that only two rows of tubes are used for visualisation purposes whereby the transverse- and longitudinal tube pitches are displayed as 25.4mm and 22mm, respectively. Other important information is also given to describe the fin pitch and thickness in more detail, as well as valuable data of different HX related areas. These geometric parameters as a collective are described in the book of *Compact heat exchangers, 3rd edition (1998)* as a HX surface.

It is important to note that the construction of the wavy- and plain fin models was based on an identical set of geometric parameters and only differed by fin surfaces (surface 8.0 – 3/8T). The plain fin model construction was used as the base model and consisted of the parameters as shown in Figure 3.5. The wavy fin model consisted, therefore, of a wavy fin surface with a popular waffle height as found in industry and is further discussed in Chapter 5 (Panse, 2005).

The plain fin RS computational model is illustrated in Figure 3.6. All computational domain models in this study (RS and TTI) were constructed using Solidworks AutoCAD software.
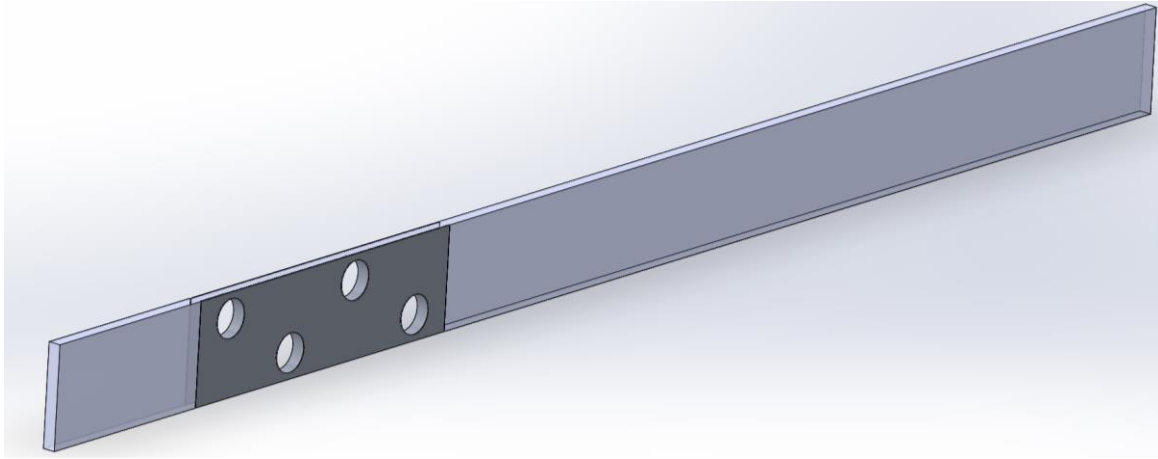
Figure 3.6: Plain fin RS FCHX model (Surface 8.0 - 3/8T)

It was deemed sufficient to create a TTI FCHX model with a front facing area of $100mm \times 100mm$ which ensured the implementation of multiple air flow passages. This model therefore comprises of 120 plain fin segment models and is illustrated in Figure 3.7.
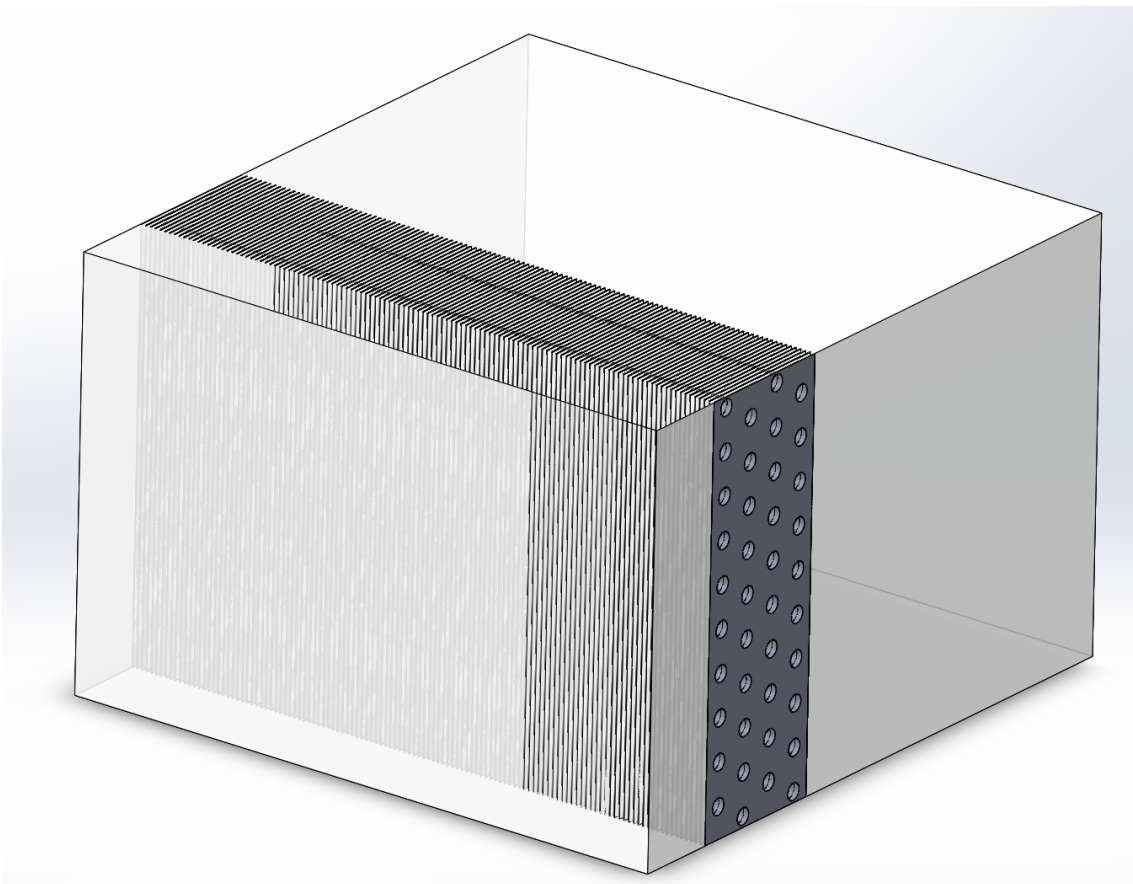
Figure 3.7: TTI plain fin FCHX model computational domain (Surface 8.0 - 3/8T)

It can be seen that both computational domains consist of a fins/tubes part and an air part. The air part was set to transparent in both figures 3.6 and 3.7 for visualisation purposes. These models are thus set for the import process into STAR-CCM+ as Parasolid file types.

28

Table 3.2: Simulation domain dimensions and material models

Dimension	Value (mm)	Material model used
TTI domain frontal area	100x100	N/A
Fin thickness (t_f)	0.33	Aluminium
Upstream air length	50	Air
Downstream air length	250	Air
HX depth (L_2)	88	Air
Air channel width	2.84	Air
Tube transverse pitch (P_t)	25.4	N/A
Tube longitudinal pitch (P_l)	22	N/A
Tube outside diameter (D_o)	10.21	Aluminium

3.2.3. Simulation model creation

For this chapter, the plain fin RS model is used for visual purposes to illustrate the AutoCAD modelling process (containing all regions) and how/why certain simulation models and meshing procedures are used. All simulation physics- (STAR-CCM+ term for material and fluid/gas flow models) and meshing models applied to the different regions regarding material types, gas flow and energy that will be discussed in this chapter are chosen within STAR-CCM+ and will apply to simulations done in both chapters 4 and 5.

First, the computational domains created using Solidworks was imported into STAR-CCM+ by implementation the Import Surface Mesh function. Using the built-in AutoCAD capabilities of Star-CCM+, the geometry was split into various surfaces by using the "Split by part curves" and "Split by patch" operation. Each surface was named to show the direction of flow (inlets, outlets, symmetry- and periodic planes, mass flows, etc.) to avoid confusion in the later stages of the simulation procedure. Each part was then exported as "Create a region per part" as specified by the software. This created a region from each part which formed the basic building blocks of each solid/gas region.

Figure 3.8 to 3.10 illustrate the TTI FCHX-, plain fin and wavy fin RS models, respectively, after defining all surfaces and regions.
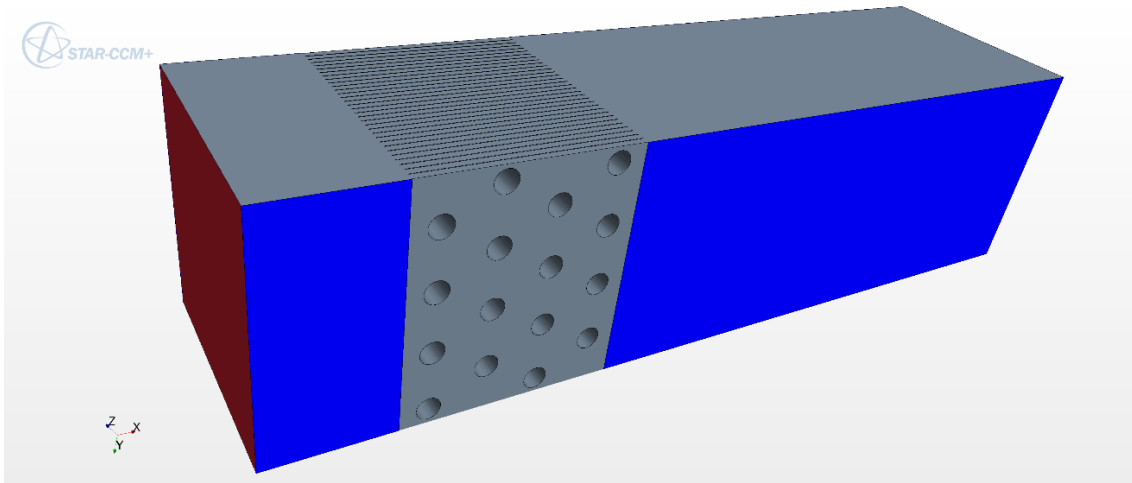
Figure 3.8: TTI FCHX simulation model
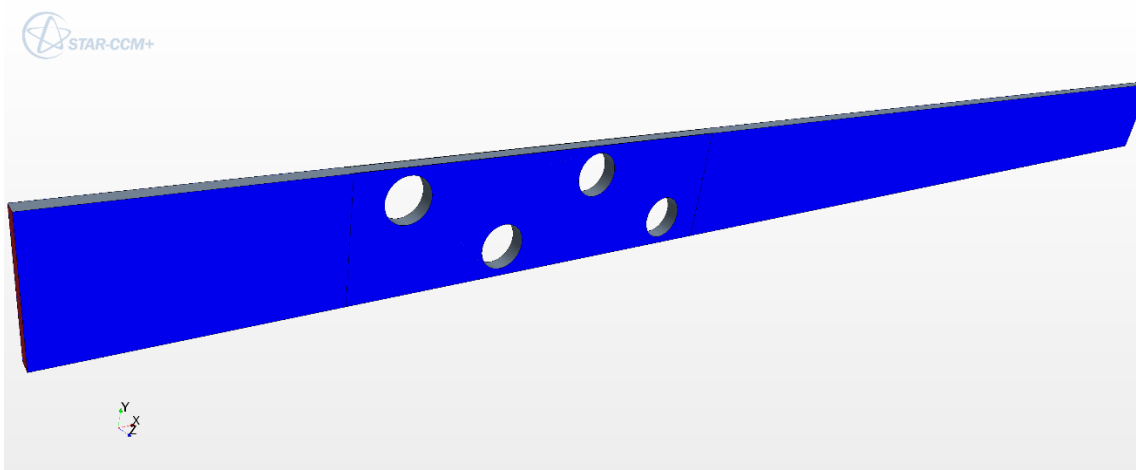
Figure 3.9: Plain fin RS model
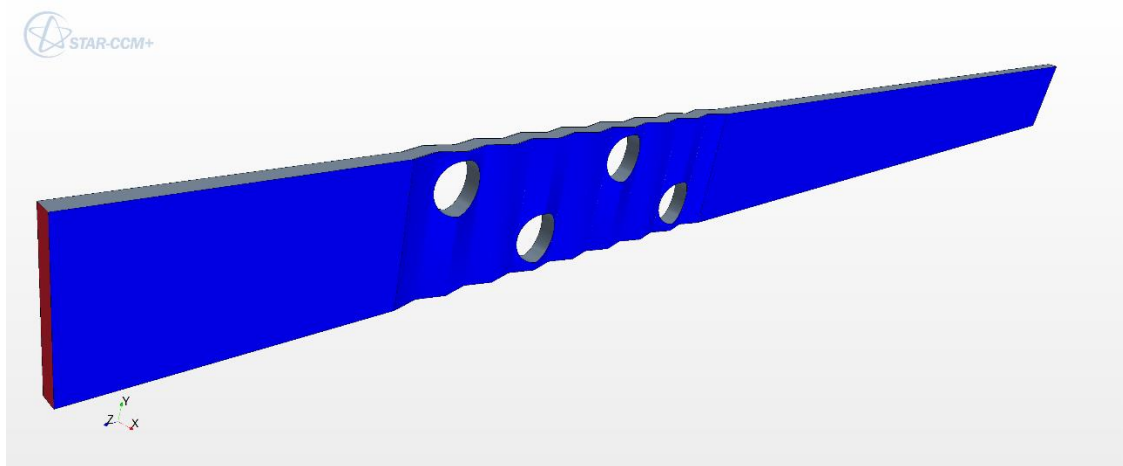
Figure 3.10: Wavy fin RS model

Colours on the model surfaces are used to serve as identification of various surface conditions. The blue surfaces illustrated in figure 3.8 to figure 3.10 serves as a sign of symmetry planes and the red surfaces on the upstream air region serve as a sign of velocity inlets. The orange surfaces (not shown in the figures, hidden due to illustration angle) show pressure outlets within the downstream air region and grey surfaces, normal wall type surfaces.

To connect all the different regions and ensure a continuous air flow, internal interfaces were created on surfaces connecting the three main regions. These interfaces were set in place for the program code to recognise the flow passage and not automatically set up walls that would cause a domain with broken flow and inaccurate results. The Surface Repair tool also becomes a fundamental step in the process as this is used to imprint surfaces and improve the cell "communication" between cells once the volume mesh has been generated. This will be further discussed in section 3.3.1.

A critical part to note is that the contacts between materials should be defined as In-place interfaces on STAR-CCM+. This is a crucial part of the simulation because these interfaces act as the contact- and convective thermal resistances in the model and connects the various regions as previously mentioned. If the interfaces aren't defined, no heat transfer or continuous air flow will take place causing the simulation to generate inaccurate or even no results. If the geometry was correctly designed, the software creates the interfaces automatically. If the interfaces aren't created for some unknown reason, they need to be defined by the user using the Surface Repair tool or manually defining interfaces by using the simulation tree menu to find a suitable solution.

Different types of interfaces are encountered with STAR-CCM+ and each interface type serves a specific purpose. If the interfaces are correctly applied this will guide the software to create an accurate simulation and imitate the natural flow of heat and air. "Internal interfaces" are created between different fluid regions (gas or liquid) to show a connected flow volume. "In contact" interfaces indicate contact between a solid and a fluid- or solid and solid regions. A vital interface to implement in the plain- and wavy fin RS models are the "periodic interface" that suggests how the outer surfaces of the domain connect to the rest of the HX. Without this interface type, a RS model approach to the FCHX would not be possible and render the study invalid. This interface thus improves predictions of the flow of air and heat between two opposite faces to be coupled and mimic the flow of an entire FCHX. Table 3.3 tabulates the interfaces found in the domain:

Table 3.3: List of interface implementation and interface type in the computational domain

Type of interface	Implementation areas
Internal interfaces	Upstream air and Main air, Main air and Downstream air.
In contact interfaces	Fin edges with Upstream and Downstream air, Fins and Main air
Periodic interfaces	All Air regions' top and bottom surfaces, Fins' top and bottom surfaces.

The same naming criteria will apply to the physics (turbulence-, energy-, transient or steady- and material modelling) and meshing (polyhedral, prism layering, etc.) tools implemented in the simulation software to keep the various model descriptions in-line with the STAR-CCM+ environment. To prevent any confusion, when referring to the mesh- and physics "continua" the reader should interpret the term as used within the Star-CCM+ environment.

After each simulation model was developed with all regions and surfaces properly defined, the inner physical working of the model had to be defined. This included splitting the domain into smaller volumes, named mesh cells. The next section will address the meshing procedures followed accompanied by the rationale thereof.

3.3. Mesh continua

A mesh is discretizing the computational domain into recognisable cells where physics solvers are used to provide a numerical solution for each individual mesh cell. Different meshing techniques and tools are provided by STAR-CCM+ that one can use to generate a mesh of substantial quality depending on the application. It is common practice to first study a wide variety of literature to ensure that the correct meshing tool is used and generate acceptable results.

It should be noted that before a final mesh is used for further simulation, a mesh independence test (MIT) must be done. This process is used to guarantee an economical approach in terms of computational resources and at the same time generate an acceptable set of results. Using a simulation with many cells can prolong the overall simulation process and therefore increase the runtime to a large extent. The recommended amount of Random-Access Memory (RAM) required to volume mesh a domain, using polyhedral cells as the main meshing tool, is 1 GB per million cells. Having less RAM would thus result in a slow convergence speed and ultimately a very tedious simulation process.

It is widely agreed upon that the residual RMS error values are to at least and had reached a steady state. This will indicate, together with the monitored quantities such as pressure drops, heat transfer coefficients, a converged result. Finally, it needs to be ensured that the overall imbalance in the domain is less than 1% for all variables (Kuron, 2019).

3.3.1. Choosing appropriate volume meshing tool

Selecting the type of volume mesh is one of the most critical choices to be made by the STAR-CCM+ user. Selecting the "wrong" meshing tool will affect the accuracy of the results and ultimately create a questionable simulation. The choice of the core volume mesh depends on several factors, namely: the desired solution accuracy and convergence rate, the amount of memory available on your computer, the quality of the starting surface mesh, the turnaround time available for building the mesh, whether the geometry is predominantly thin, etc.

Some of these factors, however, are not mutually exclusive. For example, the tetrahedral mesher is the fastest volume mesh generator (in terms of the number of cells that are generated per minute) and the one that uses the least amount of memory. However, in terms of solution quality, approximately five to eight times the number of cells is required to produce the same accuracy as the equivalent polyhedral or trimmed cell mesh (Volume Meshers Overview, 2016). Therefore, it is essential that the accuracy is evaluated against the speed of the convergence before selecting the appropriate volume meshing tool.

The meshing structure that is used in this study makes use of only one mesh continua containing various meshing tools. The mesh is then applied to all regions and the mesher/s is/are then set for each individual region, depending on the region's material and main monitoring areas. In doing this, the mesh cells' conformality is drastically increased and in return improves the "communication" between neighbouring cells. The meshing tools used in the simulation are Polyhedral mesher, Prism Layer mesher, and Surface remesher. The following table indicates the main domain regions, and the applied meshing tools.

Table 3.4: Application of various meshing tools with associated regions

Meshing tool name	Applied region/s
Polyhedral mesher	Air, Fins.
Prism Layer mesher	Air.
Surface remesher	All regions.

3.3.2. Polyhedral mesher

The Polyhedral mesher is generally used for a wide variety of simulations as it provides a balanced solution for complex mesh generation problems (Peric and Ferguson, 2018; Jabbour *et al.*, 2019). This mesh is ideal for the application of the current study as each individual polyhedral cell neighbours with more cells compared to hexahedral and tetrahedral cells which improves the calculation of gradients and allows to interchange the mass over numerous faces, reducing numerical diffusion effects caused by flows not perpendicular to any of the cell face. It is helpful in situations where no prevailing flow direction can be identified and leads to a higher accuracy achieved with a lower cell count. Polyhedral cells are not oversensitive to stretching and therefore assure an overall improved numerically stable model (Sosnowski *et al.*, 2018).

These types of meshes are relatively easy and efficient to build by the simulation software, requiring no more surface preparation than the equivalent tetrahedral mesh. The polyhedral mesher also uses about five times fewer cells than the tetrahedral mesh with the same starting surface mesh making it the ideal base mesh for the simulation domain. Multi-region meshes with a conformal mesh interface are allowed; making it thus possible to apply different meshes in different regions (Volume Meshers Overview, 2016).

The polyhedral mesher makes use of arbitrary polyhedral cell shapes to form the mesh core. Using a special dualization scheme in STAR-CCM+, the polyhedral mesh is automatically created from an underlying tetrahedral mesh after a surface mesh operation has been completed (seen in Figure 3.11). Lewis found in as early as 1933 that typical polyhedral cell has an average of 14 cell faces (Lewis, 1933).
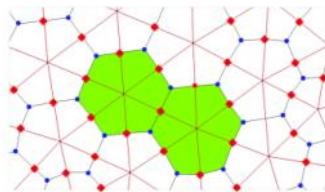
Figure 3.11: Conversion of tetrahedral cells to polyhedral cells (Sosnowski *et al.*, 2018)

Referring to table 3.4, the polyhedral meshing tool was used as the base mesh for all the different regions in the domain. The air region, where capturing the heat transfer and pressure drop are of the highest priority, a prism layer mesh is applied. Section 3.3.3 is used to clarify the typical usage of the prism layer meshing tool. No further refinement of the mesh is required around the tubes due to the mesh cells already being small enough to capture all relevant heat transfer and pressure drop information (and was confirmed using the Mesh Independency Test (MIT) in Chapter 4). The following illustrations display the implemented polyhedral core mesh using the Threshold function of STAR-CCM+
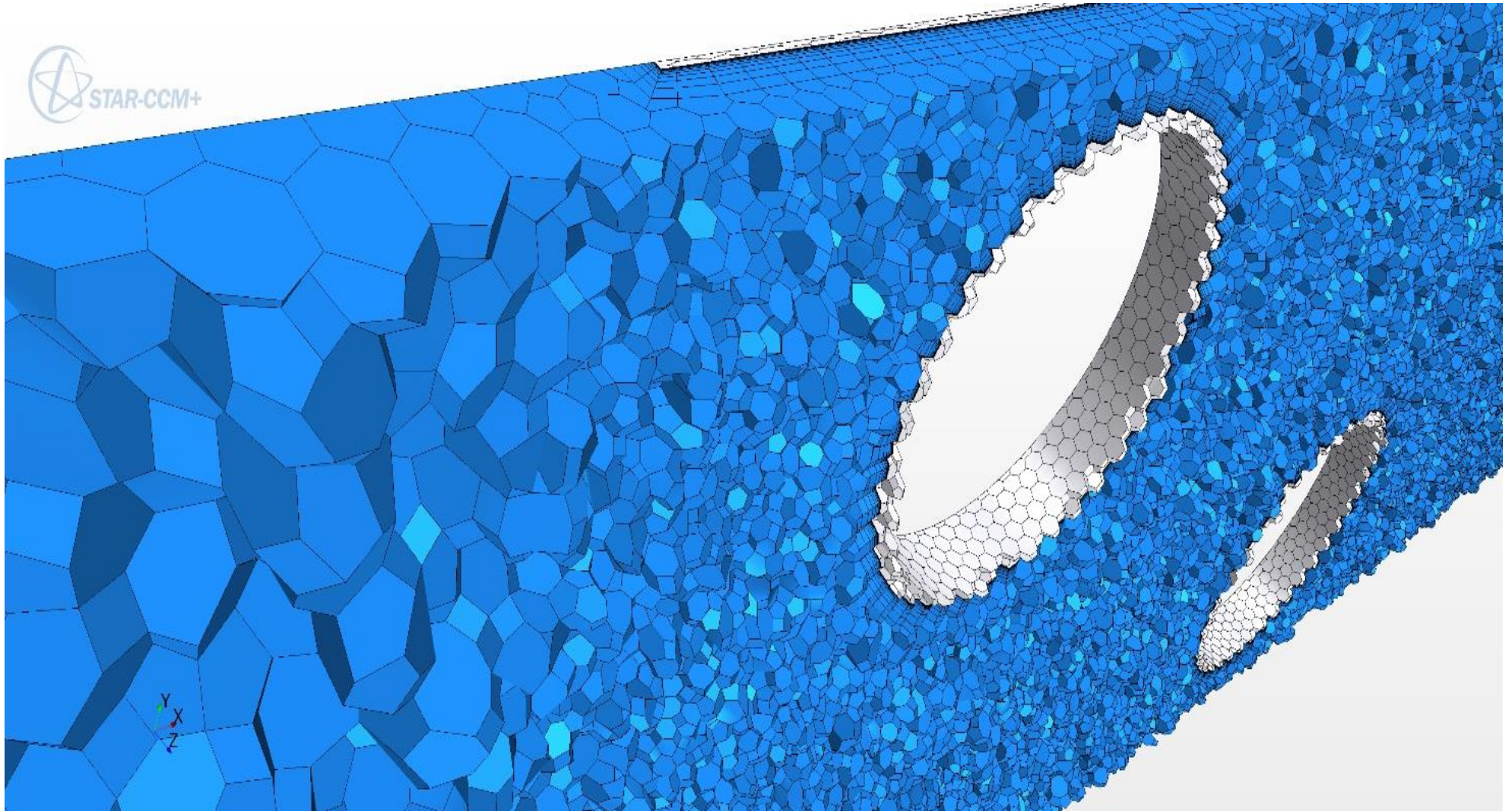
Figure 3.12: Internal side view of overall mesh
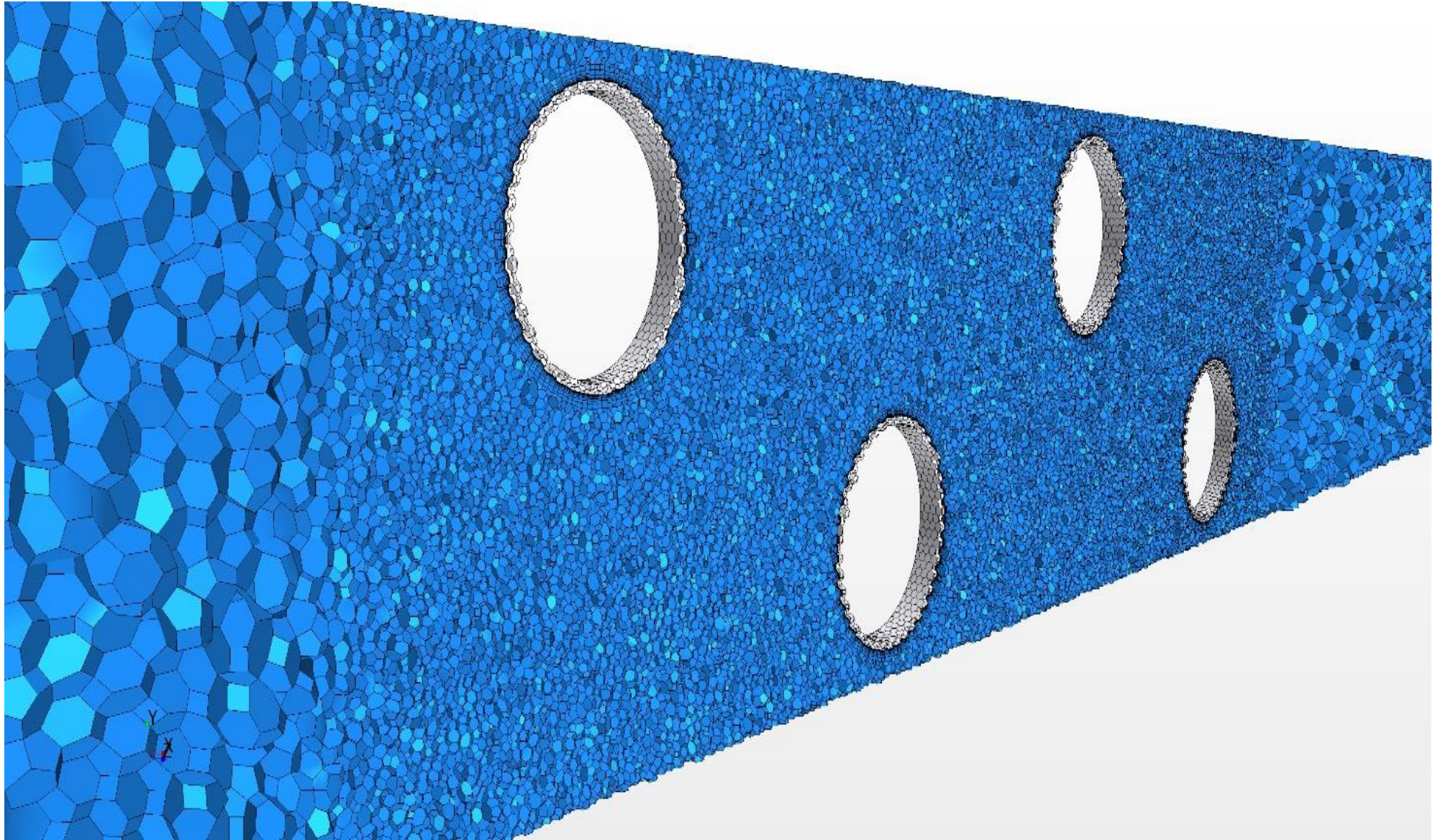
Figure 3.13: Mesh growth and refinement

Referring to Figure 3.12 and 3.13, a visual representation is made to distinguish between regions using different colours. The air region is denoted by using light blue and the fins by using white. The ideal mesh practice of cell conformality is illustrated to ensure an overall domain with no broken surfaces or any volume related abnormalities.

3.3.3. Prism layer mesher and boundary layer approach

A prism layer mesh is composed of orthogonal prismatic cells that usually reside next to wall boundaries in the volume mesh (Southampton.ac.uk, 2018). The purpose of using a prism layer mesh is in order to accurately simulate the turbulence and heat transfer generated in the boundary layer. Using the boundary-layer model, the number of prism layers, -thickness and -distribution is primarily determined. Typically, for wall function-based models, one to three layers are deemed as normal, whereas fifteen to twenty-five layers are normal for low Reynolds number- and two-layer schemes (Southampton.ac.uk, 2018).

Simulating the boundary layer has shown to be difficult in a range of different studies where the heat transfer and pressure drop were of interest (Garimella *et al.*, 2018). "A boundary layer is a thin layer of viscous fluid close to the solid surface of a wall in contact with a moving stream in which (within its thickness δ) the flow velocity varies from zero at the wall (where the flow "sticks" to the wall because of its viscosity) up to at the boundary which approximately (within 1% error) corresponds to the free stream velocity" (Schlichting, 1955). Figure 3.14 is used to illustrate the boundary layer growth as found on a flat, plain plate.
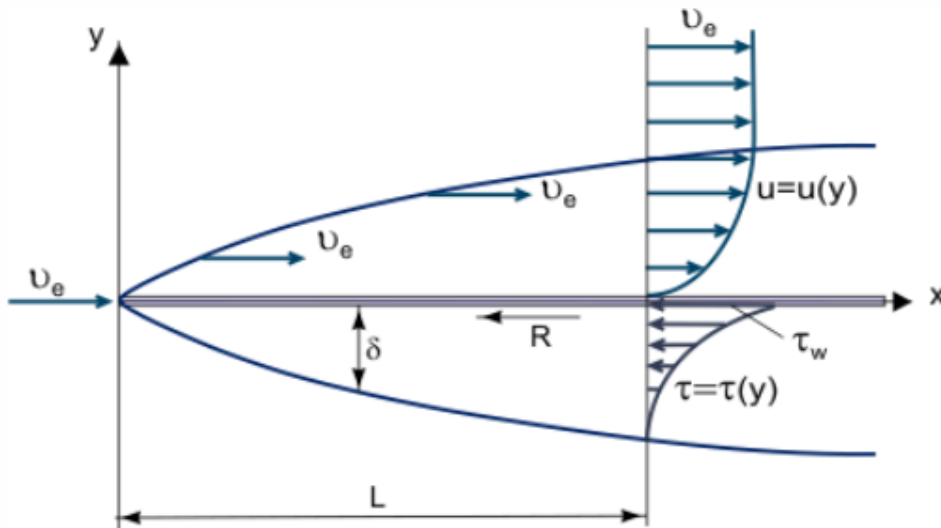
Figure 3.14: Boundary layer growth on a flat plate (Schlichting, 1955)

Where τ denotes the viscous shearing force, u_e the air stream velocity, L the characteristic linear dimension of the body over which the flow occurs and R the direction of friction caused by the plate

surface. L. Prandtl (1904) defined the boundary layer as a layer of fluid developing in flows with very high Reynolds numbers, that has a relatively low viscosity compared to the associated inertia forces (Prandtl, 1904). This observation is made when a plate profiled body is exposed to a high velocity air stream or when the body is large and the air stream velocity moderate.

The boundary layer is a very thin volume and is, despite its relative thinness, very important for starting processes of dynamic interaction between the fluid flow and the body surface. The boundary determines the energy loss for fluid flow in channels, which is referred to as a hydrodynamic boundary layer. This is due to including the thermal boundary layer, which determines the thermodynamic interaction of heat transfer (Schlichting, 1955). When the purpose of a simulation is to achieve an acceptable amount of accuracy, one should note the importance of placing enough cells (or sometimes referred to as grid points) close to the wall. This is done to capture the velocity profile, heat transfer, and pressure drop in regions where the flow will experience rapid change with satisfactory accuracy. Hence, it is of prime interest to model these interactions around the wall; implementing prism layers becomes vital for this study.

It can be seen from Figure 3.13 that the amount of prism layers on the air side and the waterside has been set to 3. Figure 3.15 illustrates the contact area between the fin and air regions to display the prism layer construction to predict heat transfer and pressure drop. The leading edges of the fins are constructed as illustrated as the manufacturing process causes too many inconsistencies in edge shape.
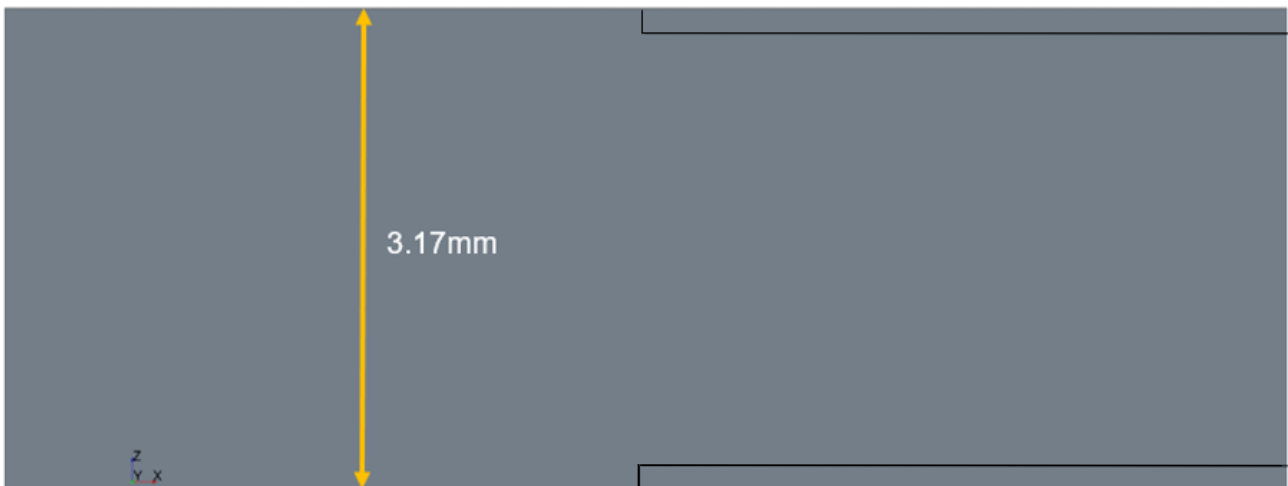
Figure 3.15: Top view of air entry between fins to illustrate the usage of prism layers on leading edges

A need was identified to quantify the relationship between fluid velocity and wall distance in the early 1900's. This problem was addressed by Theodore von Kármán when in 1930 he developed the "Law of the Wall". This law established the relationship between the average velocity of a turbulent flow at a certain point as being proportional to the logarithm of the distance from that point to the boundary of the fluid region or "Wall" (von Kármán, 1937). This formulation is only applicable to parts of the

fluid flow that are close to the wall (within 20% of the height of the flow), but is seen as a good approximation for the entire velocity profile of natural streams (Martynenko and Polijakov, n.d.). Figure 3.16 illustrates the "Law of the Wall".
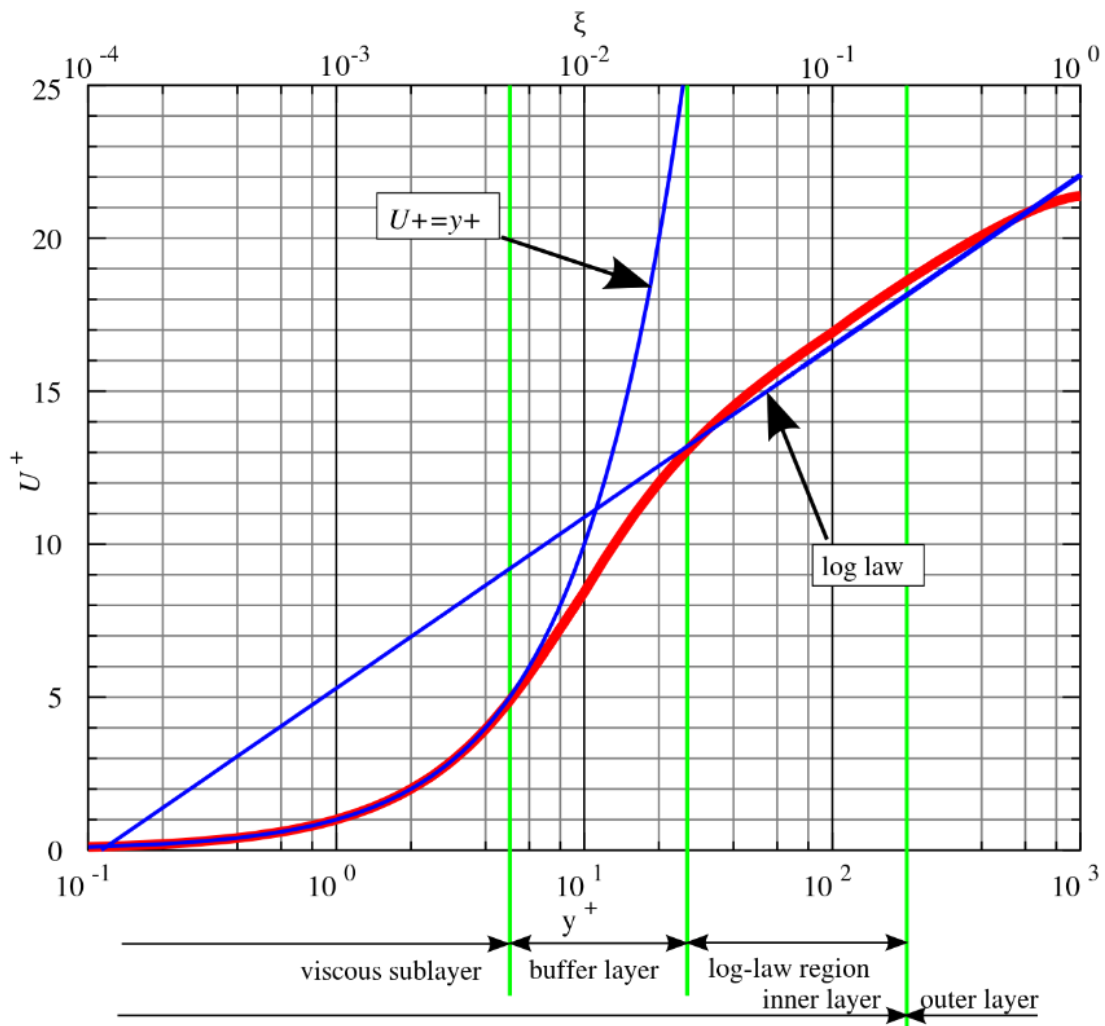
Figure 3.16: Law of the wall (von Kármán, 1937)

The priority of predicting heat transfer and pressure drop is selecting the turbulence model that has good wall treatment and is not computationally expensive (which has been chosen in Chapter 2 as the k-ω turbulence model). The turbulence model then determines the level of detail required in the boundary layer model as each turbulence model presents a different wall modelling approach which needs a different level of discretization close to the wall (Kapoor, 2018).

The wall treatment reference for various turbulence models as distributed by STAR-CCM+ are tabulated and illustrated in Table 3.5. This table was used to find the appropriate y+ value best suited for the k-ω turbulence model. It can be seen that all y+ values are applicable to the k-ω turbulence model.

Table 3.5: Wall treatment reference (Wall treatment reference, 2018)

			High y+	Low y+	All y+
Detached Eddy Simulation	EB K-Epsilon Detached Eddy			✓	✓
	SST (Menter) K-Omega Detached Eddy		✓	✓	✓
	Spalart-Allmaras Detached Eddy			✓	✓
Large Eddy Simulation	Dynamic Smagorinsky Subgrid Scale			✓	✓
	Smagorinsky Subgrid Scale			✓	✓
	WALE Subgrid Scale			✓	✓
Reynolds-Averaged Navier-Stokes	K-Epsilon Turbulence	AKN K-Epsilon Low-Re		✓	✓
		EB K-Epsilon		✓	✓
		Lag EB K-Epsilon		✓	✓
		Realizable K-Epsilon	✓		
		Realizable K-Epsilon Two-Layer			✓
		Standard K-Epsilon	✓		
		Standard K-Epsilon Low-Re		✓	✓
		Standard K-Epsilon Two-Layer			✓
		V2F K-Epsilon		✓	✓
	K-Omega Turbulence	SST (Menter) K-Omega	✓	✓	✓
		Standard (Wilcox) K-Omega	✓	✓	✓
	Reynolds Stress Turbulence	Elliptic Blending			✓
		Linear Pressure Strain	✓		
		Linear Pressure Strain Two-Layer			✓
		Quadratic Pressure Strain	✓		
	Spalart-Allmaras Turbulence	High-Reynolds Number Spalart-Allmaras	✓		
		Standard Spalart-Allmaras		✓	✓

A low wall y+ treatment ($y^+ < 1$) was chosen for this study. Because of the number of grid points located close to the wall, this wall treatment type does not require too many cells and is thus less expensive considering a limited amount of computational resources. Hence, the choice of turbulence model required for all y+ values will damp the turbulence in the near-wall region in this study; and is further discussed in section 3.4.

The distance to the first grid point is calculated using the following set of equations from 3.11 to 3.15 ("Y+ Calculator - Compute Wall Spacing for CFD", 2019).

$$Re = \frac{\rho_\infty V_\infty L}{\mu_\infty} \tag{3.11}$$

$$C_f = [2 \log_{10}(Re) - 0.65]^{-2.3} \ for \ Re < 10^9 \tag{3.12}$$

$$\tau_w = C_f . \frac{1}{2} \rho_\infty V_\infty^2 \tag{3.13}$$

$$u_+ = \sqrt{\frac{\tau_w}{\rho_\infty}} \tag{3.14}$$

$$\Delta y = \frac{y^+ \mu_\infty}{u_+ V_\infty} \tag{3.15}$$

Where ρ_∞ denotes the freestream density, μ_∞ the freestream dynamic viscosity, u_+ the friction velocity, Δy the first node distance, y^+ the dimensionless node distance, τ_w the wall shear stress and C_f the skin friction coefficient.

3.3.4. Mesh values chosen

Tables 3.6 illustrates the mesh sizes and layers implemented for the full FCHX and segment (plain and wavy) models, respectively. The values have been chosen with the before mentioned information kept in mind and after completion of a MIT.

Table 3.6: Full FCHX mesh input values

	TTI FCHX model	Plain- and wavy RS models
Base size	10 mm	10 mm
Number of Prism layers	15	15
Prism layer stretching	1.5	1.5
Prism layer thickness	5.0% *(percent of base)*	8.0% *(percent of base)*
Surface size		
Relative Minimum Size	5.0% *(percent of base)*	5.0% *(percent of base)*
Relative Target Size	30.0% *(percent of base)*	25.0% *(percent of base)*

Implementation of a larger base size for the full FCHX model is done to limit the number of cells in areas of less interest, i.e. the inlet and outlet air regions and substantially decrease the computational expense. Manipulation of the other meshing models (Prism layer thickness and Surface size) by making use of a smaller percentage base sizes as compared to the segment models gave the opportunity to create a finer mesh where capturing the heat transfer and pressure drop is of utmost importance.

In the next section the physical properties of the materials are defined as well as the flow models used for the air.

3.4. Modelling Physics continua

Using the regions tab, all relevant properties of the selected region can be stated. This includes the region physics conditions and -values, mesh conditions, feature curves and boundaries, which indicates the region outline. The physics must be created using the continua tab for each gas/solid to state the nature of the flow and/or heat transfer and is then linked with the applicable regions.

Physics continua must be created for every material type and fluid or gas that forms part of the model. The following materials and fluids in Table 3.7 are created using this procedure:

Table 3.7: Materials and applied areas

Material	Area used
Aluminium	Solid type material used for the fins.
Air	Gas type material designed to flow adjacent to the fins and perpendicular to the coil. Forms part of the upstream-, downstream- and main region.

The material model manages the material substance or substances, being simulated in the continuum. The simulated material manages the various thermodynamic and transport properties relevant to that material and to the physical processes being modelled in the continuum.

There are three general types of material models available in STAR-CCM+: single-component, multi-component, and multiphase mixture. Each of these material models manages one specific type of material: a pure substance, a multi-component mixture, or a multiphase mixture. Selecting a material model early in the model selection process allows STAR-CCM+ to assist the user in making subsequent modelling choices appropriately.

3.4.1. Solids

Creating solids includes choosing the correct appropriate models. The solid regions are identified as stated in table 3.7. The following pure substance models were chosen: Solid, Three Dimensional, Steady, Segregated Solid Energy, Gradients and Polynomial Density.

When the models have been chosen, the various material properties can then be set to the desired values, such as density, specific heat, thermal conductivity or just choosing the constant value from the database. Aluminium (being the default material used as a solid) are created using this procedure using constant values for the before mentioned properties. This was done due to the little effect the temperature has on these solids and would not affect the results by any margin. For any solid other than aluminium, the database should be used in order to replace the default material as needed.

3.4.2. Gases

The same procedure was done with choosing the suitable models for the gaseous regions (as stated in table 3.7). For the air, the following pure substance models was chosen: Gas, Three Dimensional, Steady, Segregated Flow, Segregated Fluid temperature, Gradients, Polynomial Density, Laminar (for applicable flow) and Turbulent. Using the Reynolds number as reference, the simulations were done using Laminar flow models for flow with $Re < 1400$ and Turbulent models for $Re > 1400$ (Chin Ngo, 2018). The material properties of the air, however, varied by a notable amount which required a change in the handling method from a constant value to the use of the Polynomial in T (varying values with temperature) method. Table 3.8 illustrates the polynomials used for air temperatures ranging between $0°C < T < 100°C$.

Table 3.8: Air polynomials of Temperature

Material property	Polynomial in T function
Dynamic Viscosity	$y = 2.13333E\text{-}15T^4 - 5.02993E\text{-}13T^3 + 7.44533E\text{-}13T^2 + 4.85765E\text{-}8T + 1.71535E\text{-}5$
Polynomial Density	$y = 8E\text{-}11\ T^4 - 5.03289E\text{-}8T^3 + 1.69367E\text{-}5\ T^2 - 4.73983E\text{-}3T + 1.29344$
Specific Heat	$y = -1.00372E\text{-}8T^4 + 3.34459E\text{-}6T^3 + 3.5744E\text{-}5T^2 + 4.03675E\text{-}2T + 1.00372E3$
Thermal Conductivity	$y = 5.33333E\text{-}13T^4 - 1.19822E\text{-}10T^3 - 2.69605E\text{-}8T^2 + 7.92934E\text{-}5T + 2.41214E\text{-}2$

With y being the material property value and T denoting the temperature in Table 3.8. The turbulence models chosen are: SST (Shear Stress Transport) (Menter) K-ω Turbulence, All y+ Wall Treatment, and Reynolds-Averaged Navier-Stokes. Table 3.9 below tabulates the motivation for the usage of the specific energy models as well as the chosen turbulence model.

Table 3.9: Energy and turbulence model motivation

Model name	Motivation for usage
Segregated flow	Most appropriate solver for the type of air flow due to less memory usage.
Segregated fluid temperature **Segregated solid energy**	Best option as opposed to coupled model for an accelerated convergence while maintaining accuracy and using less computational memory.
Reynolds-Averaged Navier-Stokes **SST (Menter) K-ω Turbulence**	Most effective model to be used for near wall predictions. Performs significantly better under adverse pressure gradient conditions compared to K-$\mathcal{E}$. Superior performance for wall-bounded boundary layer, free shear and low Reynolds number flows.

3.5. Conclusion

In this chapter, the development of the computational model and rationale thereof was discussed, alongside relevant background theory associated with certain simulation related models to ensure a coherent understanding. Important aspects such as the heat transfer and pressure drop related dimensionless numbers, model development, meshing strategy and simulation physics models (solids and gases, turbulence modelling, wall y+ values, etc.) were discussed as well as the implementation thereof in Chapters 4 and 5.

In the next chapter, model validation and result comparison are done for the plain fin TTI FCHX- and RS models in terms of model prediction accuracy.

Chapter 4 : TTI and RS models' validation, results and discussion.

4.1. Introduction

In this chapter, the simulation results of the plain finned, TTI and RS FCHX models will be validated and compared, using *Compact heat exchangers, 3rd ed. (1998) by W.M. Kays and A.L. London* as a reference. The experimental setup and procedure used by Kays and London was briefly discussed in section 2.4 in Chapter 2.

In order to evaluate the validity of both model types, model prediction accuracy of the heat transfer and pressure drop is determined and compared in terms of the Colburn j-factor and Fanning friction factor. This is the same approach as used by *Compact heat exchangers, 3rd ed. (1998)* and will therefore ensure an easier understanding. As the data retrieved from the simulations are in terms of the heat transfer coefficient (h) and pressure drop (ΔP), a methodology will be developed and discussed to compare results between simulations and experimental data and is discussed in section 4.3.

The results of this chapter will therefore serve a validation purpose; and determine the model type approach to be followed for Chapter 5 (TTI or RS model). Convergence time and model accuracy (on an acceptable level) with reference to *Compact heat exchangers, 3rd ed. (1998) by W.M. Kays and A.L. London* will be used as the main comparison criteria.

4.2. FCHX information

An important aspect to be able to perform the validation of the study is to use reliable information supplied by a renowned source as stated in Chapter 1. The following sub-sections will provide further information on how the information from *Compact heat exchangers, 3rd ed. (1998)* will be applied to the simulations to follow.

4.2.1. Experimental input data

As stated in section 2.15, the experiments were performed using inlet air at $30°C$ and slightly superheated steam at $110°C$. The air flow was tested for a range between $100 \leq Re \leq 8000$. The steam mass flow was selected to be at such a high value that a constant tube wall temperature could be achieved.

4.2.2. Experimental test data

Figure 4.1 illustrates the experimental data from *Kays and London, Compact Heat Exchangers (1998)* for an FCHX with the surface characteristics identified as 8.0 – 3/8T and fits within the scope of this study. The results from the experiments, were correlated using a best fit curve and presented

the relationship between the Colburn- and friction factors on the airside (Kays and London, 1998). The physical HX design parameters are illustrated in Figure 3.4 found in Chapter 3 as a visual illustration to support the process of model construction.

For the simulation results to be comparable to the experimental data, a methodology was developed to convert the simulation data into the Colburn j-factor and Fanning friction factor, in the next section.
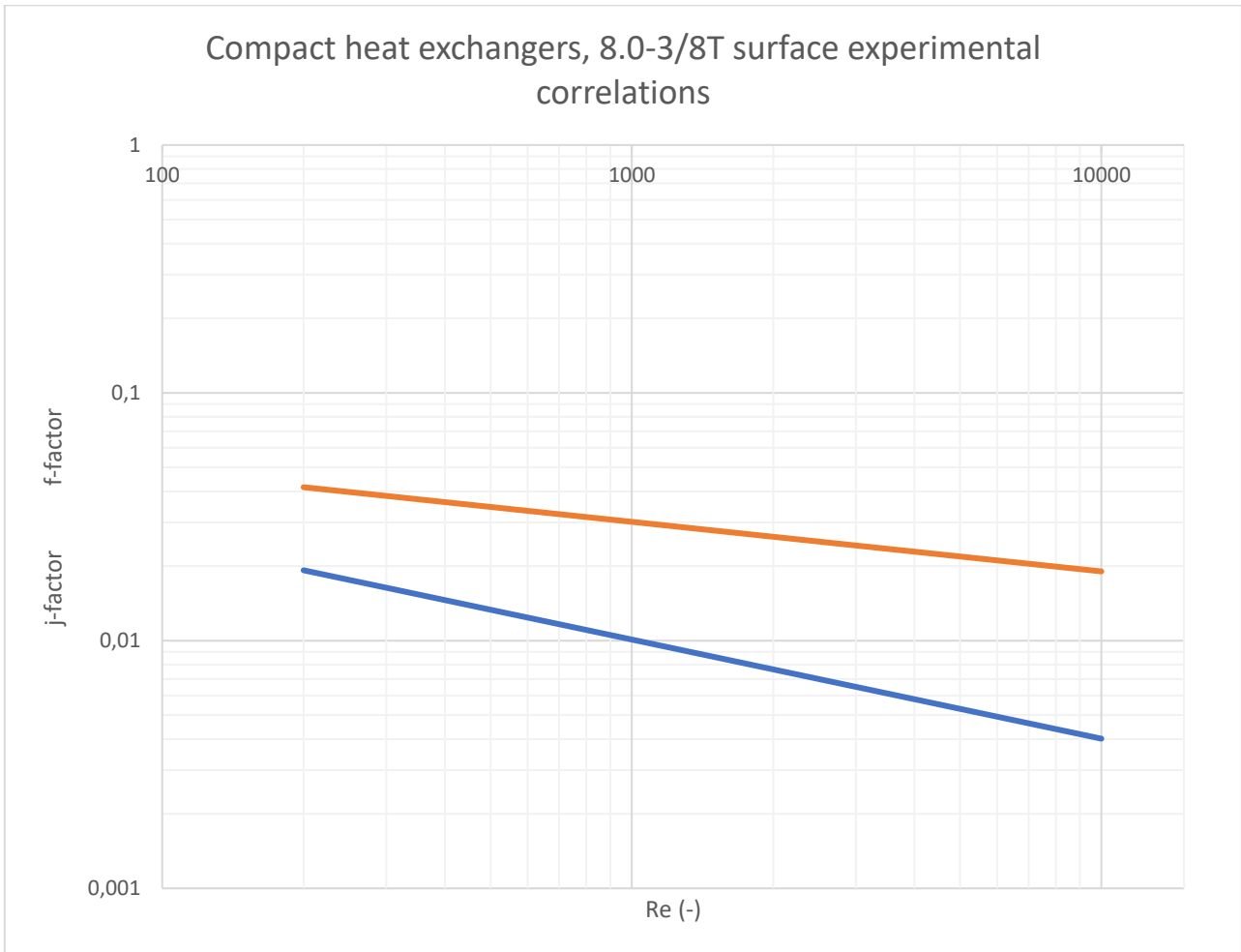
Figure 4.1: Heat transfer and friction factor for a circular tube-continuous fin HX, surface $8.0 - 3/8T$ from *Kays and London*, *Compact Heat Exchangers* (Kays and London, 1998)

4.3. Methodology to convert simulation data for comparison

Calculations to convert the simulation data is needed to be able to compare the heat transfer coefficient and pressure drop data with the Colburn *j*-factor and the Fanning friction factor (*f*-factor) experimental results from *Compact Heat Exchangers (1998)*. The following methodology was followed:

The air properties in the simulations were set to be dependent on the air temperature, as stated in Chapter 3 (Table 3.7). To calculate the Colburn j and friction factors from the simulation data, the air properties needs to be kept constant and be a representation of the entire air flow within the FCHX

model (Gu *et al.,* 2017). Gu *et al.,* 2017 stated that a bulk air temperature value can be used as the air flow representation and is determined as the average value between the inlet and outlet air temperatures (Gu et al., 2017). Table 4.1 contains the air properties.

Table 4.1: Simulation air properties

Air property	Value
Average air flow temperature	60 [℃]
Density	$1.059 \, [kg/m^3]$
Dynamic Viscosity	$2.008 \times 10^{-5} \, [kg/m.s]$
Specific heat capacity	$1007 \, [kJ/kg.K]$
Thermal conductivity	$0.02808 \, [W/m.K]$
Prandtl number	$0.7202 \, [-]$

To calculate the Colburn j-factor, the heat transfer coefficient result from each simulation is used in equation 3.1 to 3.4. The frontal air velocity from the simulation input will also be needed as well as the free-flow area/frontal area (σ) value from Figure 3.5 in order to calculate the final j-factor value.

The Fanning friction factor (f-factor) is calculated using the pressure drop results from each simulation as well as the hydraulic diameter and HX flow length found from Figure 3.5. Equations 3.8 and 3.9 are used to calculate this value.

The experimental data from *Compact Heat Exchangers (1998)* is presented using a graph without a correlation function and is very helpful to perform single Reynolds number evaluations. For this study, however, to perform an accurate comparison for a large range of Reynolds number values a correlation function is needed. Correlation functions for both nondimensional numbers were found in literature for $Re > 800$ (similar to the experimental data air flow range), making the process of calculating the *j*-factor and *f*-factor for a certain Reynolds number straightforward and possible to graph Figure 4.1, illustrated by equations 4.1 and 4.2 (Fchart.com, 2018):

$$j = 0.15 Re^{-0.4} \tag{4.1}$$

$$f = 0.13 Re^{-0.2} \tag{4.2}$$

Before any TTI versus RS comparison simulations could be done, a computationally efficient model had to be ensured to prevent any excess computational expenses by maintaining an acceptable accuracy regarding model predictions. Section 4.4 is used to achieve this goal in terms of the model mesh.

4.4. Mesh independency tests (MIT)

A MIT was done for the plain fin TTI model followed by both plain fin and wavy fin RS models. It can be possible to create a simulation with converged RMS error values and monitor points (heat transfer coefficient and pressure drop) but the need to ensure the independence of the solution from the mesh resolution is critical. By not performing a MIT can lead to erroneous results within the CFD environment and could lead to very low to no confidence in the accuracy of results (Leap Australia, 2019). It is also used to ensure the computational expense is kept at a minimum to achieve acceptably accurate results as previously mentioned.

The meshing strategy was initiated using a coarse mesh (relatively large cell sizes) for each model type. The mesh cell sizes were then decreased giving rise to the number of cells and assuming better accuracy to follow in the simulation predictions. The number of prism layers was kept constant for all tests, therefore only varying the base- and surface sizes of each following mesh (Leap Australia, 2019).

During the meshing process it was realized the mesh could only be fine in the main region due to the predominantly thin fin region. A base size was set but manipulating the surface sizes the user could not create a valid mesh with a cell size larger than $2\,mm$ within the main region. When the mesh was generated with cell sizes larger than $2\,mm$ in this region, the software would automatically collapse fin volumes at different locations during the surface repair process. The surface repair tool is mainly used to repair certain geometry aspects which may have a negative influence on the simulation results like collapsed fin volumes and to imprint faces that share an interface.

The experimental data from *Compact Heat Exchangers (1998)* were used to perform the MIT being the only form of reference available to the author. It was decided to perform the MIT with the same conditions as in the experiments using an air flow Reynolds number and temperature of 1600 and $30\,[℃]$, respectively. The tube wall temperatures were kept constant at $110\,℃$ as the same approach was implemented by many other studies, such as Borrajo-Peláez *et al.,* 2010; Lu *et al.*, 2011; Erek *et al.*, 2005; Romero-Méndez *et al.,* 2000; Bhuiyan, Amin and Islam, 2013 and Panse, 2005.
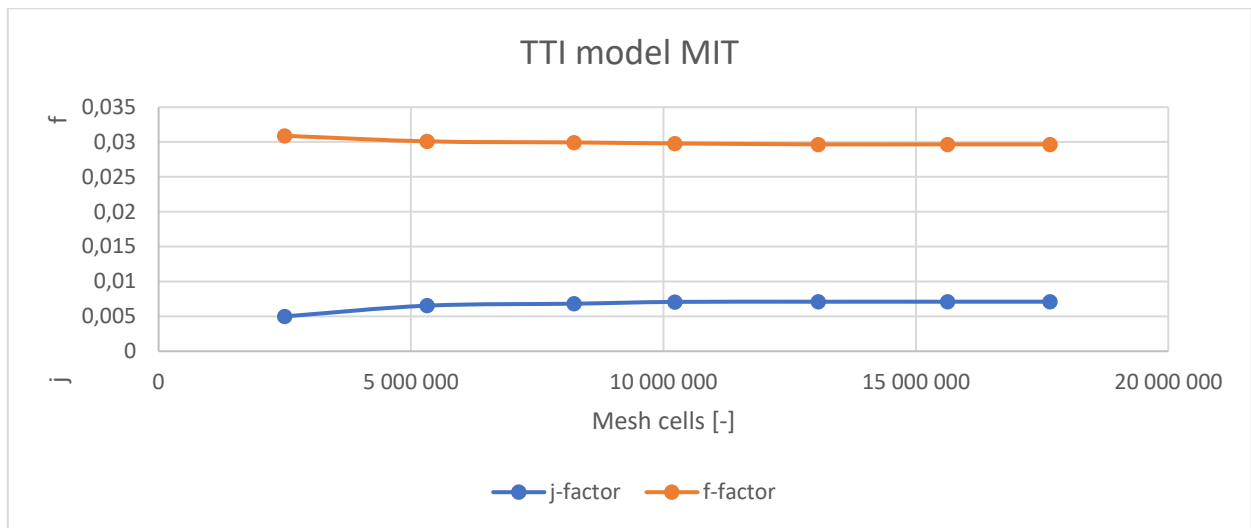
Figures 4.2 to 4.4 illustrate the MIT results.
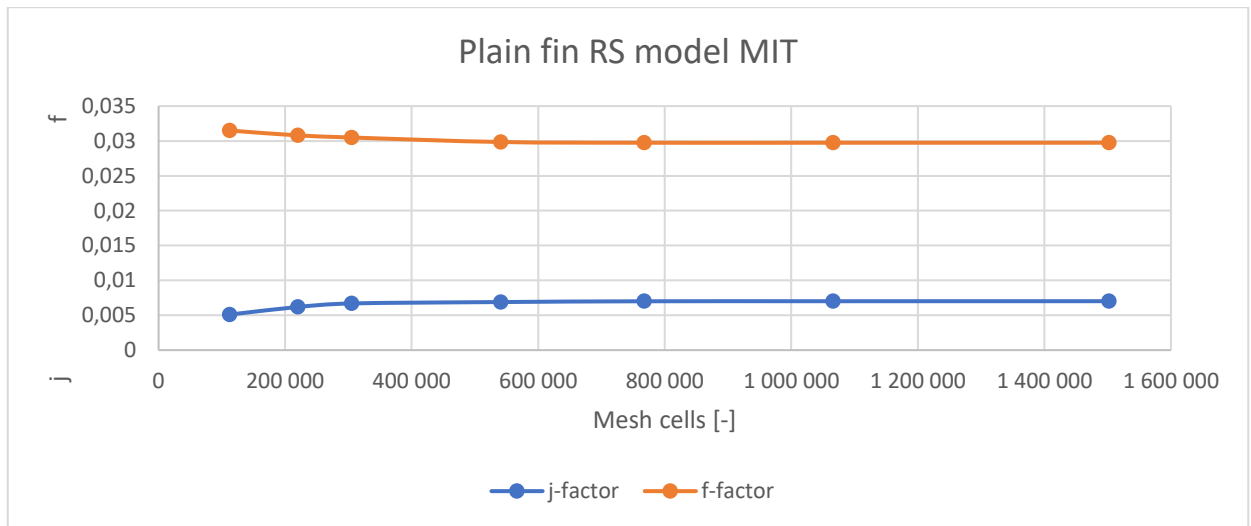
Figure 4.2: Plain fin TTI model MIT results

Figure 4.3: Plain fin RS model MIT results
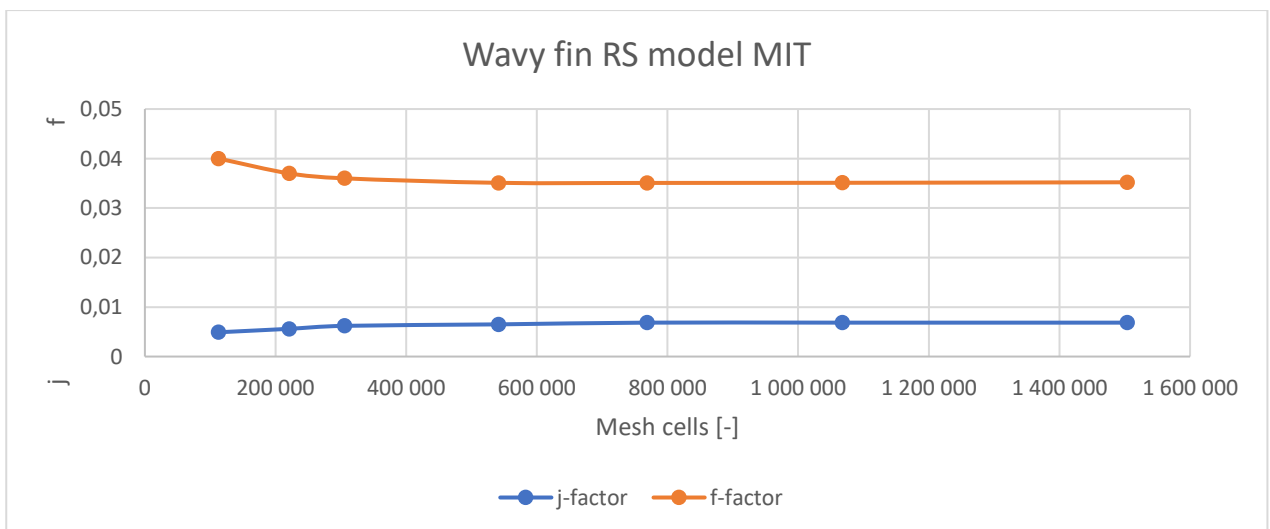
Figure 4.4: Wavy fin RS model MIT results

49

From the results illustrated by Figures 4.2 to 4.4 a decision was made to use $13,069,117$; $767,559$ and $768,654$ cells for the TTI, plain and wavy RS models, respectively. It was seen that the accuracy from this point did not improve with the imbalances decreasing to less than 1% and would therefore suffice for simulations to follow (Computationalfluiddynamics.com.au, 2019).

The MIT results indicate the TTI FCHX model required a substantial number of cells more than the RS models, as the larger geometric size of the model contributed to this factor. It was also seen that the wavy fin RS model did not require a large number of cells more than the plain fin RS model and this could be due to the slightly longer wavy fin length. The wavy fin RS model results is applicable for the simulations done in Chapter 5.

4.5. Simulation inputs

The inputs used for the simulations are tabulated using Table 4.2 including the temperature dependent air properties from Table 3.8. The air flow values were chosen to be a representation of what is found in the industry and includes the laminar, transitional and turbulent flow regimes. It can be seen that the simulated air flow starts at $Re = 100$ which is below the experimental test data range and might prove to be less accurate than air flow simulations for $Re > 800$ due to the correlation functions not taking this lower range into consideration. Simulations for flow from $Re > 3500\ to\ 4000$ was found to require unsteady implicit simulations and therefore not done due to the extra computational expense required (as mentioned in Chapter 2) (Fjallman, 2013). The air inlet and tube wall temperature values are also kept constant similar to studies like Borrajo-Peláez *et al.,* 2010; Lu *et al.*, 2011; Erek *et al.*, 2005; Romero-Méndez *et al.,* 2000; Bhuiyan, Amin and Islam, 2013 and Panse, 2005 for both Chapter 4 and 5 as the effect will have little impact on the heat transfer.

Table 4.2: Full FCHX and segment simulation input values

Variable	Value
Air	
Inlet temperature	30 [℃]
Air flow	$100 - 3100$ Reynolds
Tube wall temperature	110 [℃]

4.6. Simulation results

In this section, the simulation results of the TTI- and RS FCHX models are tabulated, graphed and discussed.

4.6.1. Tabulated results

The TTI FCHX and RS models' (both comprising plain fins) simulation results are tabulated using Table 4.3 and Table 4.4, respectively and are graphed in section 4.7.2. The results for an air flow range of $100 \leq Re \leq 3100$ is illustrated. The tables consist of the simulation results in terms of the heat transfer coefficient and pressure drop and the error deviations for both the Colburn *j*-factors and the Fanning friction factors (*f*-factors) with reference to *Compact Heat Exchangers (1998)*. The Nusselt number was also included to provide an extra measure of the heat transfer.

Table 4.3: TTI FCHX model simulation results

Reynolds nr. [-]	Air velocity [m/s]	Simulation data		Dimensionless numbers		Goodness factor	Nusselt [-]	Absolute error deviation [%]	
		h [W/m^2.K]	ΔP [Pa]	j [-]	f [-]	j/f [-]		j [-]	f [-]
100	0,33808	15,20	1,12	0,020566	0,053173	0,386775	1,56	9,41%	2,74%
600	2,02847	44,05	28,49	0,009933	0,037572	0,2643854	4,51	8,79%	3,88%
1100	3,71886	65,51	84,17	0,008058	0,033025	0,2439921	6,70	5,14%	3,08%
1600	5,40925	84,03	160,01	0,007106	0,029674	0,2394639	8,60	2,45%	0,17%
2100	7,09964	101,03	258,06	0,006509	0,027781	0,2343051	10,34	0,10%	1,31%
2600	8,79003	117,42	378,04	0,006110	0,026550	0,2301497	12,02	2,36%	1,57%
3100	10,48042	133,60	514,95	0,005831	0,025440	0,2292112	13,67	4,98%	2,31%
							Average	4,75%	2,15%

Table 4.4: RS model simulation results

Reynolds nr. [-]	Air velocity [m/s]	Simulation data		Dimensionless numbers		Goodness factor	Nusselt nr. [-]	Absolute error deviation [%]	
		h [W/m^2.K]	ΔP [Pa]	j [-]	f [-]	j/f [-]		j [-]	f [-]
100	0,33808	15,00	1,20	0,020295	0,056971	0,3562401	1,54	10,61%	10,08%
600	2,02847	42,52	29,90	0,009588	0,039431	0,2431678	4,35	11,96%	9,03%
1100	3,71886	64,04	84,51	0,007877	0,033158	0,2375575	6,55	7,27%	3,50%
1600	5,40925	82,91	160,40	0,007011	0,029747	0,2356977	8,48	3,75%	0,07%
2100	7,09964	100,25	258,64	0,006459	0,027844	0,2319748	10,26	0,87%	1,09%
2600	8,79003	117,34	378,04	0,006106	0,026550	0,2299929	12,01	2,29%	1,57%
3100	10,48042	133,35	515,00	0,005820	0,025442	0,2287601	13,65	4,79%	2,30%
							Average	5,93%	3,95%

4.6.2. Graphs and discussion of results

In this section the results from Tables 4.2 and 4.3 are graphically presented and discussed. The nondimensional Colburn j-factor and Fanning friction results are illustrated in Figures 4.5 and 4.6, respectively followed by the error deviations in Figures 4.7.
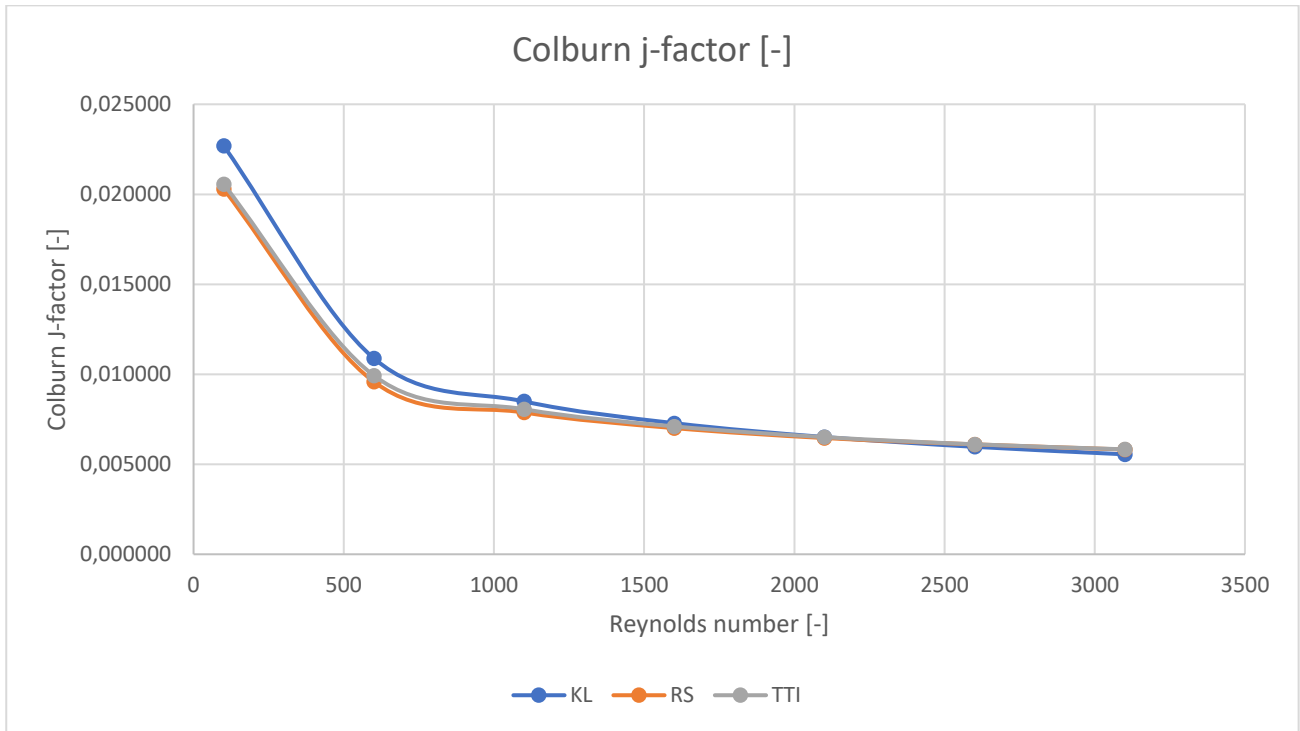
Figure 4.5: Colburn j-factor results comparison

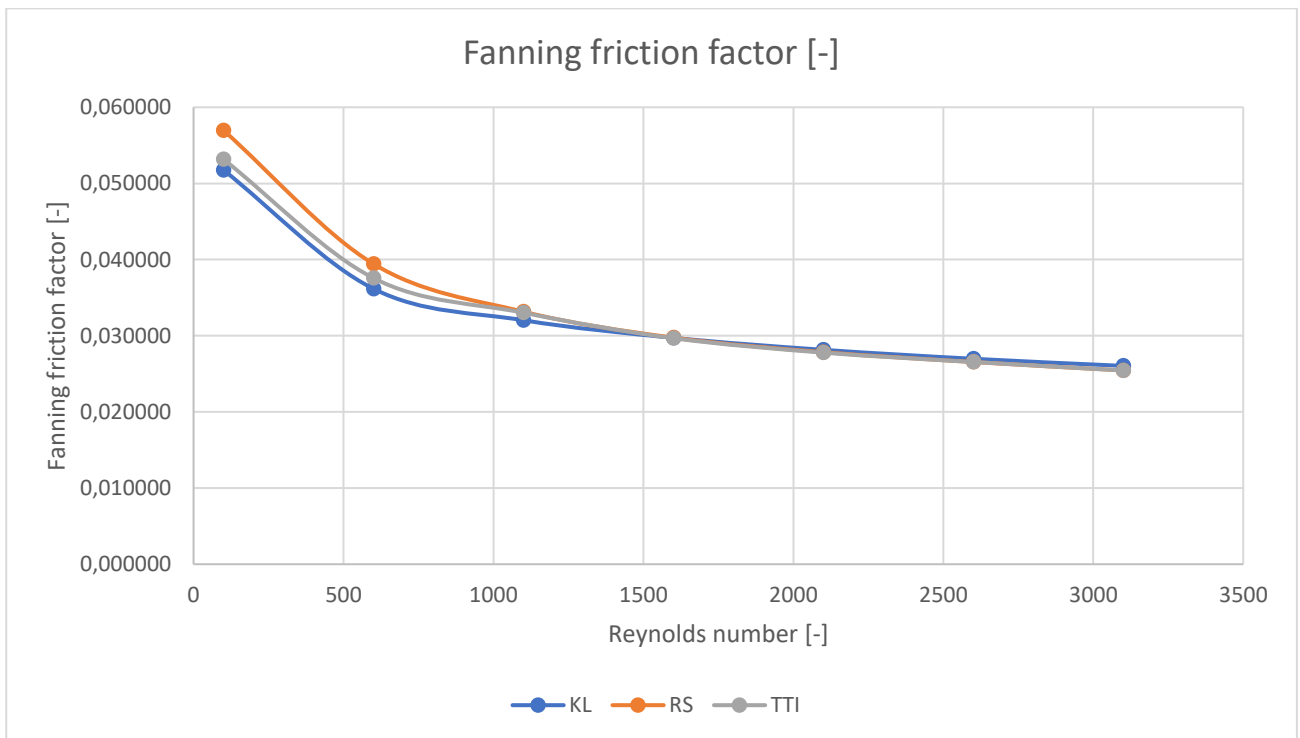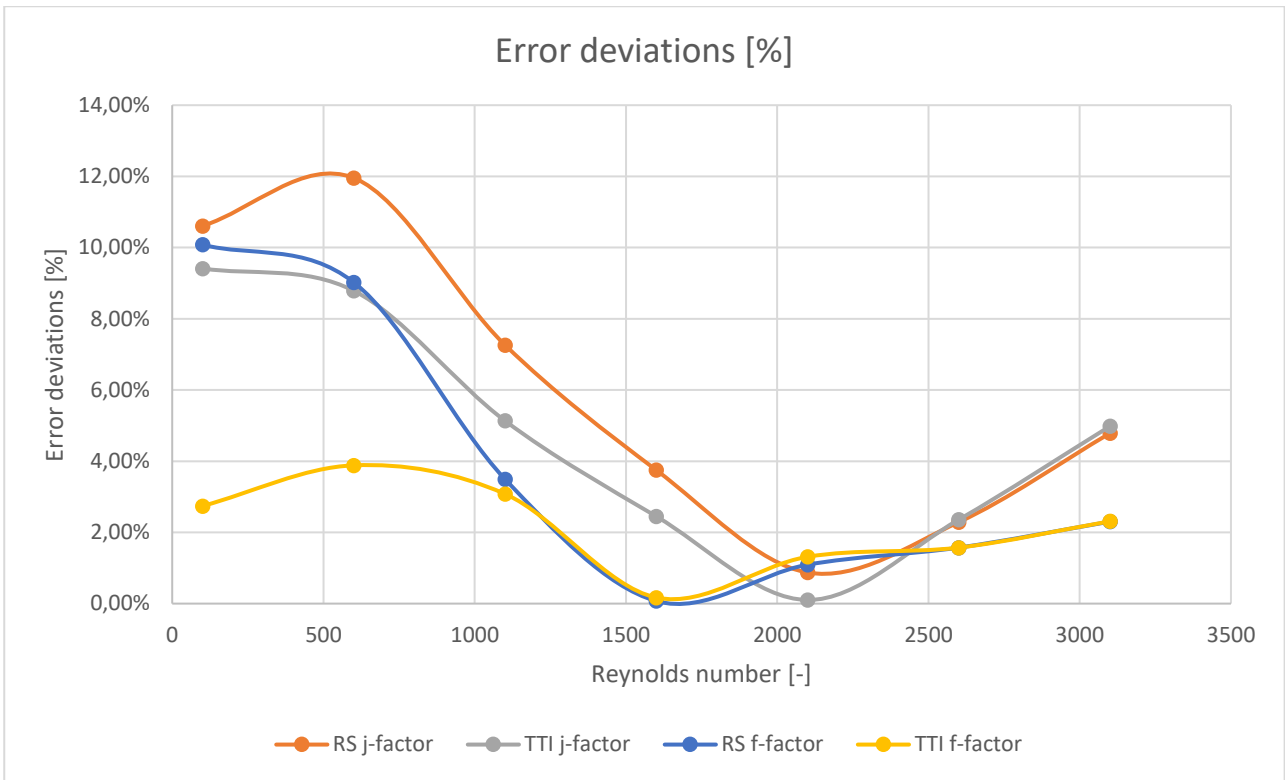**Figure 4.6: Fanning friction factor results comparison**

Figure 4.7: Error deviation [%] for TTI and RS model for j-factors and f-factors

Due to the information displayed by the Colburn j-factor and Fanning friction factors being abstract in nature, the Nusselt number and pressure drop results are displayed using Figure 4.8 and Figure 4.9, respectively.
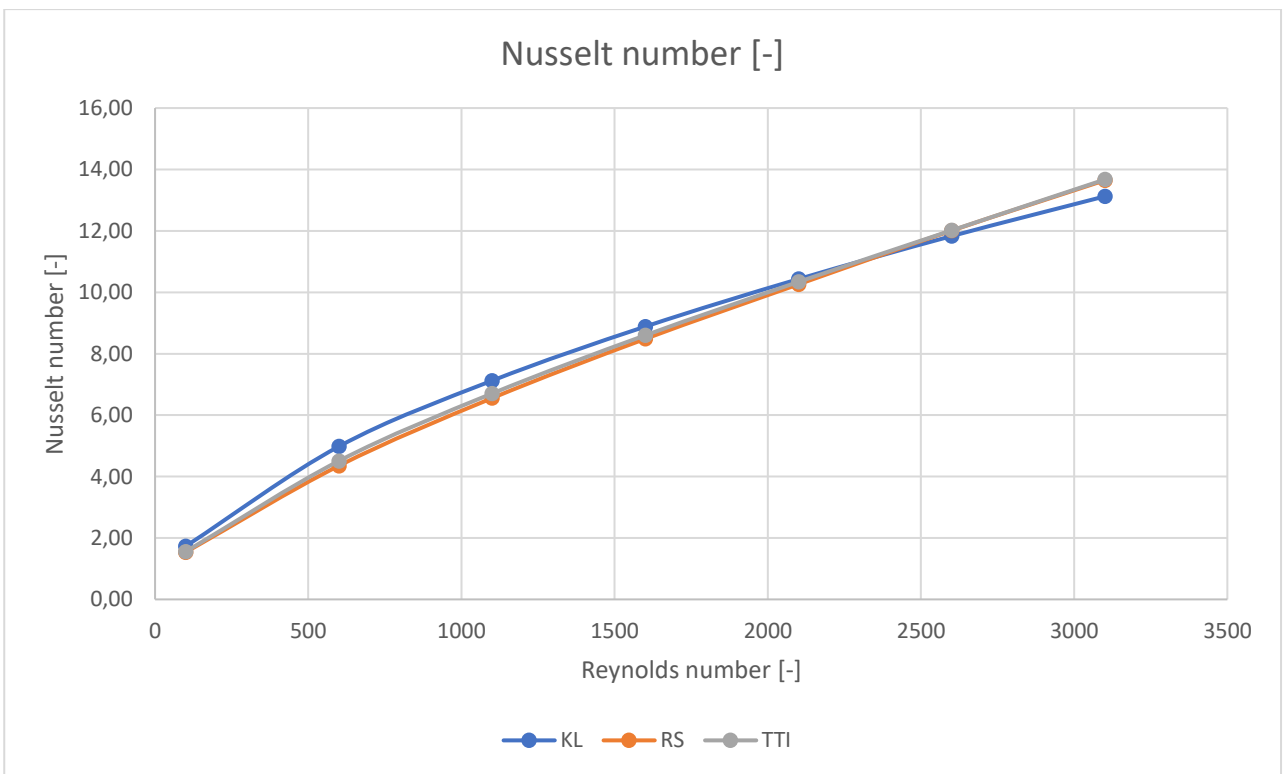
Figure 4.8: Nusselt number results comparison
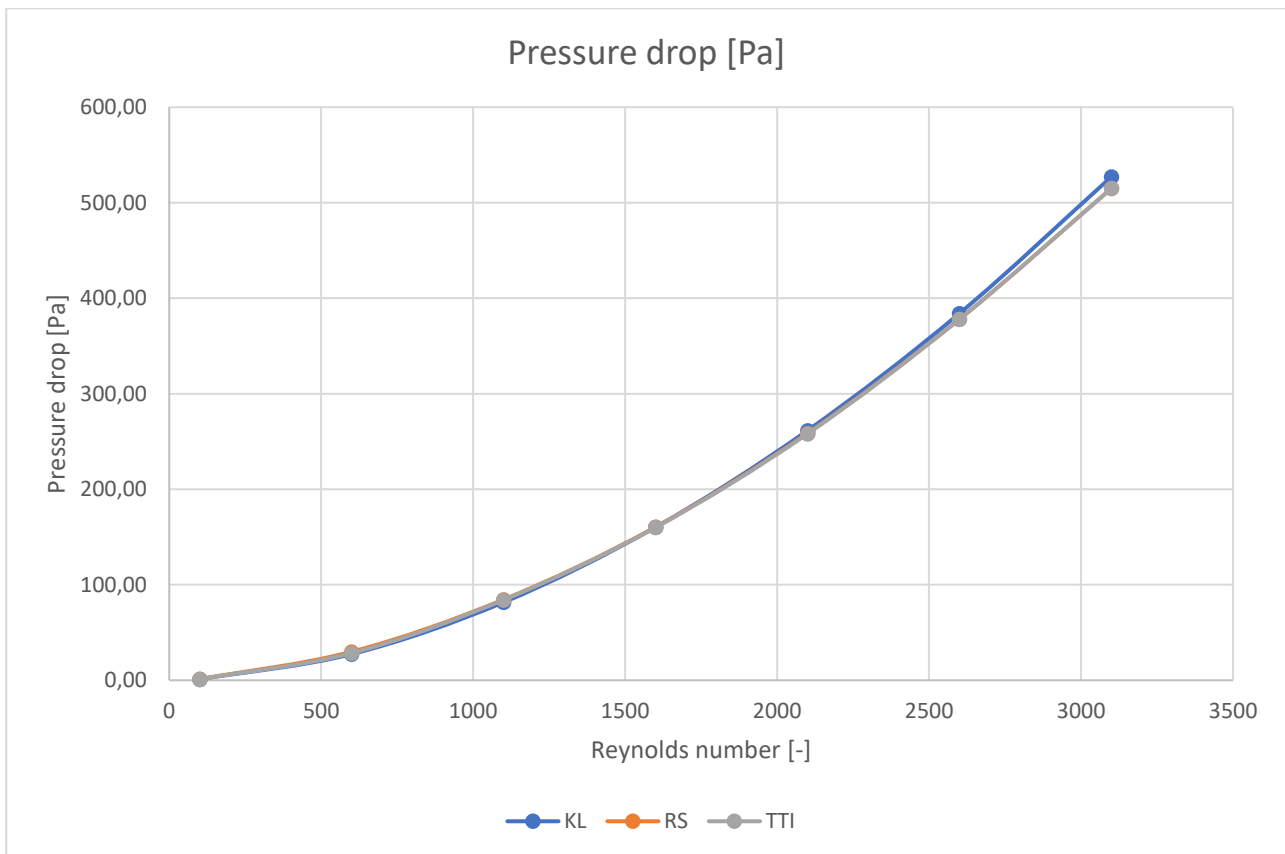
Figure 4.9: Pressure drop results comparison

From Figure 4.7 it becomes very evident that the TTI model has a marginally higher prediction accuracy in comparison to the RS model on average over the tested air flow range. On average, the TTI and RS models predicted the heat transfer performance with error deviations of 4.75% and 5.93%, respectively; and predicted the pressure drop performance with error deviations of 2.15% and 3.95%, respectively. The TTI model therefore showed an improvement of the heat transfer and pressure drop predictions by only 1.18% and 1.83%, respectively.

The simulation models proved to slightly underpredict the heat transfer performance and overpredict the pressure drop performance of the laminar and transitional flow regimes as compared to the experimentally tested FCHX. For the heat transfer predictions, this is true for an air flow up to $Re <2000$ and for the pressure drop predictions, up to $Re < 1600$. For air flow $Re > 2000$, the simulation models slightly over predicted the heat transfer performance; and for $Re > 1600$, the simulation model slightly underpredicted the pressure drop performance. The prediction accuracy after these air flow values continued to be accurate at an acceptable level.

Overall, the error deviations for both models were found to be somewhat larger for lower air inlet velocities and became steadily more accurate as the air inlet velocity was increased. An exception to this was the pressure predictions of the TTI model, which predicted the entire air flow range with acceptable accuracy. The poorest predictions of both model types, therefore, were in the laminar air flow regime with the heat transfer prediction accuracy reaching a low of 9.41% and 11.96% for the

TTI and RS models, respectively. The lowest prediction accuracy of the pressure drop values were 3.88% and 10.08% for the TTI and RS models, respectively keeping in mind the experimental data was performed for air flow with $Re > 800$ and the correlation functions were calculated for this range. This is critical information that will be further discussed in section 4.8 when concluding this chapter.

4.7. Model visual results

The following figures illustrate the various properties of the TTI and RS models for $Re = 1600$ to ensure consistency.

Figures 4.10 to 4.13 illustrate the velocity profile, temperature distribution, specific y+ heat transfer coefficient and pressure drop for the TTI model, respectively; and Figures 4.14 to 4.17 the same for the RS model. The "specific y+" term refers to the heat transfer coefficient that is calculated by using a fluid temperature at a specified y+ value and accommodates local fluid temperature variation effects (CD-Adapco, 2012). These illustrations were captured from the simulations performed using STAR-CCM+ and provides more insight into how the air flow patterns/turbulence are developed. Legends are provided at the bottom of each illustration.

The figures are followed by a discussion that will put focus on the comparison between the model types on the applicable properties and will aid in concluding the chapter.

4.7.1. TTI FCHX model

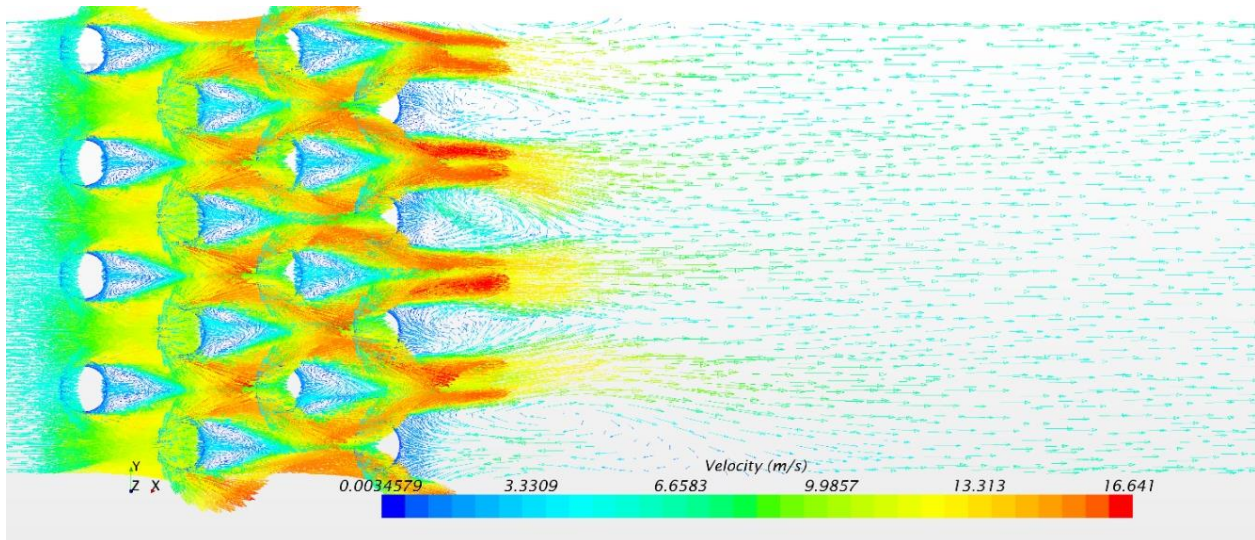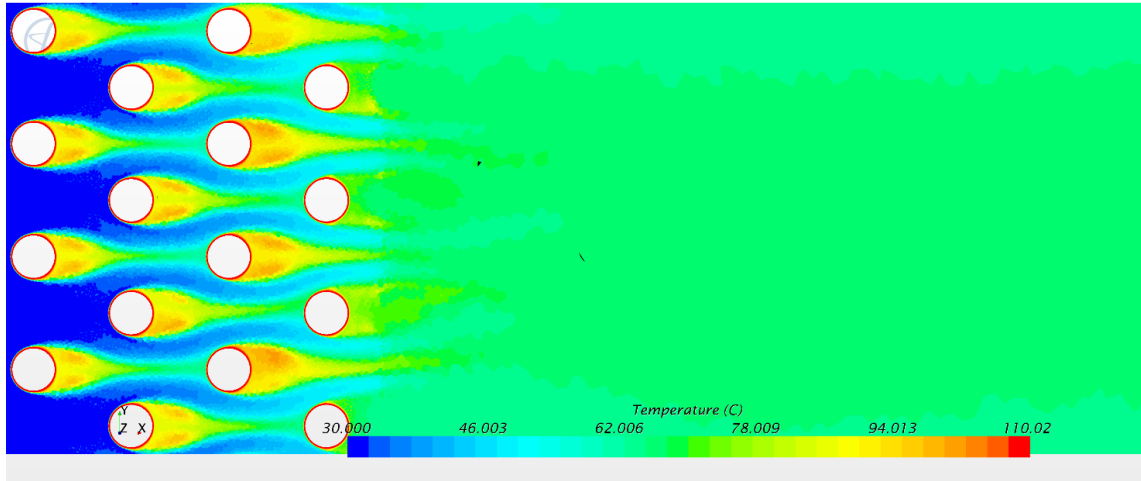Figure 4.10: Full FCHX model velocity profile

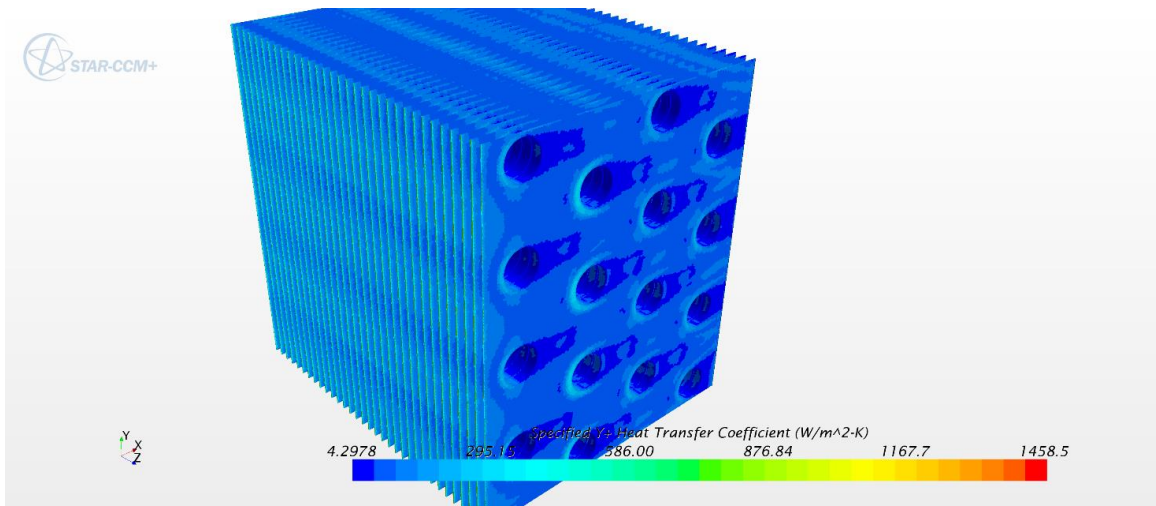**Figure 4.11: Full FCHX model temperature distribution**

Figure 4.12: Full FCHX model heat transfer coefficient
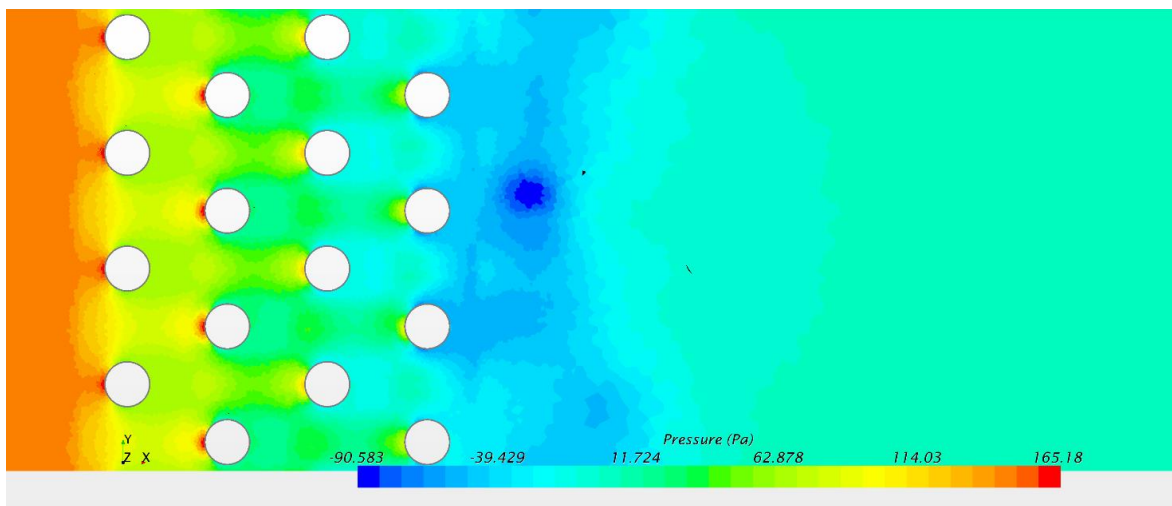

Figure 4.13: Full FCHX model pressure drop

4.7.2. Segment model
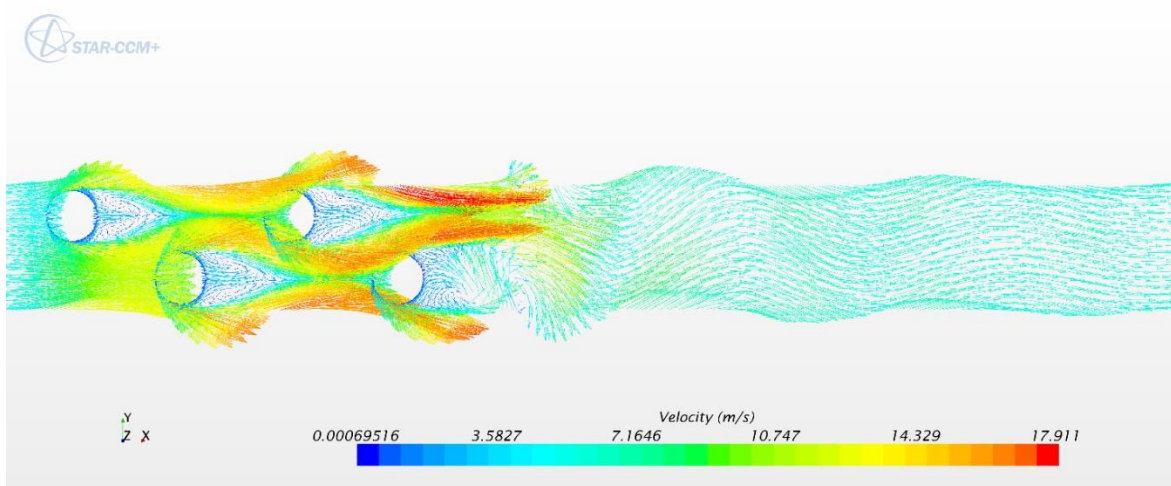
Figure 4.14: Segment model velocity profile
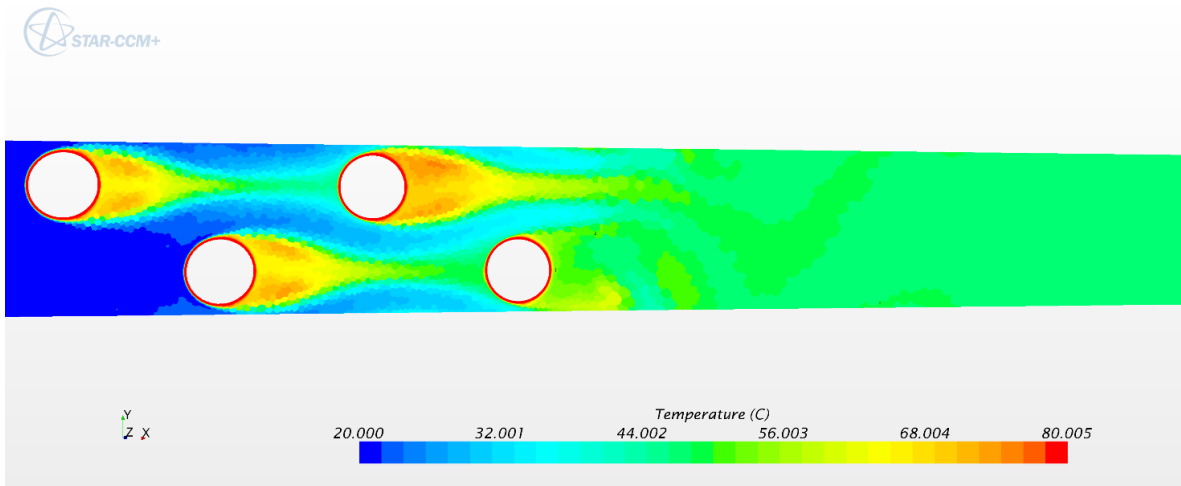
Figure 4.15: Segment model temperature distribution
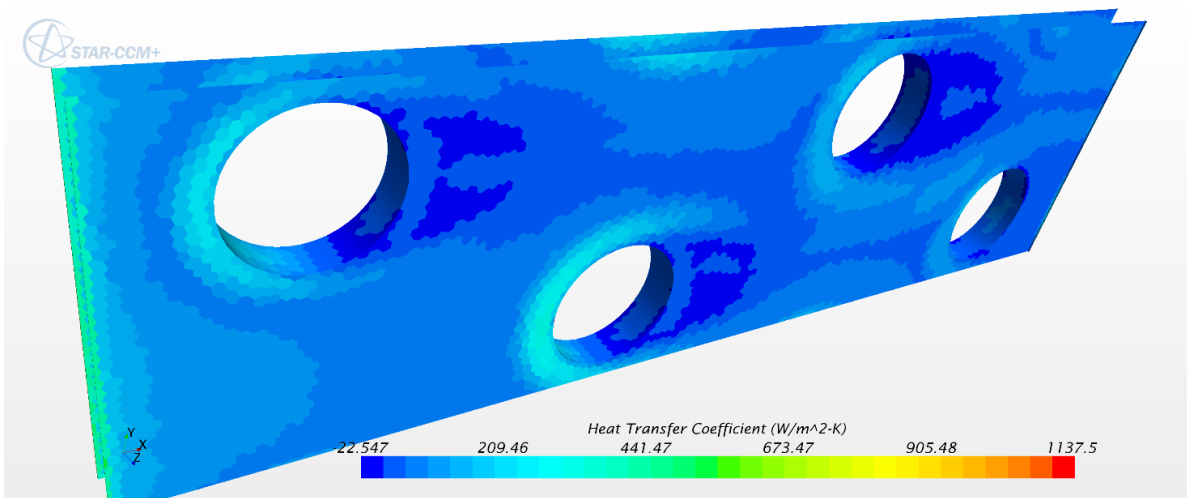
Figure 4.16: Segment model heat transfer coefficient
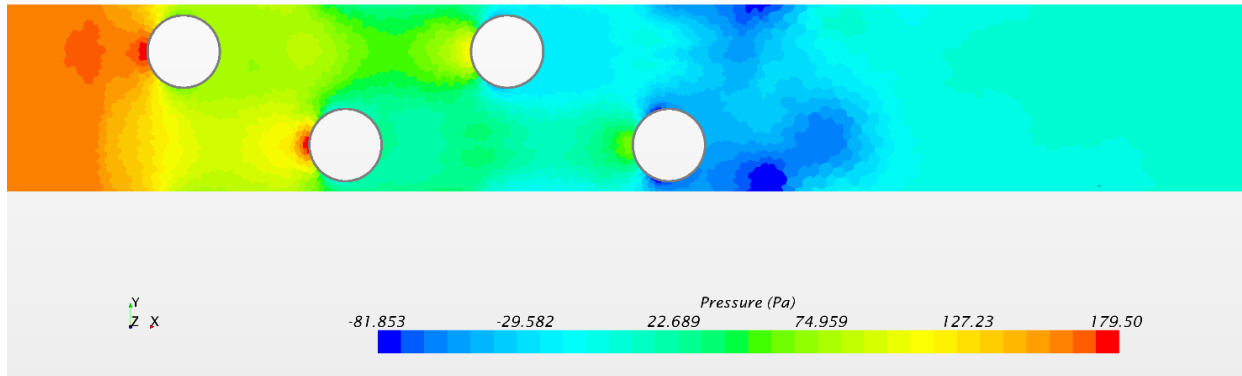
Figure 4.17: Segment model pressure drop

To ensure consistency for visual comparison, 2000 iterations were used for both model types ensuring the simulation residual errors were converged. To be able to generate acceptable results from both the simulations it was necessary to run the appropriate amounts of iterations in order to allow convergence of the residuals. All residuals converged (together with all residual values below 1^{-4} (Engineering.com, 2018)). The TTI FCHX model was found to take up to 6 times the amount of time needed for a RS model to converge. This was due to the extra number of cells in the TTI model.

From the velocity profile illustrations, the differences in air flow can be seen between the two model types. Flow patterns are very similar within the first three tube rows but show variations when air leaves the HX volume behind the fourth tube row. For the RS model the flow behind the HX also seem to consist of a slightly higher turbulence than the TTI model and can be associated to the absence of extra tubes in the transversal direction. The periodic boundaries still mimic the flow very well for the RS model type and is an acceptable approach. Behind the TTI model's last tube row, at the bottom of the HX the vortices seem to be stretched more than is found with the RS model and can be contributed to the effect of a wall-defined bottom surface.

The temperature distribution illustrates how the heat is transferred from the warm tube wall toward the colder air flowing across the coil surface and towards the downstream air region. The vortices behind the coil carried the highest air temperatures as slow to reversible flow occurred in these areas, increasing the opportunity for heat to be distributed downstream as air flow currents passed by the tubes. The flow patterns behind the tubes form similar vortices that has been extensively studied in the past for both instances and ultimately the recognisable shapes as found for turbulent flow around circular objects (Achenbach, 1968; White, 1991). It is evident that the cells are sufficiently small for both models to capture the vortices and therefore predict the heat transfer and pressure drop with an acceptable accuracy. Using the Polyhedral mesh as base is seen to be

effective due to the unpredictability of the flow direction and gradients. Therefore, the air downstream region behind the tubes experienced the best heat transfer from the tubes.

From Figures 4.12 and 4.16 (specified y+ heat transfer coefficient) the leading-edge effect can be clearly seen as the specific y+ heat transfer coefficient was found to be the highest on the fin front edges. The heat transfer capabilities of each model follow the same path as the vortices formed within the air flow and the heat transfer coefficient is found to be the lowest behind every tube due to recirculation. High heat transfer is also found in front of each tube with the highest heat transfer seen at the first and second tubes and is reduced for the third and fourth row tubes. Air is delivered at high impact and is forced over the face of the tubes in both longitudinal and transversal directions and correlates well with the pressure in the same areas as seen in Figures 4.13 and 4.17.

The maximum air velocity is found on the top and bottom edges of the tubes and the minimum at the front and back, the latter correlating with the pressure drop over the HX length. The maximum pressure for the FCHX is in front of the first tube row and the minimum behind the last as air in this region flows out of the HX volume. Every row of the FCHX is seen to drop the pressure in stages as indicated by the various colours.

4.8. Conclusion

In conclusion to this chapter, the prediction accuracy of the TTI FCHX- and RS simulation models were validated and compared by reference to *Compact heat exchangers, 3rd ed. (1998)* as written by W.M. Kays and A.L. London. It was seen that both the model predictions of the heat transfer coefficient and pressure drop, and in return the Colburn- and Fanning friction factors were acceptably accurate for an air flow of $Re > 800$ and higher (same range as experimental test data).

The TTI model showed a minor improvement of the heat transfer and pressure drop predictions by only 1.18% and 1.83%, respectively. When compared to the much faster simulation convergence of the RS model, the TTI model's extra time and computational expense is not justifiable. Hence, the RS model proved to be an excellent alternative to the TTI FCHX model to save computational expense and, therefore, simulation time.

In conclusion, the RS model predictions would be deemed adequate and suffice in the requirements as a representation of the TTI FCHX.

In Chapter 5 the study will further determine the validity of simulating a geometrically modified plain fin model as a representation of a wavy fin model.

Chapter 5 : Model comparisons

5.1. Introduction

In this chapter, the model prediction accuracy of a plain fin RS model with regards to a wavy fin RS model is evaluated and compared.

The dominant resistance within the thermal analogy of an FCHX is usually on the air side and may be 10 times as large as the resistance of the water (or secondary fluid) side, in practical applications (Panse, 2005). Enhanced surfaces have become very popular to improve the overall heat transfer performance in air-cooled HXs but also bring forward a higher pressure drop which is not desired, as previously mentioned. Common types of enhanced fin types used in FCHXs are wavy or corrugated fin, louvered fin, offset strip fin and the perforated fin (Panse, 2005). The wavy or corrugated fins are a popular type of enhanced fin surface that have been developed to improve heat transfer performance. The surface of the wavy fins can lengthen the air flow path and bring about better air flow mixing and, therefore, increase heat transfer performance compared to a plain plate fin type. However, the higher heat transfer performance of the wavy fin surface is accompanied by a higher pressure drop as compared to the plain plate fin type (Panse, 2005).

Hence, the use of wavy finned FCHXs are very common in the HVAC&R industry due to the many advantages it can offer. However, this fin profile could cause an inconvenience when trying to quickly construct a model in a typical CFD simulation. In the previous chapter it was concluded that the heat transfer and pressure drop predictions of a RS model would suffice as a representation of a TTI FCHX. This chapter will therefore make us of RS models incorporating plain and wavy fins.

The first step in the investigation between plain and wavy fins will be to evaluate and compare the heat transfer and pressure drop prediction similarities and differences, and whether or not a plain fin model approach would yield acceptable accuracy with regards to a wavy fin model. Construction of a plain fin model is thus deemed to be faster and less time consuming (due to a much simpler measurement process for construction purposes) and forms the basis of the rational in this chapter. If the study finds the plain fin model to be an acceptable approach, no further investigation is needed.

It is imperative to realize that the plain fin model approach can be expected to yield large inaccuracies with reference to a wavy fin model as found by Panse (2005). Geometrical modifications to the plain fin model could increase the model prediction accuracy and will be parametrically tested in the next step of the investigation, by variation of the fin pitch, longitudinal- and transverse tube pitches. The need to save model-construction time has therefore been recognised by construction of a geometrically modified plain fin model as representation of the heat transfer and pressure drop results of a wavy fin model, assuming a plain fin model's prediction accuracy is insufficient.

In this chapter, a wavy fin model is constructed with the same design parameters as the plain fin segment model in Chapter 4, but with a wavy fin profile with parameters similar to Panse (2005).

5.2. Model geometry and mesh

Figure 5.1 illustrates the model differences between the plain and wavy fin models as constructed using Solidworks. The plain fin model is the model in the top half and the wavy fin model in the bottom half of the illustration. From this figure it is clear that the only geometrical difference between the plain and wavy fin models is the fin type. The air was made transparent in this illustration for better visualisation of the Aluminium fins.
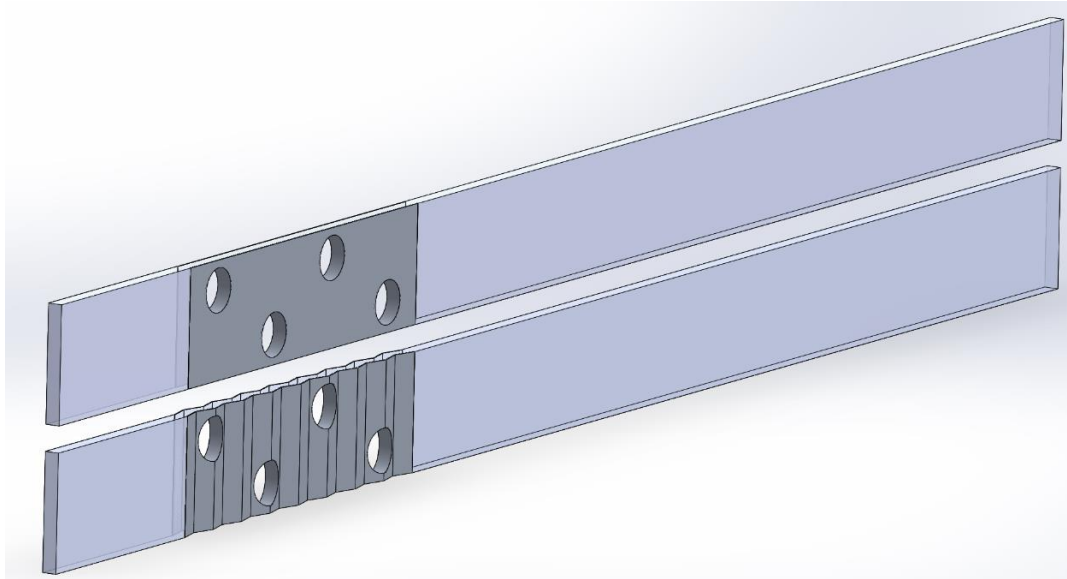
Figure 5.1: Plain and wavy fin model visual comparison (constructed using Solidworks)

Table 3.2 contains the model dimensions and the model nomenclature is illustrated using Figure 5.2. The waviness angle and waviness height (also known as waffle height) are used to define the characteristics of a wavy fin surface, as seen in the figure.
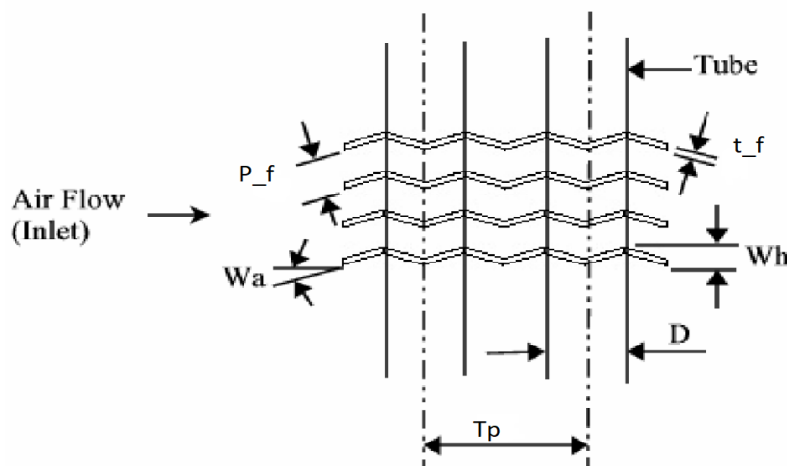
Figure 5.2: Wavy fin nomenclature (Panse, 2005)

All parameters are identical to the plain RS model in Chapter 4, but by means of a wavy fin profile instead of a plain fin profile. Hence, the only extra design parameters that had to be selected were the waviness angle (W_a) and waviness height (W_h) of the fins, which were 13.52° and 1.5 mm, respectively. The before mentioned parameters affect the total fin length constant in the main air region for both the plain and wavy fin models. No other parameter was changed to determine the impact of the waviness on the heat transfer and pressure drop.

The model was constructed by the same process as the plain fin RS model described in Chapter 3. Figure 5.3 illustrates the wavy fin RS model geometry after the geometry had been successfully constructed and Figure 5.4, the implemented mesh. Table 3.6 contains the mesh values that were chosen for the wavy fin RS model. It can be seen that the values are identical to the plain fin segment model and was tested using an MIT. The number of cells chosen for this model is 768,654.
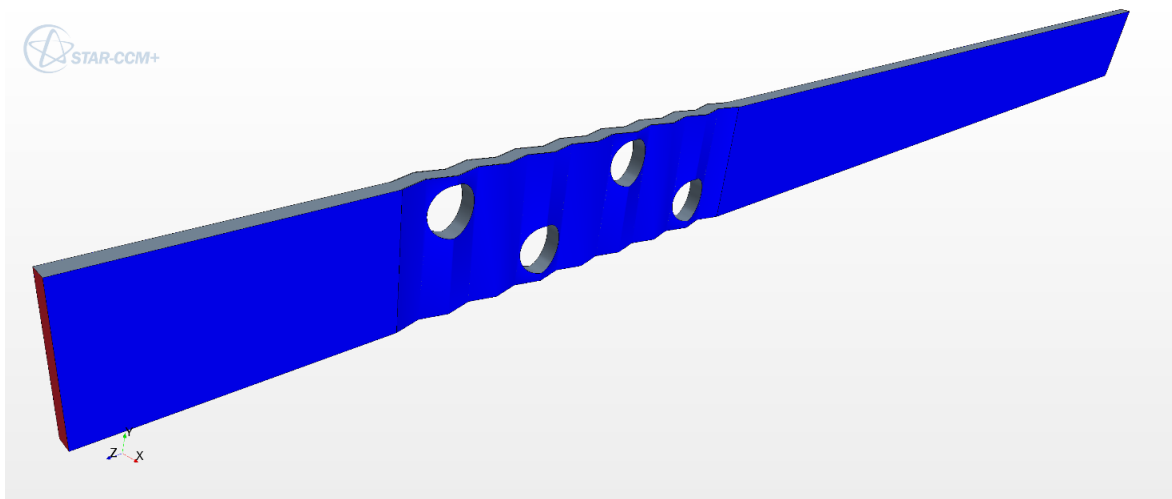
Figure 5.3: Wavy fin segment model created using Star-CCM+
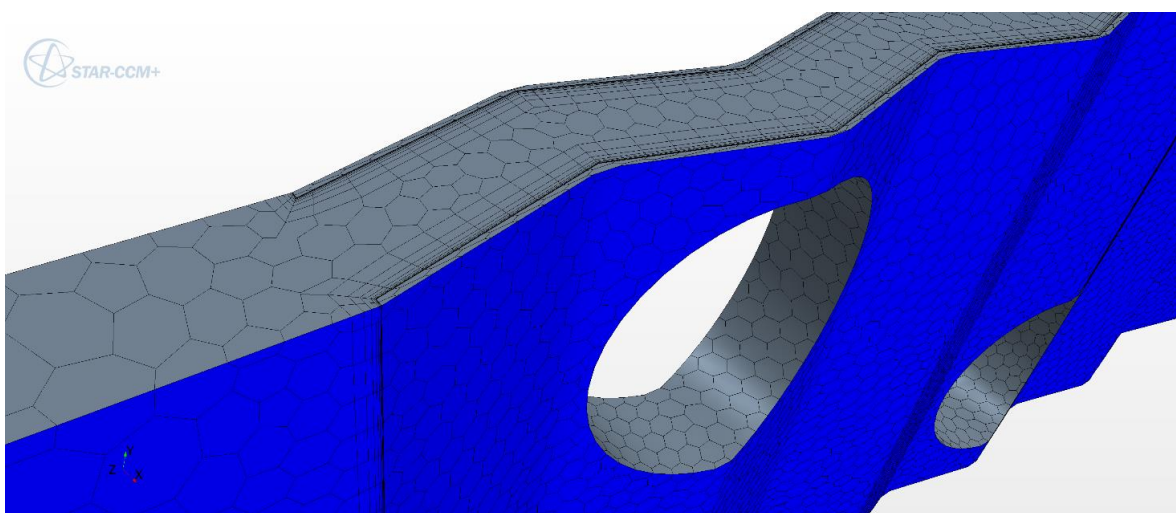
Figure 5.4: Wavy fin segment model mesh

5.3. Plain and Wavy fin simulation results and discussion

In this section, the results of the wavy fin RS model are illustrated and compared to the plain fin RS model. Simulations in this chapter were performed using the same Reynolds air flow range (based on fin spacing) as implemented in Chapter 4, with differences for the air and tube wall temperatures which is kept constant at $20℃$ and $80℃$, respectively.

5.3.1. Tabulated results and discussion

The results of the wavy fin and plain fin RS models' simulations are tabulated using Table 5.1 and Table 5.2, respectively. The table consists of the air inlet variables (air inlet velocity and Reynolds number), the heat transfer results in terms of the heat transfer coefficient, Colburn j-factor and Nusselt number, and the pressure drop also in terms of the Fanning friction factor. Table 5.2 includes the absolute deviation of the heat transfer and pressure drop with regards to the wavy fin model.

Table 5.1: Wavy fin tabulated results

Reynolds number [-]	Air velocity [m/s]	Simulation data		Dimensionless numbers		Nusselt number
		h [W/m^2.K]	ΔP [Pa]	j [-]	f [-]	[-]
100	0.30956	16.00	2.20	0.018328	0.081792	1.64
600	1.85733	47.00	43.00	0.008973	0.044407	4.81
1100	3.40511	72.61	124.50	0.007561	0.038254	7.43
1600	4.95288	95.67	241.50	0.006849	0.035072	9.79
2100	6.50066	116.71	396.57	0.006366	0.033433	11.94
2600	8.04843	136.55	589.54	0.006016	0.032423	13.97
3100	9.59621	155.21	799.00	0.005735	0.030911	15.88

Table 5.2: Plain fin tabulated results

Reynolds number [-]	Air velocity [m/s]	Simulation data		Dimensionless numbers		Nusselt number [-]	Absolute deviation [%]	
		h [W/m^2.K]	ΔP [Pa]	j [-]	f [-]		j [-]	f [-]
100	0,33808	15,00	1,60	0,017183	0,059485	1.54	6.25%	27,27%
600	2,02847	42,52	30,40	0,008118	0,031395	4.35	9.53%	29,30%
1100	3,71886	64,04	84,51	0,006669	0,025966	6.55	11.80%	32,12%
1600	5,40925	82,91	160,40	0,005936	0,023294	8.48	13.34%	33,58%
2100	7,09964	100,25	258,64	0,005468	0,021804	10.26	14.10%	34,78%
2600	8,79003	117,34	378,04	0,005170	0,020791	12.01	14.07%	35,88%
3100	10,48042	133,35	515,00	0,004928	0,019924	13.65	14.08%	35,54%
						Average	11,88%	32,64%

Comparison between the models can only be done once the air flow type is identical and this is done by comparing results based on the Reynolds number. It can be seen that the air inlet velocity of the plain and wavy models is not the same for each respective Reynolds number. This is due to the fact that the value of the minimum free-flow cross-sectional area A_{min} is different for the plain and wavy fin models (found in equation 3.7) and requires a higher air inlet velocity from the plain fin model with respect to the wavy fin model to achieve the same Reynolds number values.

The results from Tables 5.1 and 5.2 indicate the effect of a wavy fin profile by referring to the heat transfer and pressure drop results, and can also be seen from Figures 5.6 and 5.7. As mentioned in Chapter 1, the addition of wavy fins increases the heat transfer performance of a FCHX, but also increases the pressure drop as penalty. This holds true for the results. The plain fin RS model, therefore, underpredicted the heat transfer and pressure drop results of the wavy fin RS model over the entire flow range.

It can also be noted that the prediction deviation between the plain and wavy RS models are found to be large over the entire air flow range. The average heat transfer prediction deviation was 11.88% and the pressure drop deviation, 32.64%. Therefore, the plain fin RS model does not provide results with acceptable accuracy with regards to the wavy fin RS model.

5.3.2. Graphs results and discussion
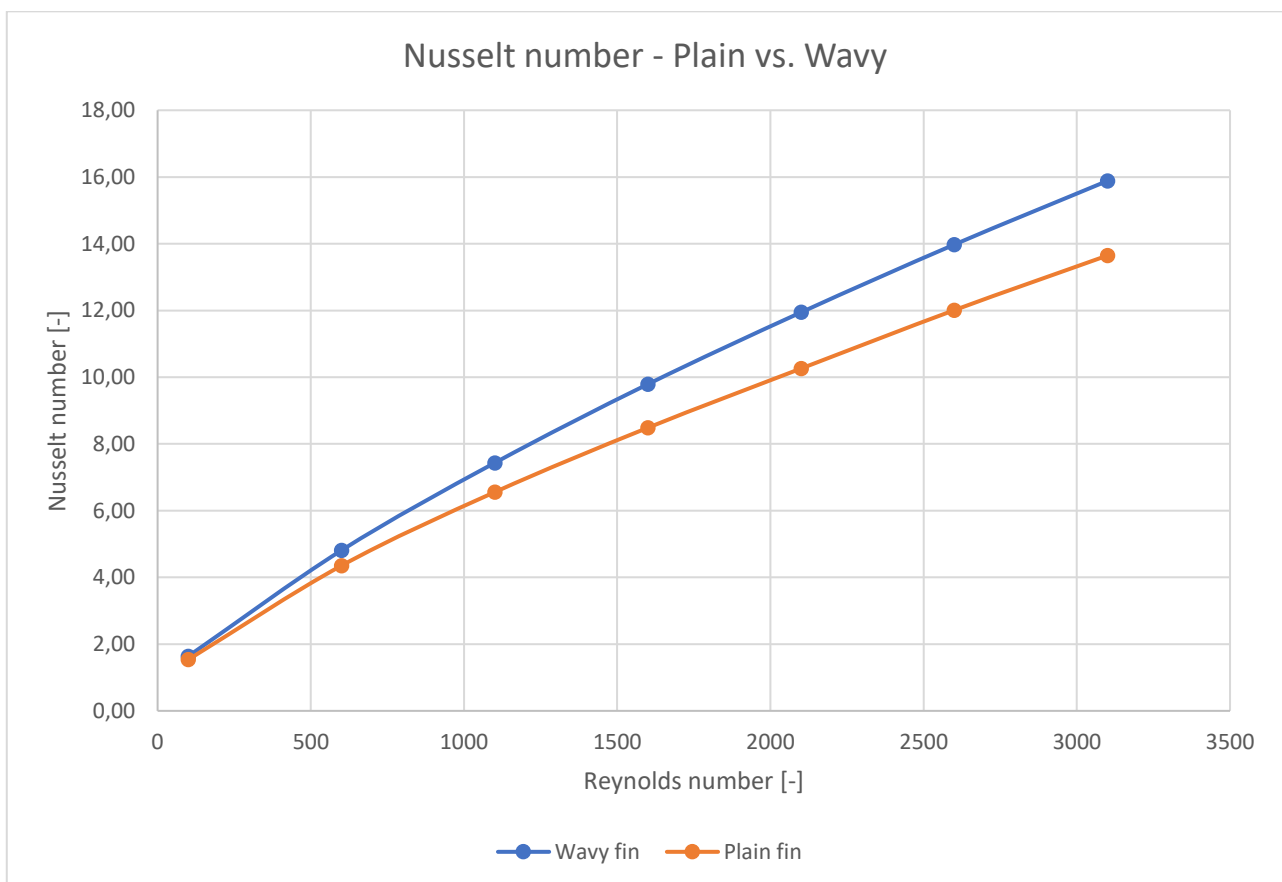
Figure 5.5: Plain vs. wavy fin models Nusselt number
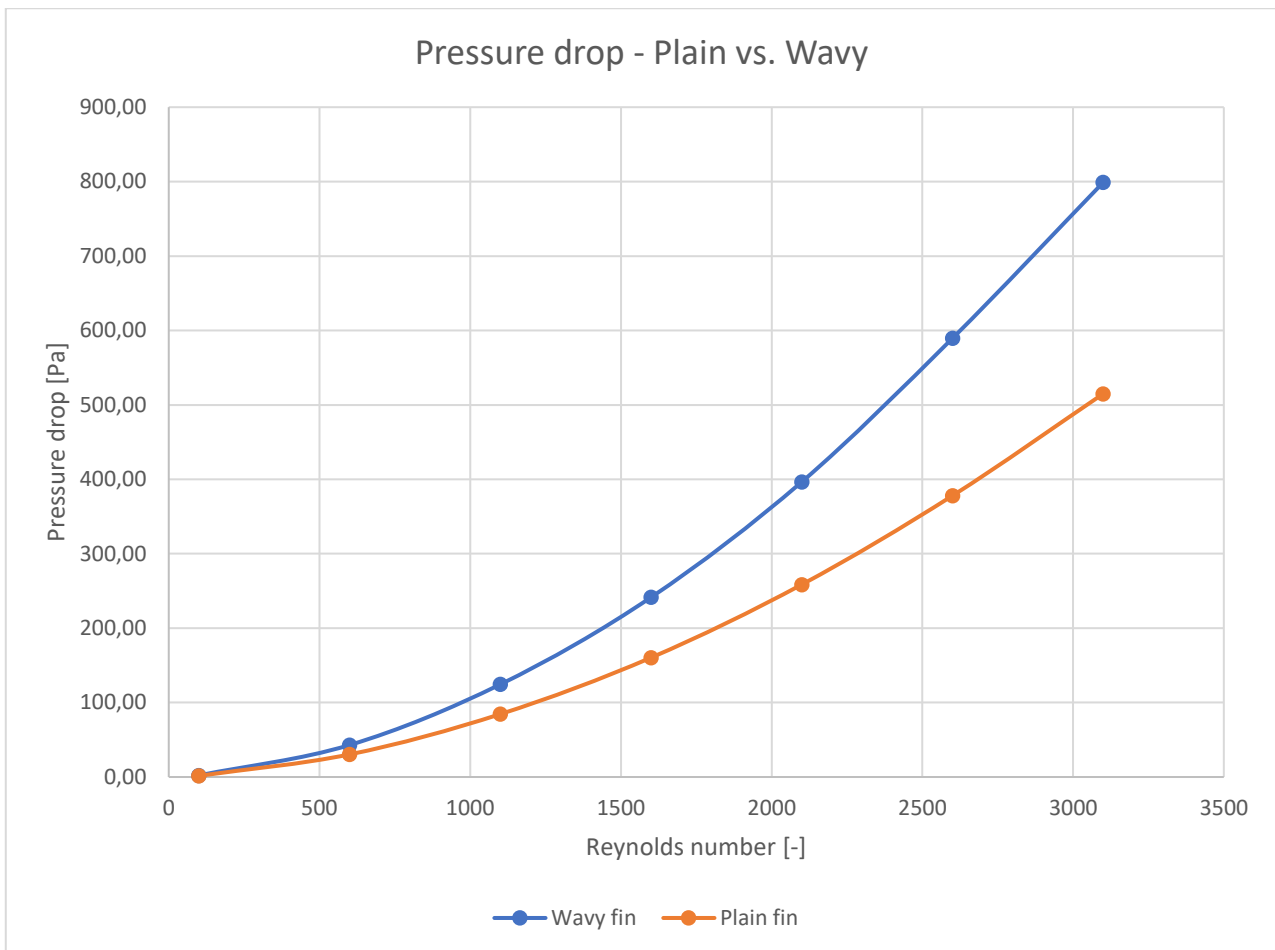
Figure 5.6: Plain vs. Wavy fin models pressured drop

As illustrated in Figures 5.6 and 5.7, the increase in heat transfer and pressure drop is clear when implementing a wavy fin profile compared to a plain fin profile over the same air flow rates. These figures also provide an illustration of the model prediction error when implementing a plain fin profile as opposed to a wavy fin profile. As the air flow rate is increased, the difference in heat transfer between the models is also slightly increased with a large increase seen in pressure drop difference. The heat transfer coefficient and Nusselt number results are found to follow the same rate of increase due to the unchanging hydraulic diameter (distance between fins) between the plain and wavy fin models.

5.3.3. Wavy fin RS model visual results

Figures 5.7 to 5.10 are the visual results for the converged wavy fin profile RS model. These visual results are comparable to Figures 4.14 to 4.17 for the plain fin RS model and give insights into the reasons behind the heat transfer and pressure drop increase.
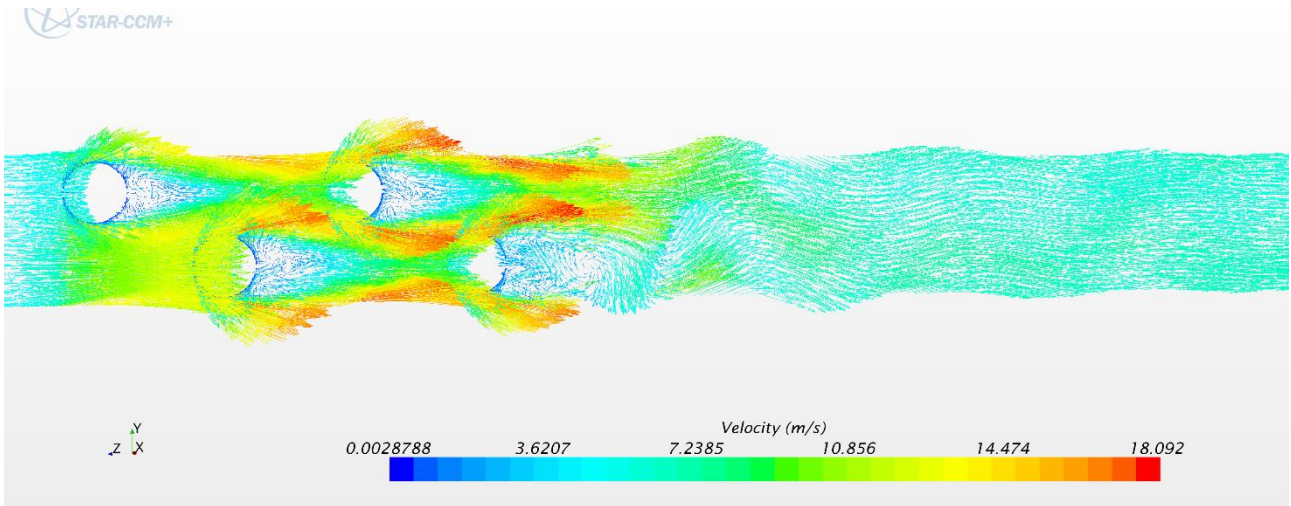
Figure 5.7: Wavy fin model velocity profile
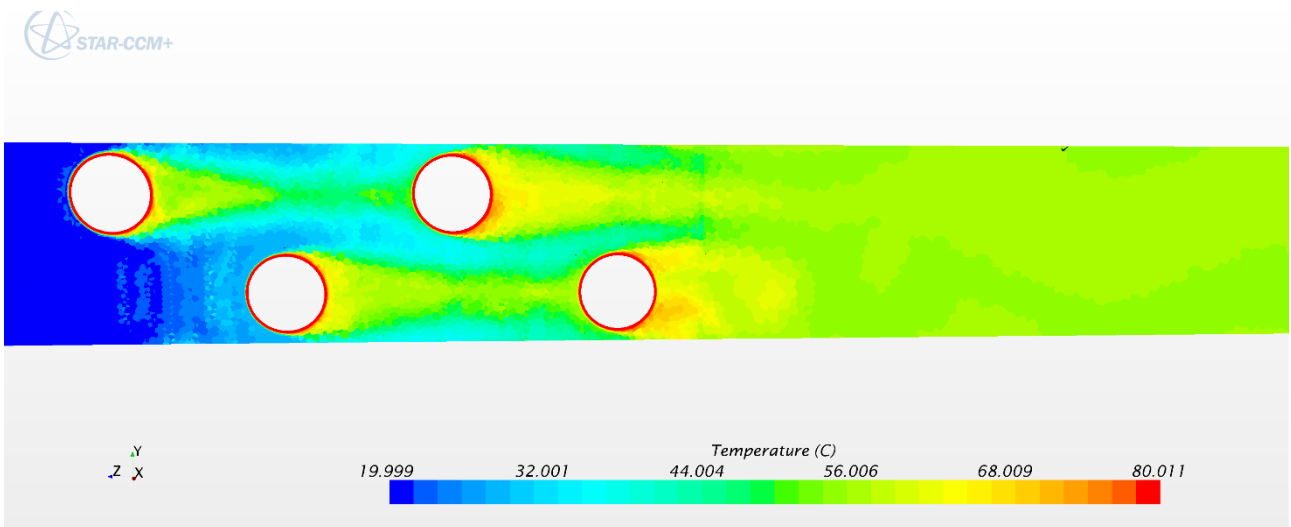
Figure 5.8: Wavy fin temperature distribution
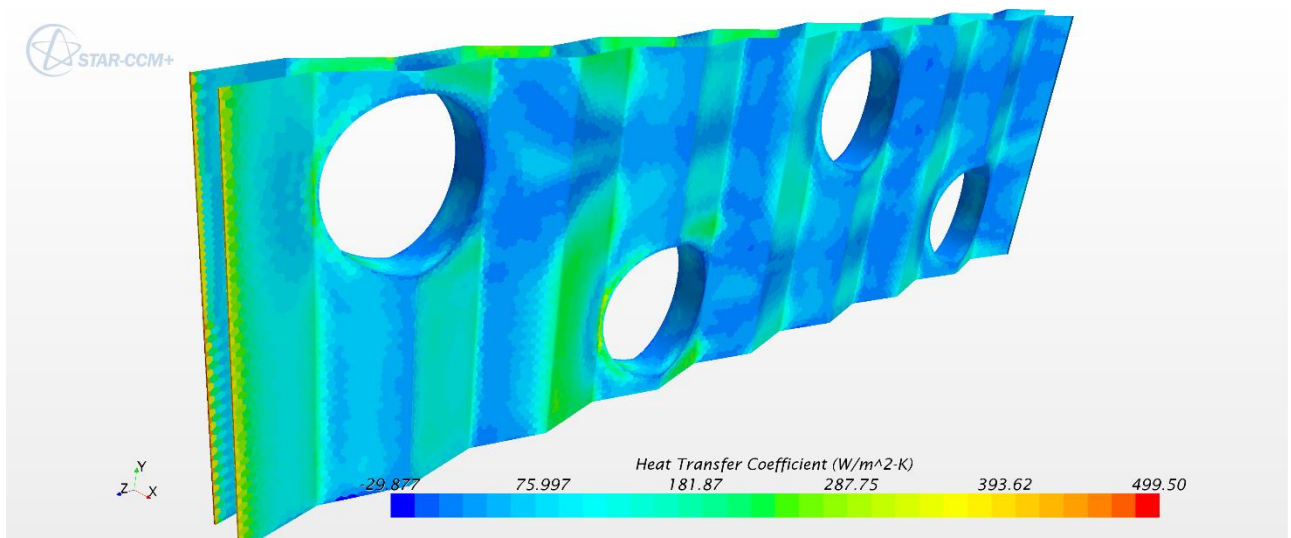
Figure 5.9: Wavy fin heat transfer coefficient
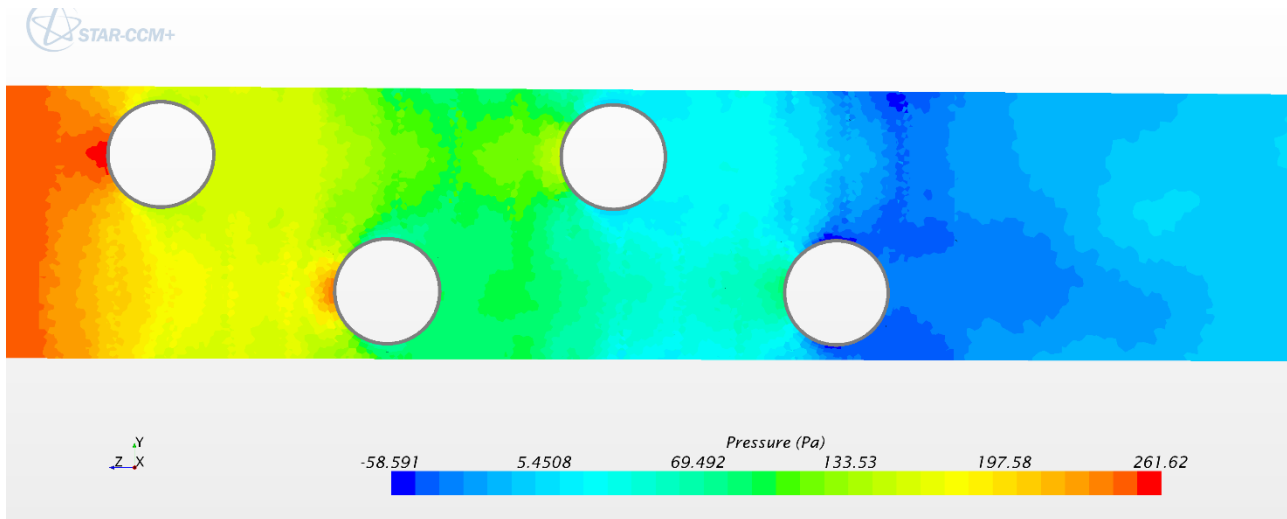
Figure 5.10: Wavy fin pressure drop

The visual results for the wavy fin RS model are found to be very similar to the plain fin RS model in Chapter 4. From Figure 5.7 it can be seen that the air flow turbulence generated within the main region is visibly higher compared to the plain fin model with maximum air velocities also increasing from $17.91\ m/s$ to $18.09\ m/s$.

The heat transfer coefficient illustrates a very interesting phenomenon in Figure 5.9 compared to Figure 4.16 of the plain fin RS model. The effects of the waviness become apparent as every alternating wave side of the fin profile experiences contrasting heat transfer values. It is seen that when the surface of the wave is directed perpendicular to the air flow direction, a much higher heat transfer is generated due to more direct contact between the aluminium fins and the air particles. The same overall flow structure is seen to develop behind the tubes as well as the leading fin edge, as discussed in Chapter 4.

Figure 5.10 illustrates the side view of the wavy fin segment model pressure drop. The pressure drop is comparable to the pressure drop in Figure 4.17 of the plain fin RS model, but is found to increase at a higher rate for the wavy fin model as expected.

As mentioned in section 5.3.1, the plain fin RS model does not provide acceptably accurate results as representation of a wavy fin RS model with the same parameters. Therefore, the effect of geometric variation for the plain fin RS model is tested and evaluated with regards to the wavy fin RS model results in the next section. The simulation tests are done parametrically, whereby the effect of each geometric variation is monitored and compared to the wavy fin RS model's results.

5.4. Plain fin modification parametric study

The representation of a wavy fin FCHX's heat transfer and pressure drop results through simulation are assumed to be possible by implementation of a modified plain fin RS model. The results in

section 5.3 is a very good indication of the heat transfer and pressure drop correlations of a wavy fin FCHX that is commonly found in the industry, and is used as a reference in this section.

The geometric parameters of the plain fin RS FCHX model from Chapter 4 will therefore be geometrically modified using a parametric approach to serve as the results of a wavy fin RS model. It is important to note the geometric parameters of the plain fin RS model from Chapter 4 is defined as the default plain fin RS model values for the purposes of this chapter.

The parametric approach used in this chapter entails the variation of only one geometric parameter of the default plain fin RS model at an instance for three variations (Cases I, II and III) per parameter group to determine the effect of each variation on the heat transfer and pressure drop results while keeping the other parameters unchanged. The same approach is followed for each parameter group in order to determine the most effective geometric parameter variation (between the fin pitch and tube pitches) with reference to the wavy fin RS model. By doing this, every parameter group has three independent case studies (adding to a total of nine case studies to be investigated). The different modification approaches and results are discussed in the following section.

A few design parameters can be modified in order to induce more turbulence and as a result increase the heat transfer and pressure drop in the same manner as the wavy fin profile of a wavy fin FCHX. These include increasing the fin pitch, increasing the fin thickness, decreasing the tube transverse and -longitudinal dimensions and increasing the tube diameter. Three of these design parameters, including increasing the fin pitch and decreasing the tube transverse and -longitudinal dimensions, were identified as the best possible solutions when referring to the study of Bhuiyan, Amin and Islam (2013). The variation values for each parameter group is listed below as Cases I to III:

- Fin pitch variations

    o *Default*: $3.17mm$ Case I: $3.5mm$ Case II: $4.25mm$ Case III: $5mm$

- Longitudinal tube pitch variations

    o *Default*: $22mm$ Case I: $20mm$ Case II: $17mm$ Case III: $14mm$

- Transverse tube pitch variations

    o *Default*: $25.4mm$ Case I: $24.5mm$ Case II: $23mm$ Case III: $21.5mm$

The values of each study case were selected to be within the geometrical restrictions of the RS model type. The following section illustrates the simulation results for these geometrical variations made to the plain fin RS model.

In the following section, the results for all parameter groups are tabulated, graphed and discussed.

5.4.1. Fin pitch variations tabulated results

Tables 5.3 to 5.5 illustrate the results for cases I, II and III of the fin pitch-modified plain fin RS model simulations and Table 5.6 the heat transfer coefficient and pressure drop absolute deviations with regards to the wavy RS model.

Table 5.3: Fin pitch modifications - Case I

Reynolds number [-]	Air velocity	Simulation data		Dimensionless numbers		Goodness factor	Nusselt	Absolute deviation [%]	
		h [W/m^2.K]	ΔP [Pa]	j [-]	f [-]	[-]	[-]	j [-]	j [-]
100	0,30665	14,50	1,30	0,018507	0,066860	0,27681	1,65	0,98%	18,26%
600	1,83992	39,48	23,80	0,008399	0,034001	0,247006	4,50	6,40%	23,43%
1100	3,37318	59,58	67,05	0,006913	0,028499	0,242578	6,79	8,57%	25,50%
1600	4,90645	76,84	126,40	0,006130	0,025394	0,241389	8,76	10,51%	27,60%
2100	6,43971	92,85	202,15	0,005643	0,023575	0,239378	10,59	11,36%	29,48%
2600	7,97298	108,60	296,57	0,005331	0,022563	0,236283	12,38	11,38%	30,41%
3100	9,50624	123,00	404,50	0,005064	0,021648	0,23394	14,03	11,70%	29,97%
							Average	8,70%	26,38%

Table 5.4: Fin pitch modifications - Case II

Reynolds number [-]	Air velocity	Simulation data		Dimensionless numbers		Goodness factor	Nusselt	Absolute deviation [%]	
		h [W/m^2.K]	ΔP [Pa]	j [-]	f [-]	j [%]	j [%]	j [-]	j [-]
100	0,25553	12,40	0,80	0,019322	0,074863	0,258098	1,73	5,42%	8,47%
600	1,53317	34,53	15,05	0,008968	0,039121	0,229226	4,81	0,06%	11,90%
1100	2,81082	52,44	41,86	0,007428	0,032373	0,229461	7,30	1,76%	15,37%
1600	4,08846	67,41	79,98	0,006565	0,029236	0,224552	9,38	4,15%	16,64%
2100	5,36611	80,56	127,84	0,005978	0,027127	0,220356	11,21	6,11%	18,86%
2600	6,64375	93,54	184,25	0,005606	0,025506	0,219794	13,02	6,82%	21,34%
3100	7,92139	106,09	256,00	0,005333	0,024928	0,213919	14,77	7,02%	19,35%
							Average	4,48%	15,99%

Table 5.5: Fin pitch modifications - Case III

Reynolds number [-]	Air velocity	Simulation data		Dimensionless numbers		Goodness factor	Nusselt	Absolute deviation [%]	
		h [W/m^2.K]	ΔP [Pa]	j [-]	f [-]	[-]	[-]	j [-]	j [-]
100	0,21468	10,70	0,50	0,020120	0,082217	0,244712	1,80	9,77%	0,52%
600	1,28805	30,40	9,47	0,009527	0,043255	0,22025	5,11	6,17%	2,59%
1100	2,36143	46,35	27,05	0,007923	0,036760	0,215534	7,79	4,78%	3,90%
1600	3,43481	59,96	52,76	0,007047	0,033889	0,207931	10,07	2,88%	3,37%
2100	4,50819	71,82	85,82	0,006431	0,031999	0,200964	12,06	1,01%	4,29%
2600	5,58156	82,56	124,27	0,005971	0,030228	0,197523	13,87	0,75%	6,77%
3100	6,65494	94,10	172,68	0,005708	0,029547	0,193175	15,81	0,48%	4,41%
							Average	3,69%	3,69%

Table 5.6 was added for the fin pitch variations parameter group due to the differences in absolute deviations between the heat transfer coefficient and Colburn j-factor, and the pressure drop and Fanning friction factor.

Table 5.6: Fin pitch heat transfer coefficient and pressure drop absolute deviations

Reynolds number [-]	Absolute deviation [%]					
	Case I		Case II		Case III	
	h [W/m^2.K]	ΔP [Pa]	h [W/m^2.K]	ΔP [Pa]	h [W/m^2.K]	ΔP [Pa]
100	9,38%	40,91%	22,50%	63,64%	33,13%	77,27%
600	16,00%	44,65%	26,53%	65,00%	35,32%	77,98%
1100	17,95%	46,14%	27,78%	66,38%	36,17%	78,27%
1600	19,68%	47,66%	29,54%	66,88%	37,33%	78,15%
2100	20,44%	49,03%	30,97%	67,76%	38,46%	78,36%
2600	20,47%	49,69%	31,50%	68,75%	39,54%	78,92%
3100	20,75%	49,37%	31,65%	67,96%	39,37%	78,39%
Average	17,81%	46,78%	28,64%	66,62%	37,04%	78,19%

When referring to Tables 5.3 to 5.5, it can be seen that an increased fin pitch increases the Colburn j-factor and friction factor but leads to a decrease in the heat transfer coefficient and pressure drop. For Case III, both the j- and f-factors are predicted with a deviation of 3.69%, but 37.04% and 78.19% for the heat transfer coefficient and pressure drop, respectively. The next section illustrates the graph results followed by a short discussion of the results.

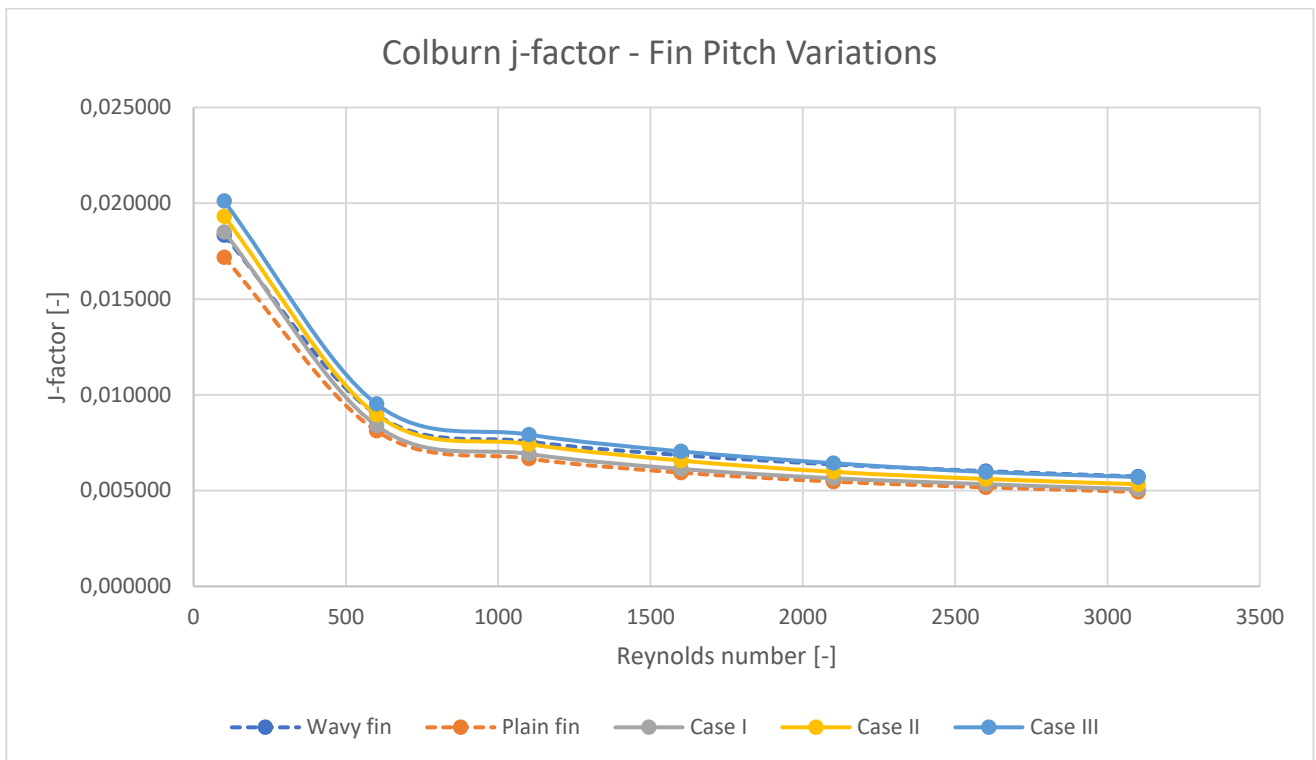## 5.4.2. Fin pitch variations graph results and discussion

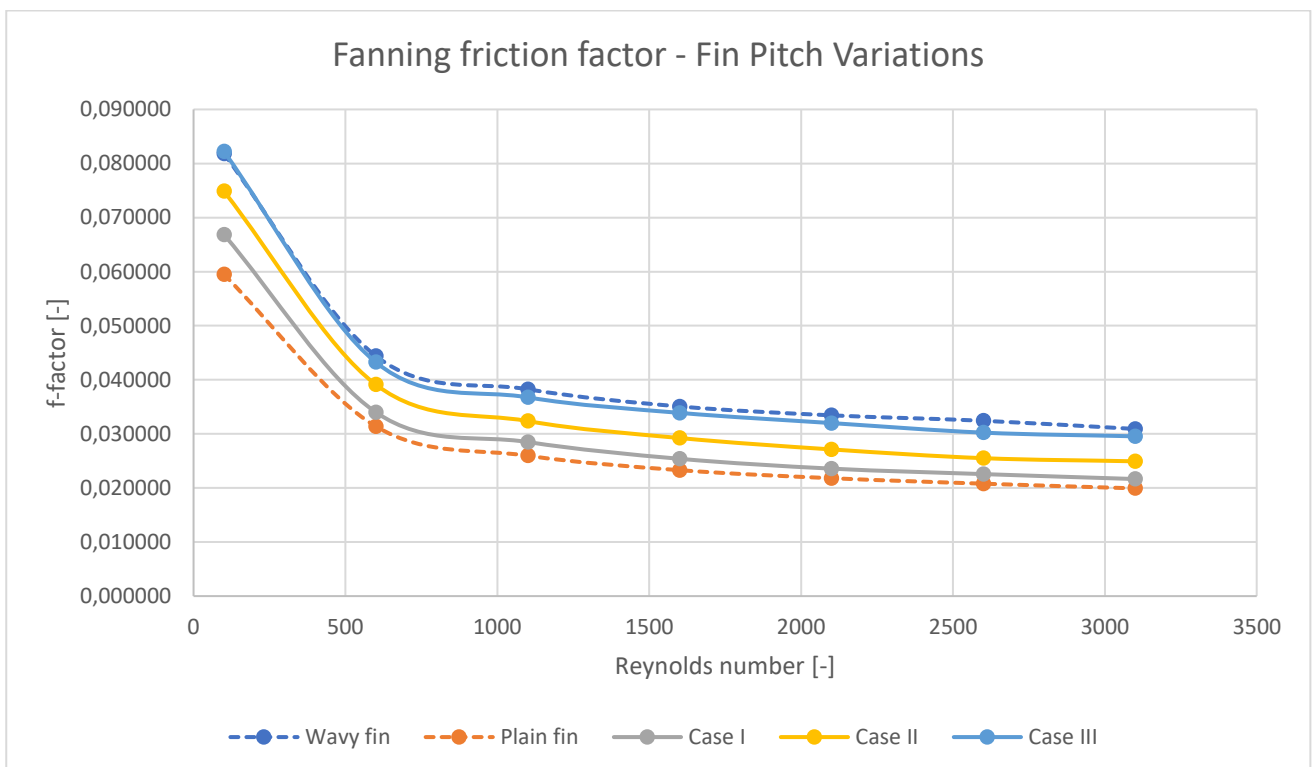**Figure 5.11: Fin pitch variations - Colburn j-factor**

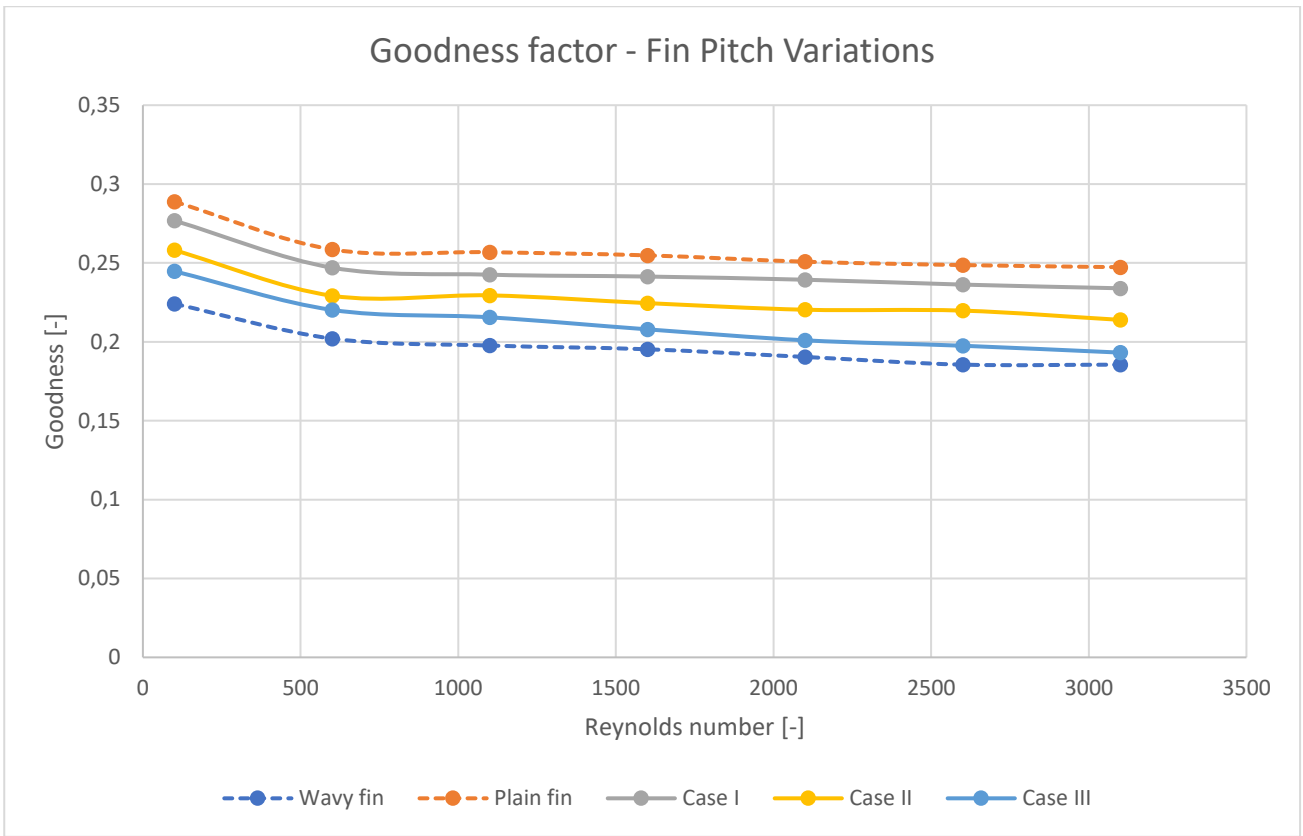**Figure 5.12: Fin pitch variations - Friction factor**

Figure 5.13: Fin pitch variations - Goodness factor
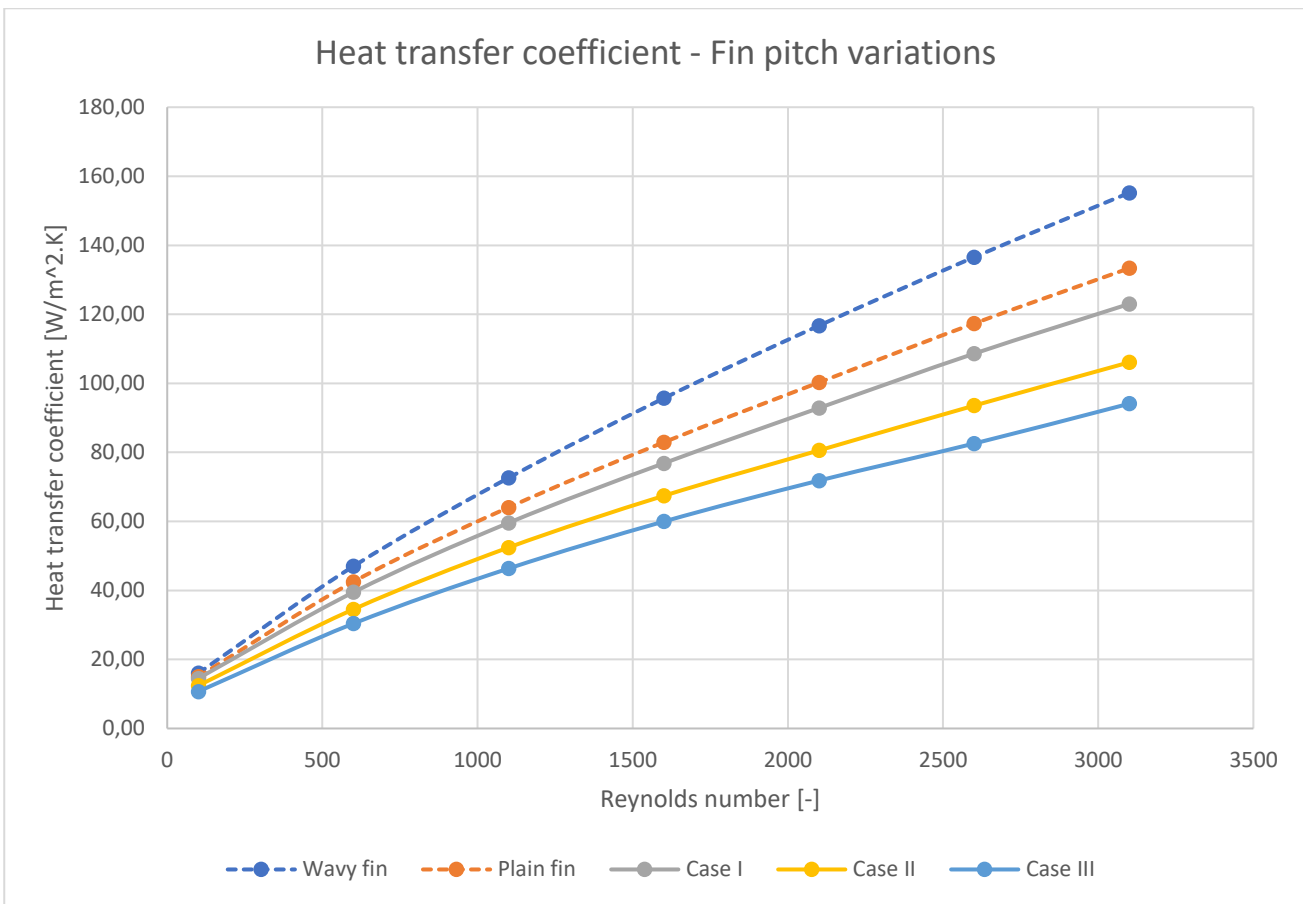

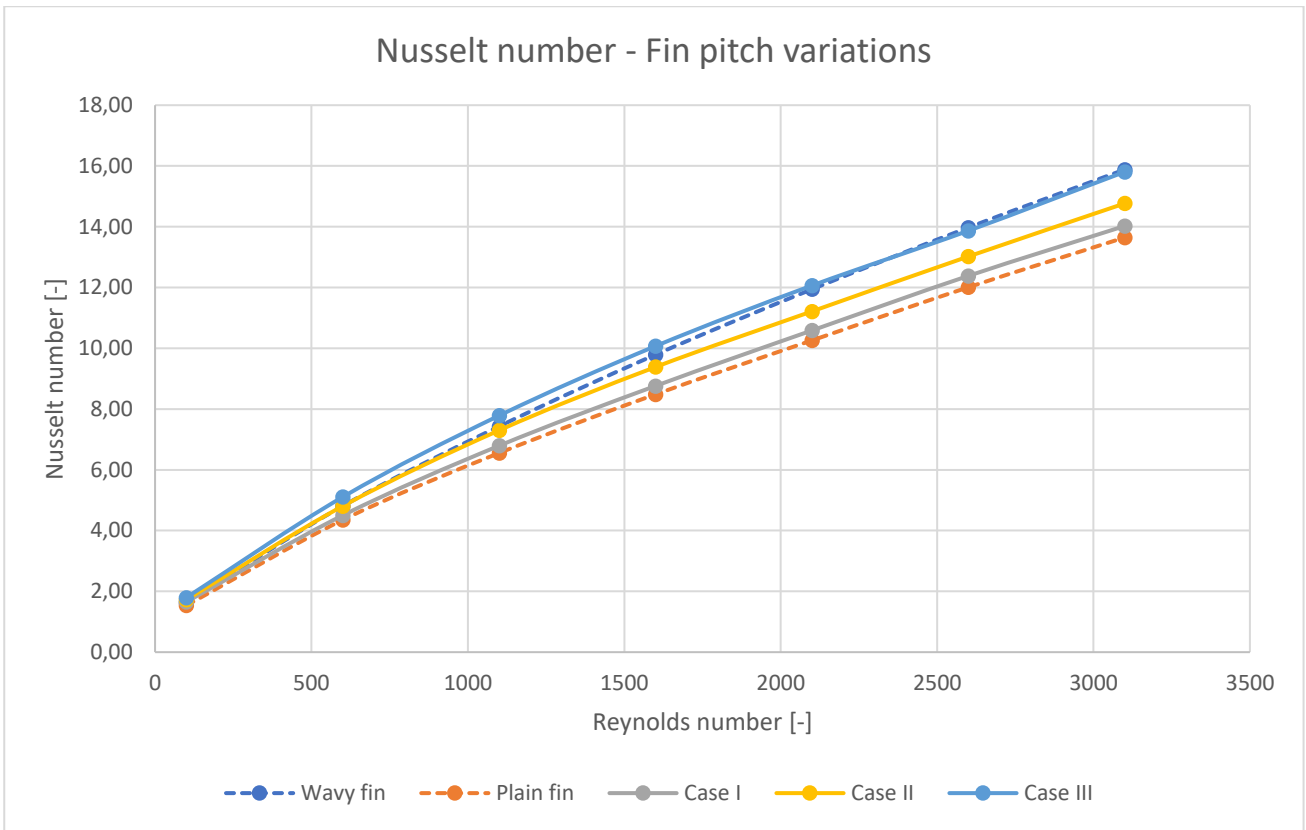**Figure 5.14: Fin pitch modifications - heat transfer coefficient**

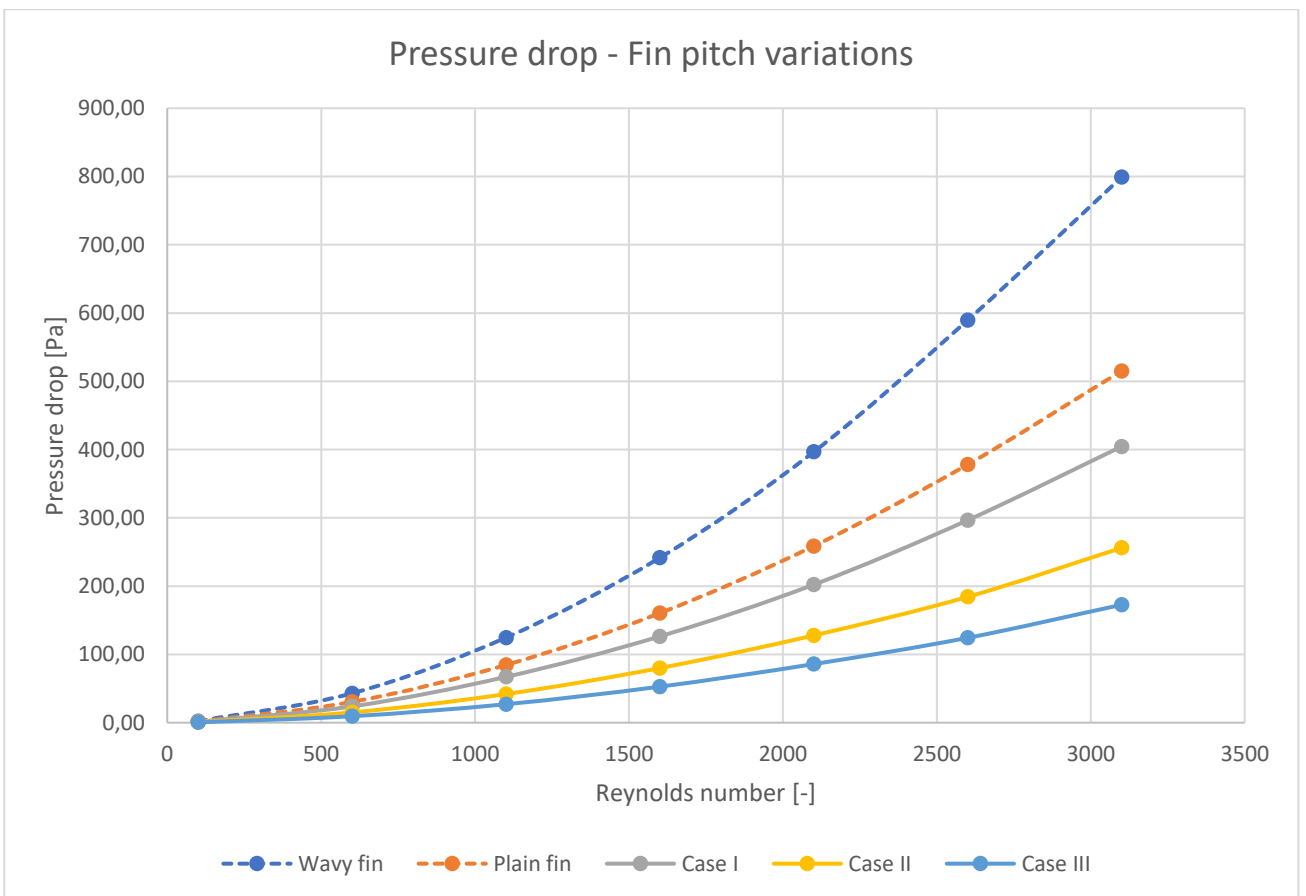**Figure 5.15: Fin pitch modifications - Nusselt number**

Figure 5.16: Fin pitch modifications - pressure drop

From the fin pitch variations, it is clear that an increase in the fin pitch caused an increase in the dimensionless heat transfer and pressure drop numbers as seen in Figures 5.11 to 5.13, but a decrease in the heat transfer coefficient and pressure drop prediction values in Figures 5.14 and 5.16 due to the substantial change in the hydraulic diameters. Case III was the most accurate at predicting the turbulent flow and Case II the laminar flow in terms of the dimensionless heat transfer numbers. The rate of increase for the heat transfer performance was not the same between the plain and wavy fins and can be clearly seen in Figure 5.15. Case III was also found to have the best prediction accuracy in terms of the friction factor.

From Figure 5.13 it can be noted that the Goodness factor of the wavy fin RS model was found to be substantially worse than the plain fin RS model. This was due to the large increase in pressure drop penalty and thus had a much larger impact on the Goodness factor than the increased heat transfer performance the wavy fins added. It can be seen that an increased fin pitch also decreased the Goodness factor and Case III was closest to the wavy fin RS model results.

Decreasing the fin pitch would increase the heat transfer coefficient and pressure drop values as needed to correlate with the wavy fin results, but would decrease the heat transfer capability and friction factor due to a more streamlined air flow, as Bhuiyan, Amin and Islam (2013) found. When using this approach, it is not possible to yield a prediction accuracy of an acceptable level for both the dimensionless heat transfer and friction factor-, as well as the heat transfer coefficient and pressure drop prediction values. The fin pitch is therefore not the best solution to geometrically modifying a plain fin RS model.

5.4.3. Longitudinal tube pitch variations tabulated results

Tables 5.7 to 5.9 illustrate the results for cases I, II and III of the longitudinal tube pitch-modified plain fin RS model simulations. Table 5.10 illustrates the pressure drop absolute deviations with regards to the wavy RS model.

Table 5.7: Longitudinal tube pitch – Case I

Reynolds number [-]	Air velocity	Simulation data		Dimensionless numbers		Goodness factor	Nusselt	Absolute deviation [%]	
		h [W/m^2.K]	ΔP [Pa]	j [-]	f [-]	[-]	[-]	j [-]	j [-]
100	0,33808	15,10	1,60	0,017297	0,065434	0,264347	1,55	5,63%	20,00%
600	2,02847	44,02	30,57	0,008404	0,034728	0,242005	4,50	6,34%	21,80%
1100	3,71886	66,48	84,21	0,006923	0,028462	0,243242	6,80	8,44%	25,60%
1600	5,40925	85,74	163,24	0,006139	0,026078	0,235394	8,77	10,38%	25,65%
2100	7,09964	103,41	260,16	0,005641	0,024126	0,233808	10,58	11,40%	27,84%
2600	8,79003	120,48	381,65	0,005308	0,023089	0,229901	12,33	11,77%	28,79%
3100	10,48042	136,80	527,40	0,005055	0,022444	0,22523	14,00	11,86%	27,39%
							Average	9,40%	25,29%

Table 5.8: Longitudinal tube pitch – Case II

Reynolds number [-]	Air velocity	Simulation data		Dimensionless numbers		Goodness factor [-]	Nusselt [-]	Absolute deviation [%]	
		h [W/m^2.K]	ΔP [Pa]	j [-]	f [-]			j [-]	j [-]
100	0,33808	16,22	1,60	0,018580	0,076981	0,241361	1,66	1,37%	5,88%
600	2,02847	46,47	30,53	0,008872	0,040803	0,217437	4,76	1,13%	8,12%
1100	3,71886	70,72	86,32	0,007365	0,034323	0,214566	7,24	2,60%	10,27%
1600	5,40925	90,87	166,11	0,006506	0,031219	0,208392	9,30	5,02%	10,99%
2100	7,09964	109,86	269,50	0,005993	0,029402	0,203815	11,24	5,87%	12,05%
2600	8,79003	127,98	392,67	0,005639	0,027948	0,201755	13,10	6,28%	13,80%
3100	10,48042	145,38	536,81	0,005372	0,026876	0,199886	14,88	6,33%	13,05%
							Average	4,09%	10,60%

Table 5.9: Longitudinal tube pitch – Case III

Reynolds number [-]	Air velocity	Simulation data		Dimensionless numbers		Goodness factor [-]	Nusselt [-]	Absolute deviation [%]	
		h [W/m^2.K]	ΔP [Pa]	j [-]	f [-]			j [-]	j [-]
100	0,33808	17,49	1,70	0,020035	0,099319	0,201724	1,79	9,31%	21,43%
600	2,02847	50,21	32,90	0,009586	0,053392	0,17954	5,14	6,83%	20,23%
1100	3,71886	76,47	94,28	0,007963	0,045522	0,174936	7,83	5,32%	19,00%
1600	5,40925	99,79	182,93	0,007144	0,041747	0,171135	10,21	4,31%	19,03%
2100	7,09964	119,62	296,88	0,006525	0,039330	0,165905	12,24	2,49%	17,64%
2600	8,79003	138,26	441,08	0,006091	0,038120	0,159797	14,15	1,25%	17,57%
3100	10,48042	156,79	605,97	0,005794	0,036839	0,15727	16,05	1,02%	19,18%
							Average	4,36%	19,15%

Due to the length of the fins being shortened as a result of a decreasing longitudinal tube pitch, the average absolute deviations of the pressure drop and friction factor prediction values were not identical. Therefore, Table 5.10 illustrates the average absolute deviations of the pressure drop for Cases I to III of the longitudinal tube pitch variations.

From Table 5.10 it is therefore evident that the pressure drop prediction values were not as accurate as the friction factor prediction values with the highest accuracy being achieved by Case III with an average absolute deviation of 24.17%.

Table 5.10: Longitudinal tube pitch variation average absolute pressure drop deviations

Reynolds number [-]	Absolute deviation [%]		
	Case I	*Case II*	*Case III*
	ΔP [Pa]	ΔP [Pa]	ΔP [Pa]
100	27,27%	27,27%	22,73%
600	28,91%	29,00%	23,49%
1100	32,36%	30,67%	24,27%
1600	32,41%	31,22%	24,25%
2100	34,40%	32,04%	25,14%
2600	35,26%	33,39%	25,18%
3100	33,99%	32,81%	24,16%
Average	32,09%	30,92%	24,17%

From Tables 5.7 to 5.9 it is evident that by decreasing the longitudinal tube pitch a better heat transfer performance was seen as well as better friction factor predictions. Case II yielded the best prediction accuracy of the heat transfer and friction factor with an average absolute deviation of 4.09% and 10.60%, respectively. Case III predicted the heat transfer performance with slightly less accuracy with an average absolute deviation of 4.36% (also within an acceptable accurate range) although the friction factor was inaccurately predicted with an average absolute deviation of 19.15%.

The heat transfer performance predictions were thus acceptably accurate while the friction factor and pressure drop predictions were not accurate on an acceptable level. Hence, a variation in the longitudinal tube pitch of a plain fin RS model is not a viable option to geometrically modifying a plain fin RS model.

The next section illustrates the graph results followed by a short discussion of the results.

5.4.4. Longitudinal tube pitch variations graph results and discussion

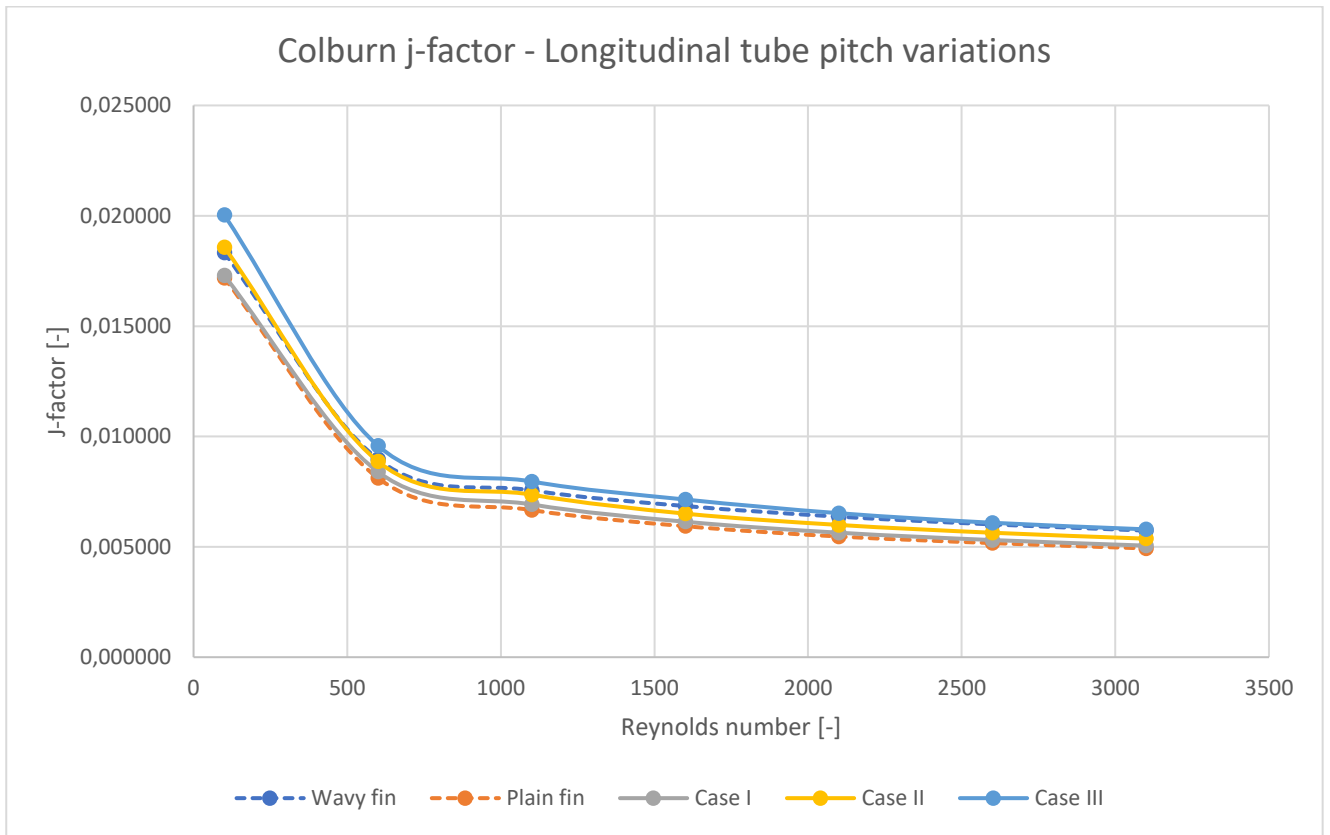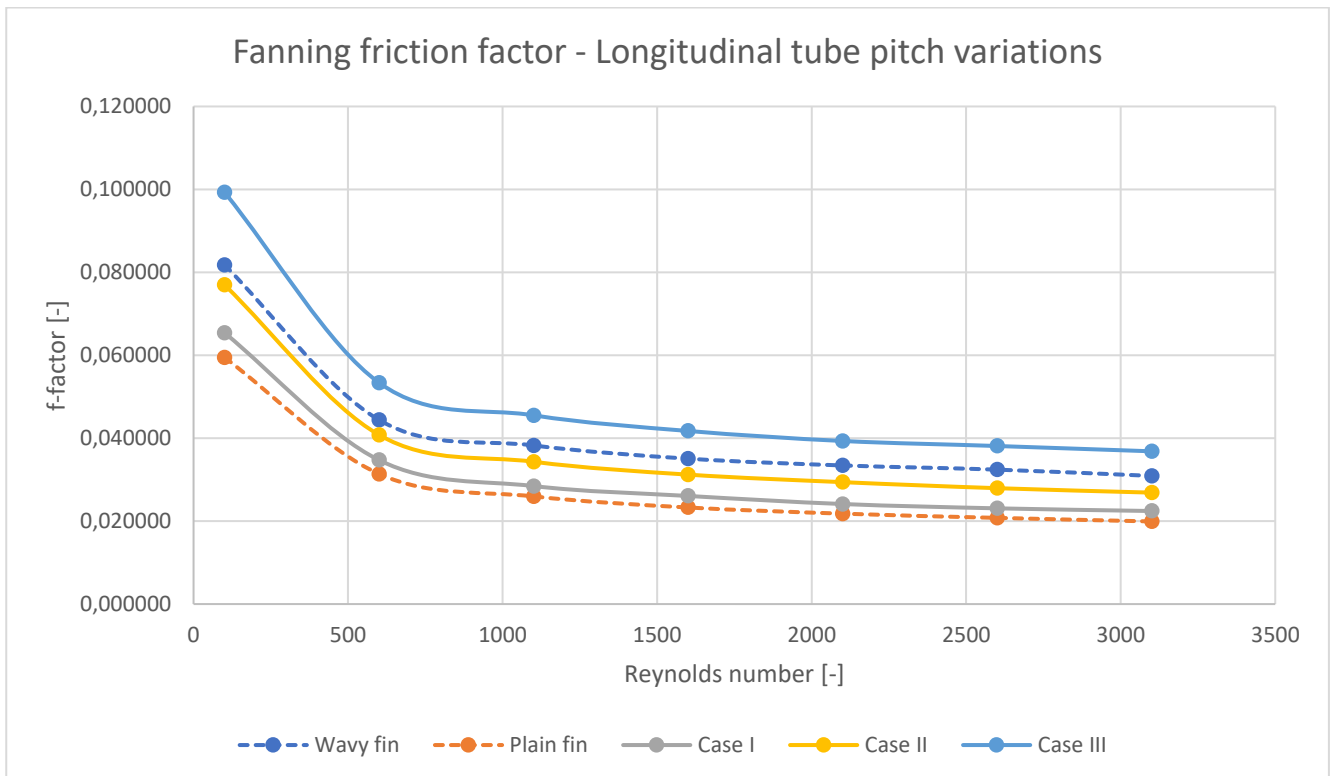**Figure 5.17: Longitudinal pitch variations - Colburn j-factor**

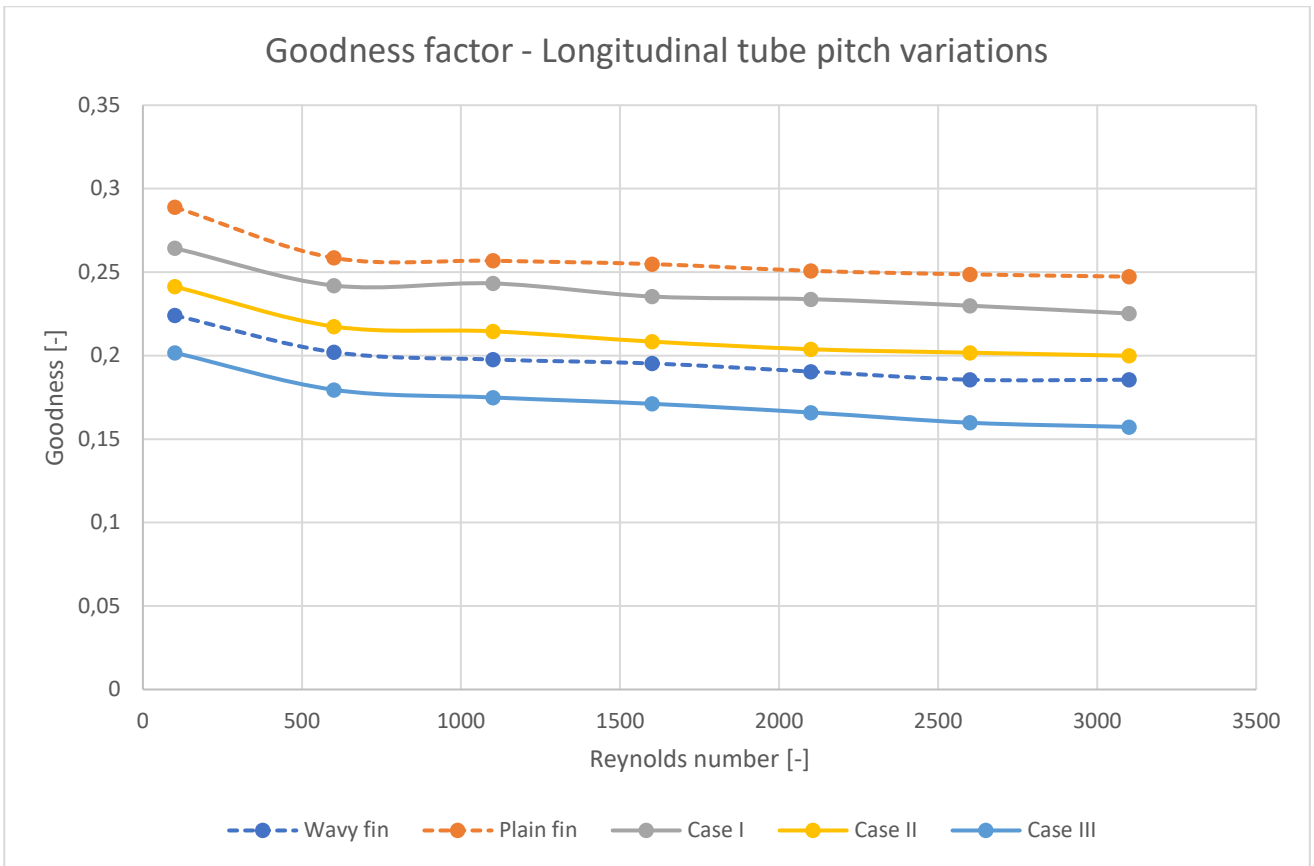**Figure 5.18: Longitudinal pitch variations - Friction factor**

Figure 5.19: Longitudinal pitch variations - Goodness factor
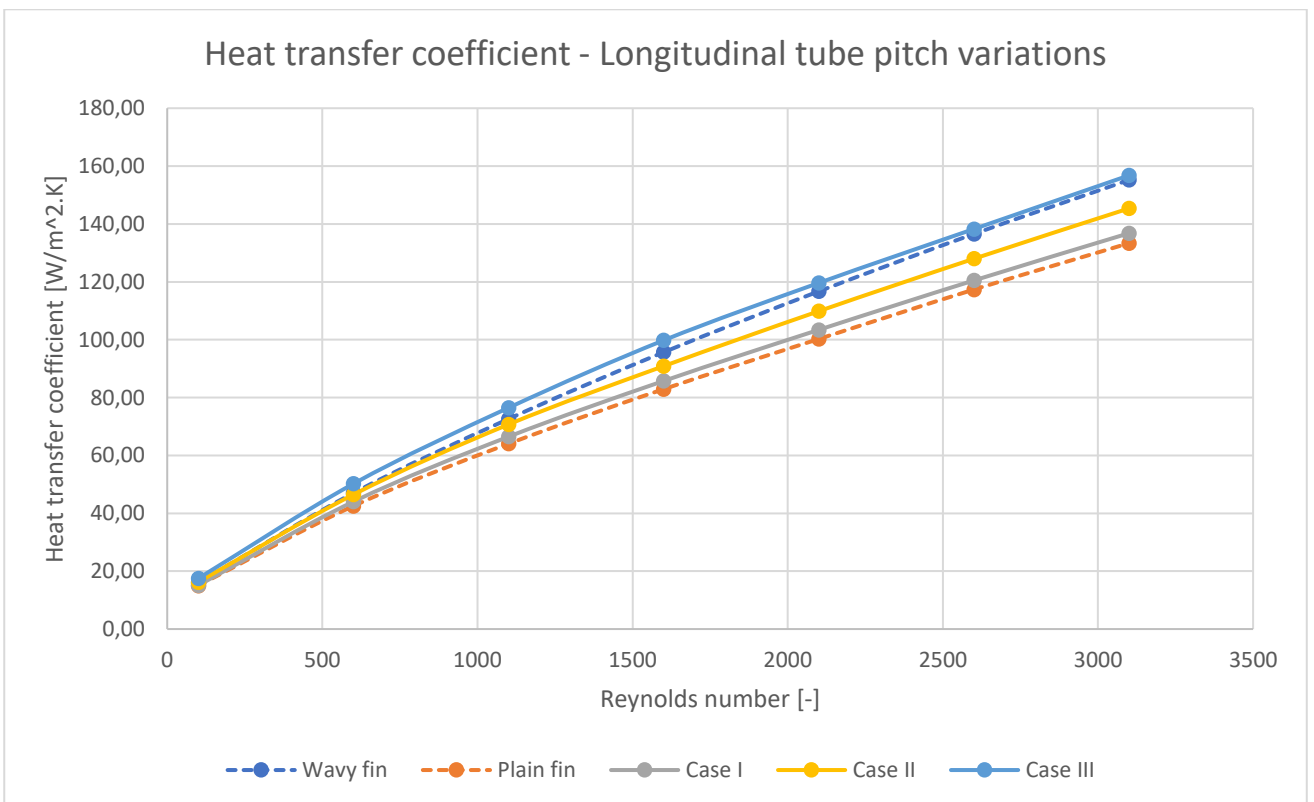

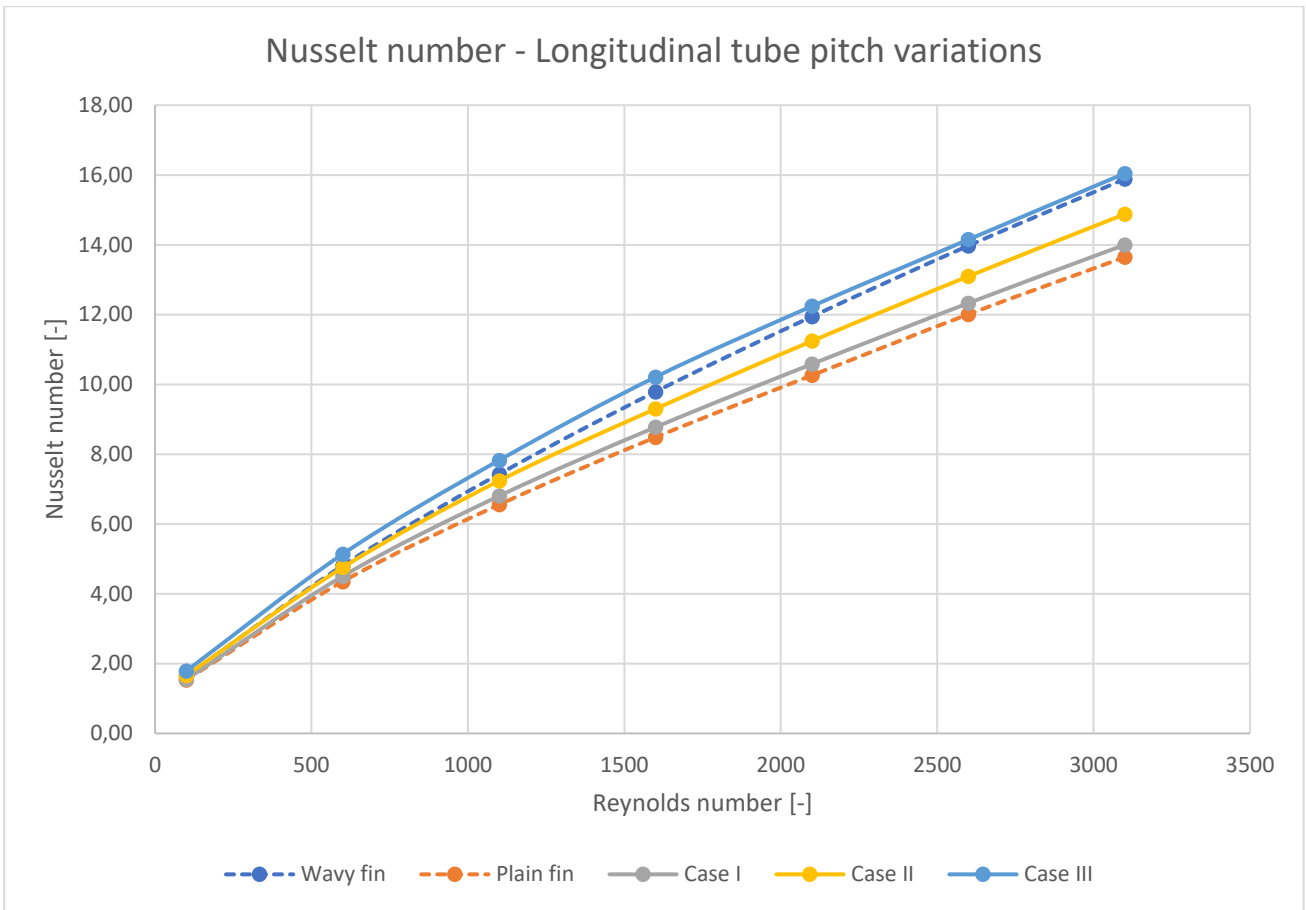**Figure 5.20: Longitudinal tube pitch variations - heat transfer coefficient**

78

Figure 5.21: Longitudinal tube pitch variations - Nusselt number
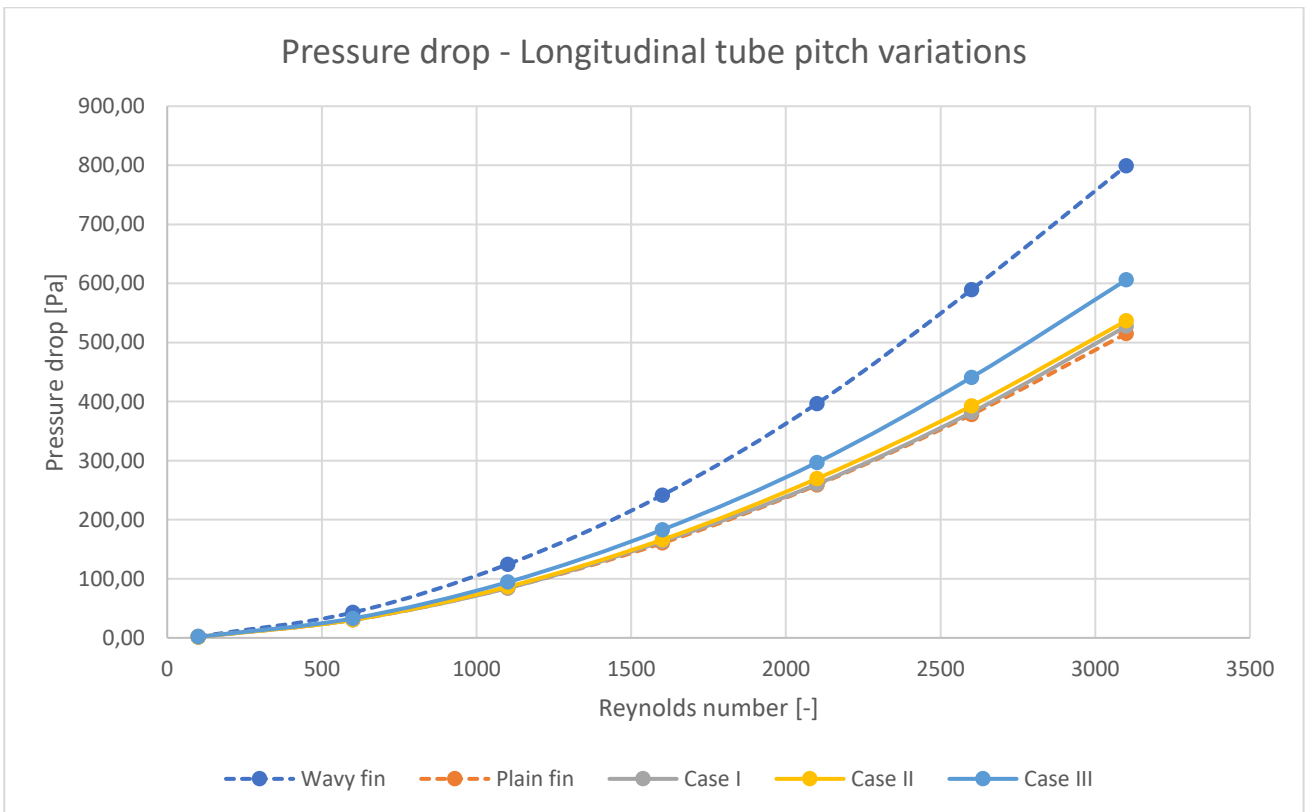

Figure 5.22: Longitudinal tube pitch variations - pressure drop

The longitudinal and transverse tube pitch variations showed similarities for rate of increase between the heat transfer coefficients and Nusselt numbers. For the longitudinal tube pitch variations, a similar result was seen between Case II and Case III for the heat transfer coefficient (Figure 5.20) and dimensionless heat transfer numbers (Figures 5.17 and 5.21) as with the fin pitch variations' heat transfer results. Case III was accurate with the turbulent flow and Case II proved accurate with the laminar flow range.

The pressure drop for the longitudinal tube pitch variations did not increase by a large enough amount to be acceptably accurate for wavy fin model predictions. In terms of the j-factor and f-factor, the wavy fin model predictions were found to be between the results of Case II and Case III as seen in Figures 5.17 to 5.19. Due to the pressure drop values not being sufficiently accurate, longitudinal tube pitch variations are also not the best solution to geometrically modifying a plain fin RS model as previously mentioned.

5.4.5. Transverse tube pitch variations tabulated results

Tables 5.11 to 5.13 illustrate the results for cases I, II and III of the transverse tube pitch-modified plain fin RS model simulations. Table 5.14 is the tabulated results of a test case which was done after testing the model prediction accuracy of the first three study cases.

Table 5.11: Transverse tube pitch - Case I

Reynolds number [-]	Air velocity	Simulation data		Dimensionless numbers		Goodness factor	Nusselt	Absolute deviation [%]	
		h [W/m^2.K]	ΔP [Pa]	j [-]	f [-]	[-]	[-]	j [-]	j [-]
100	0,33808	14,90	1,70	0,017068	0,063203	0,270052	1,52	6,88%	22,73%
600	2,02847	43,08	33,18	0,008225	0,034266	0,240028	4,41	8,34%	22,84%
1100	3,71886	65,21	91,40	0,006791	0,028083	0,241808	6,67	10,19%	26,59%
1600	5,40925	84,10	171,40	0,006021	0,024892	0,241889	8,61	12,09%	29,03%
2100	7,09964	101,72	274,65	0,005549	0,023154	0,239639	10,41	12,84%	30,74%
2600	8,79003	118,70	402,40	0,005230	0,022131	0,236307	12,15	13,07%	31,74%
3100	10,48042	134,90	557,00	0,004985	0,021549	0,231328	13,80	13,09%	30,29%
							Average	10,93%	27,71%

Table 5.12: Transverse tube pitch - Case II

Reynolds number [-]	Air velocity	Simulation data		Dimensionless numbers		Goodness factor	Nusselt	Absolute deviation [%]	
		h [W/m^2.K]	ΔP [Pa]	j [-]	f [-]	[-]	[-]	j [-]	j [-]
100	0,33808	15,05	1,85	0,017240	0,068780	0,250654	1,54	5,94%	15,91%
600	2,02847	44,00	36,00	0,008400	0,037178	0,22595	4,50	6,38%	16,28%
1100	3,71886	67,00	100,00	0,006977	0,030726	0,22708	6,86	7,73%	19,68%
1600	5,40925	87,00	190,00	0,006229	0,027593	0,225734	8,90	9,06%	21,33%
2100	7,09964	104,50	301,00	0,005700	0,025376	0,224636	10,69	10,46%	24,10%
2600	8,79003	122,50	445,00	0,005397	0,024474	0,220526	12,54	10,29%	24,52%
3100	10,48042	138,70	615,00	0,005125	0,023793	0,215414	14,19	10,64%	23,03%
							Average	8,64%	20,69%

Table 5.13: Transverse tube pitch - Case III

Reynolds number [-]	Air velocity	Simulation data		Dimensionless numbers		Goodness factor	Nusselt	Absolute deviation [%]	
		h [W/m^2.K]	ΔP [Pa]	j [-]	f [-]	[-]	[-]	j [-]	j [-]
100	0,33808	15,16	2,00	0,017366	0,074357	0,23355	1,55	5,25%	9,09%
600	2,02847	45,47	40,58	0,008681	0,041908	0,207145	4,65	3,26%	5,63%
1100	3,71886	69,48	114,80	0,007235	0,035273	0,205126	7,11	4,31%	7,79%
1600	5,40925	90,11	218,00	0,006451	0,031660	0,203773	9,22	5,81%	9,73%
2100	7,09964	109,30	353,00	0,005962	0,029759	0,200344	11,19	6,35%	10,99%
2600	8,79003	128,20	515,50	0,005648	0,028351	0,199225	13,12	6,11%	12,56%
3100	10,48042	145,20	705,00	0,005365	0,027274	0,196721	14,86	6,45%	11,76%
							Average	5,36%	9,65%

It can be seen from the tabulated data in Tables 5.11 to 5.13 that variations in the transverse tube pitch delivered promising results with an acceptable accuracy for the model heat transfer prediction values with regards to the wavy fin RS model. Case III had the highest model prediction accuracy with an average absolute deviation of 5.36%. The pressure drop prediction values is seen to yield an accuracy lower than the acceptable level with an average absolute deviation of 9.65% in Case III.

In order to find a possibly more accurate prediction set in terms of the heat transfer and pressure drop values, a test case was simulated with a transverse tube pitch of $20.5mm$. The value was selected to adhere to the simulation model restrictions, still rendering the periodic planes as valid.

The results are tabulated using Table 5.14.

Reynolds number [-]	Air velocity	Simulation data		Dimensionless numbers		Goodness factor	Nusselt	Absolute deviation [%]	
		h [W/m^2.K]	ΔP [Pa]	j [-]	f [-]	[-]	[-]	j [-]	j [-]
100	0,33808	15,20	2,10	0,017412	0,078074	0,223015	1,56	5,00%	4,55%
600	2,02847	47,00	44,00	0,008973	0,045440	0,197473	4,81	0,00%	2,33%
1100	3,71886	71,00	122,00	0,007394	0,037486	0,197243	7,27	2,22%	2,01%
1600	5,40925	92,10	231,00	0,006594	0,033548	0,196552	9,43	3,73%	4,35%
2100	7,09964	112,50	378,00	0,006137	0,031867	0,192571	11,51	3,61%	4,68%
2600	8,79003	132,00	554,00	0,005816	0,030469	0,190875	13,51	3,33%	6,03%
3100	10,48042	148,00	742,00	0,005469	0,028706	0,190515	15,15	4,65%	7,13%
							Average	3,22%	4,44%

Table 5.14 illustrates the test case results. It can be seen that the model prediction accuracy of the test case was higher than Case III from the transverse tube pitch variations group for both the heat transfer and pressure drop predictions with average absolute values of 3.22% and 4.44%, respectively. The next section illustrates the graph results followed by a short discussion of the results.

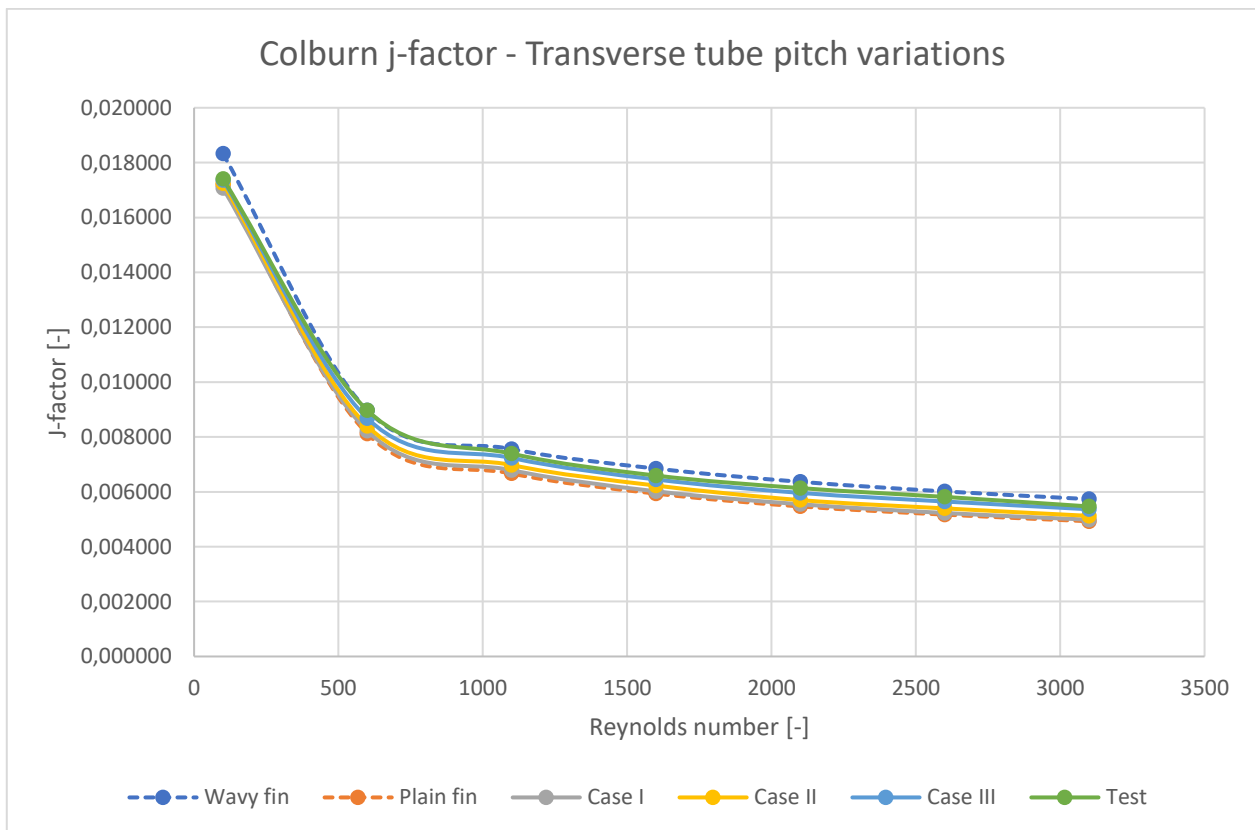### 5.4.6. Transverse tube pitch variations graph results and discussion

Figure 5.23: Transverse pitch variations - Colburn j-factor
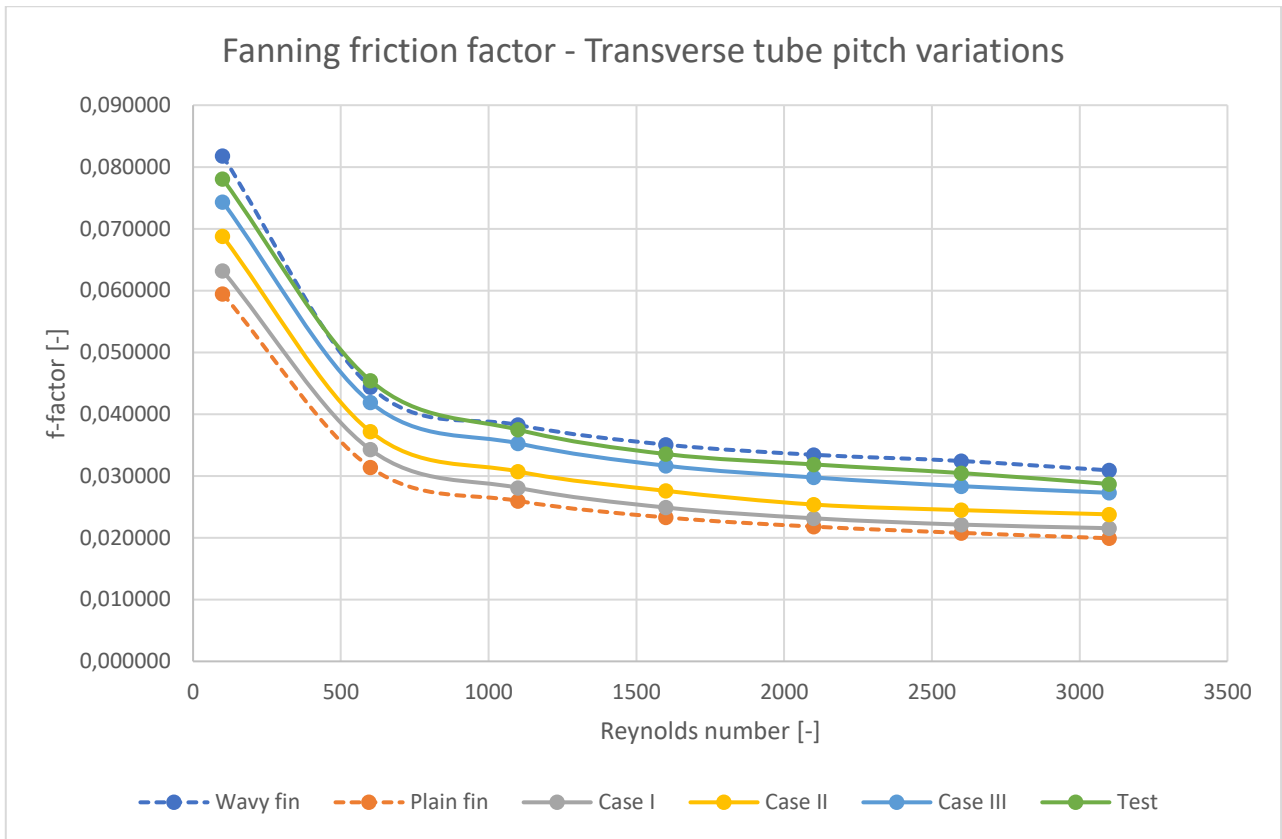
Figure 5.24: Transverse pitch variations - Friction factor
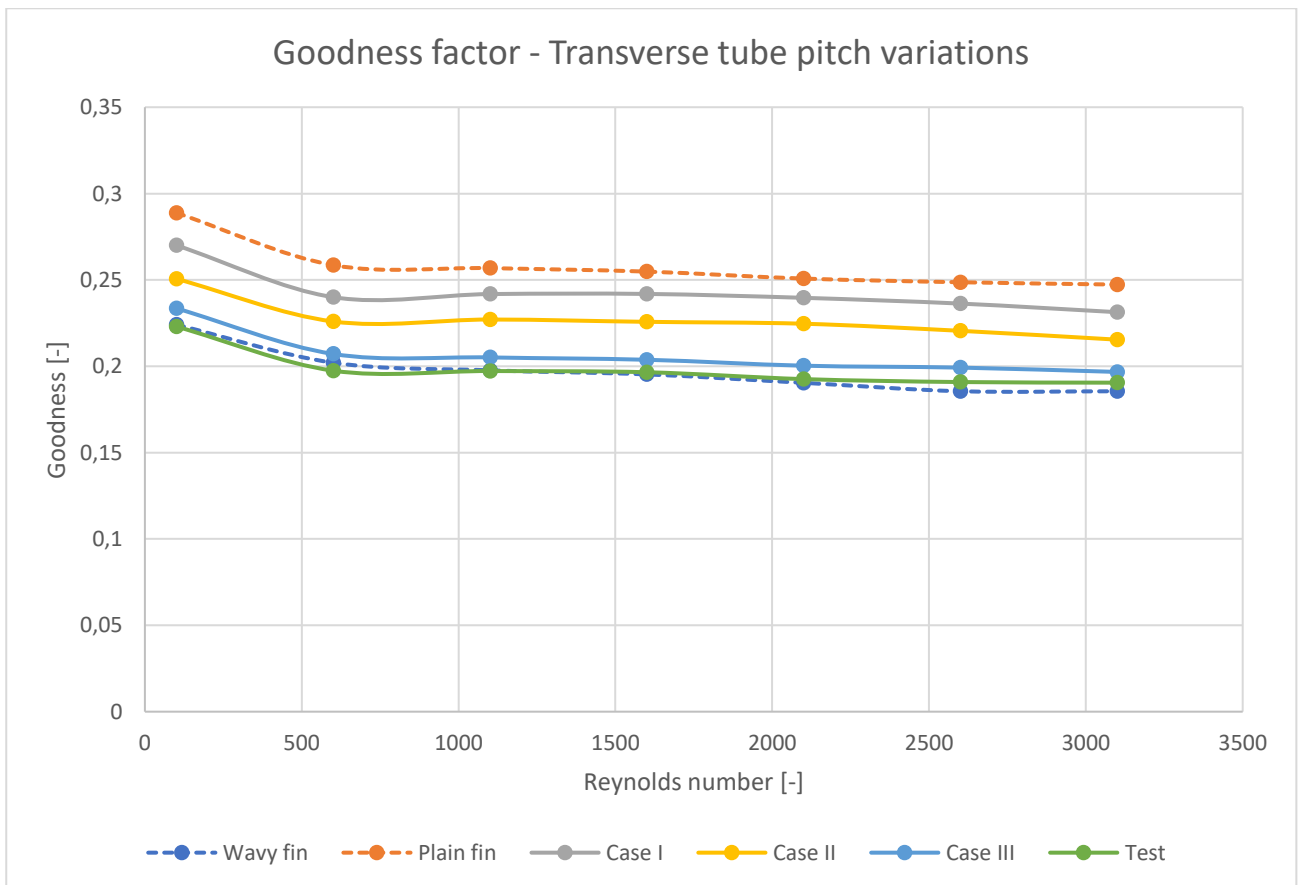
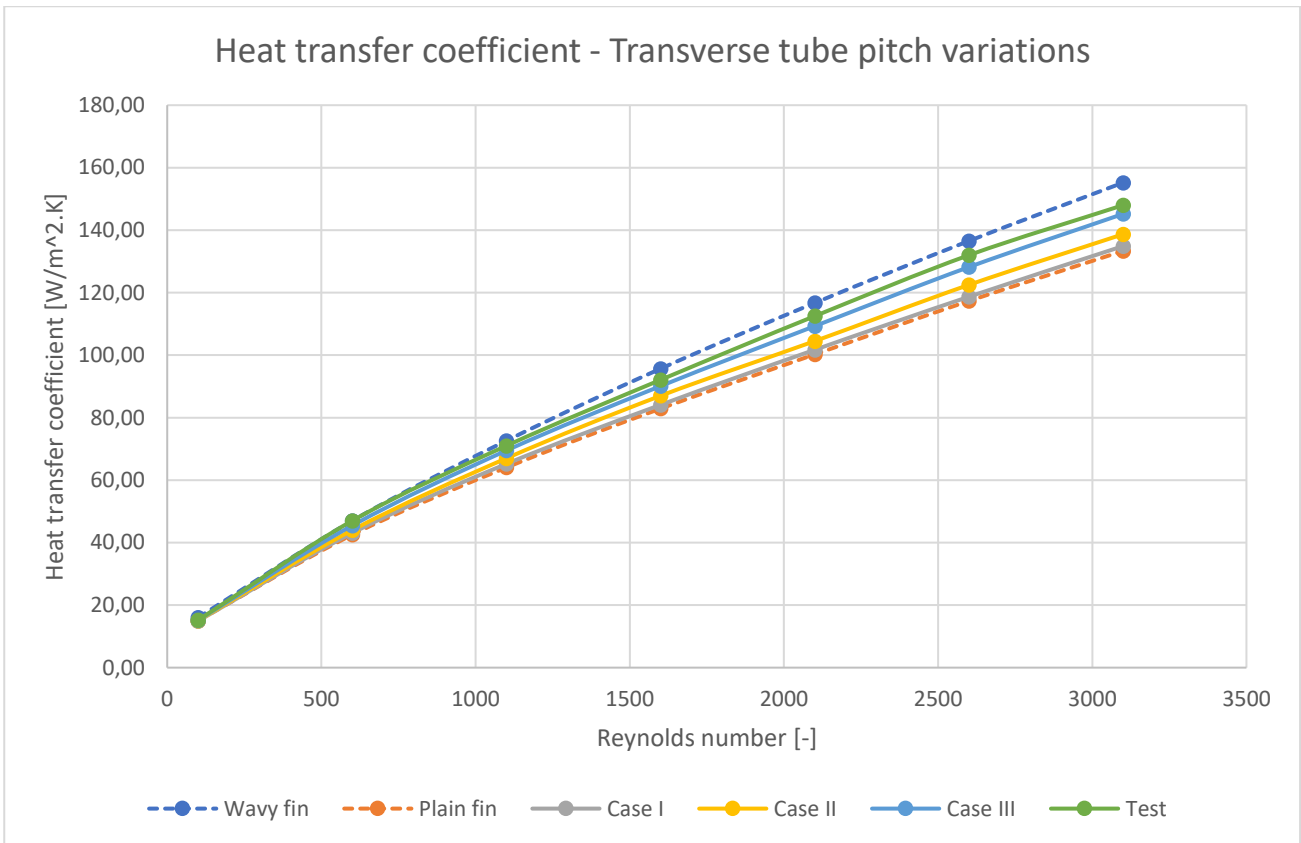

Figure 5.25: Transverse pitch variations - Goodness factor

83

Figure 5.26: Transverse tube pitch variations - heat transfer coefficient
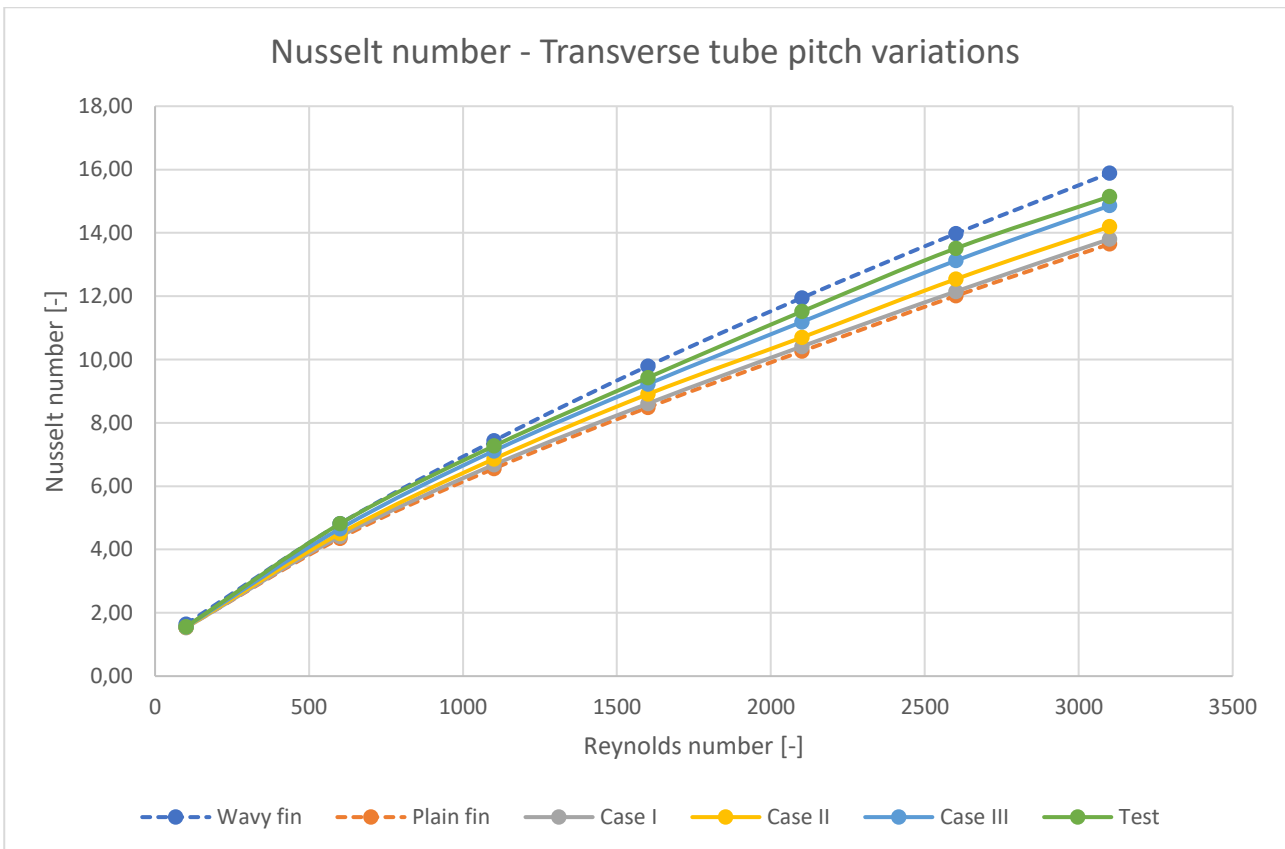

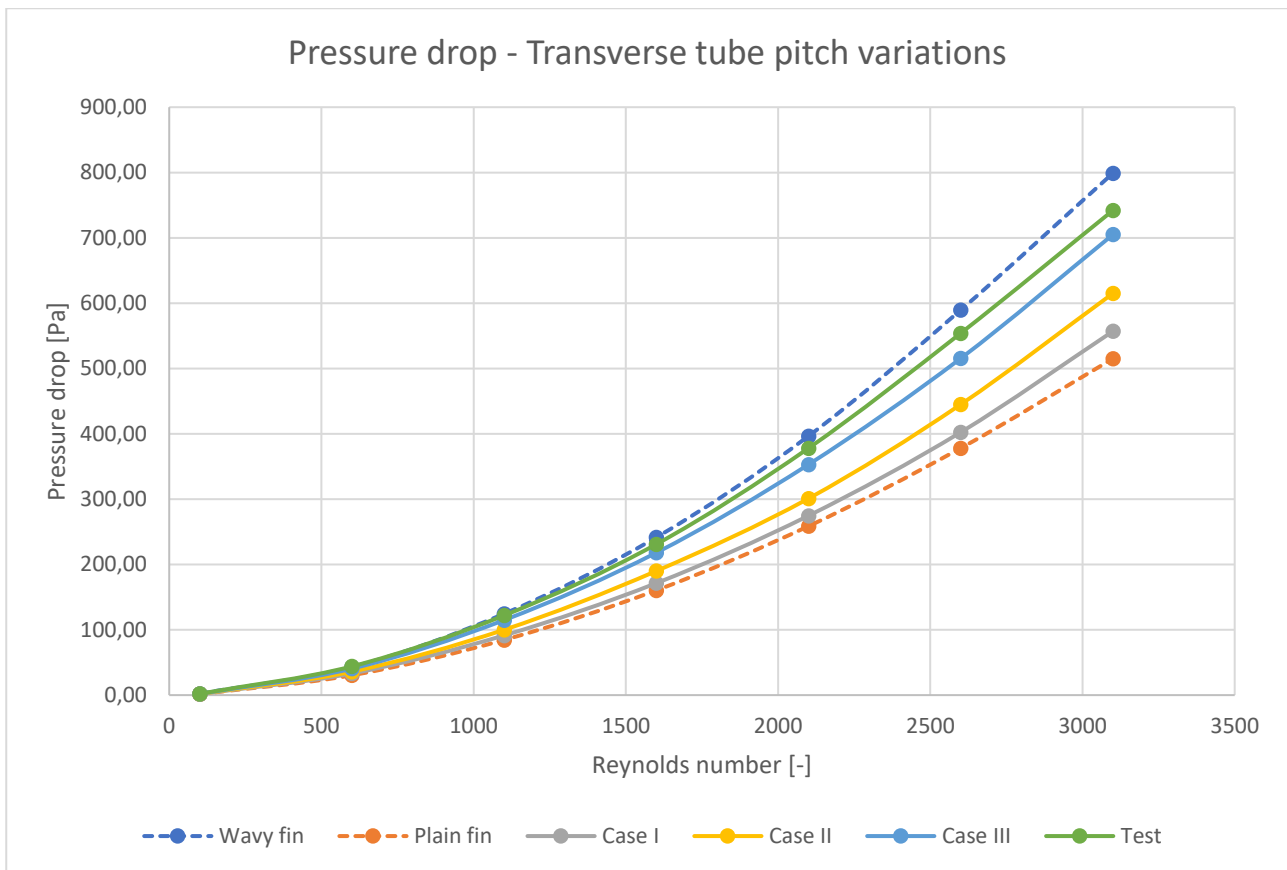**Figure 5.27: Transverse tube pitch variations - Nusselt number**

Figure 5.28: Transverse tube pitch variations - pressure drop

When referring to the transverse tube pitch modifications made, Figures 5.23 to 5.28 illustrate promising results in prediction accuracy with regards to the wavy fin RS model results. After Cases I-III were simulated and the results tabulated, it was found that a variation in the transverse tube pitch showed the best increase in both the heat transfer performance and the pressure drop (and friction factor), but was not enough. It was decided to simulate a test study Case by decreasing the transverse tube pitch to $20.5mm$ from $21.5mm$ (Case III) as this value still allows air to flow over the tube surface and prevent the periodic interface from being inaccurate (as previously mentioned). The average prediction accuracy for the entire flow range (for the test Case study) was found for the heat transfer coefficient (and Nusselt number) to be predicted with an error deviation of 3.22% and pressure drop of 4.44%; and was therefore found to be acceptably accurate. Hence, this was achieved by decreasing the transverse tube pitch by 19.29% as a constant value over the total range of air flow.

In terms of the j-factor and f-factor both the prediction accuracies are acceptable. It can be seen from the graphical results that a variation in the transverse tube pitch therefore shows the most promise and can be investigated in future studies using an alternative modelling approach.

5.5. Conclusion

In conclusion to this chapter, it was found that a plain fin RS model does not satisfy the requirements to predict a wavy fin RS model's results on an acceptable level of accuracy. Therefore, geometrical modifications have to be made to the plain fin model in order to achieve more accurate results with reference to a wavy fin model.

It was also found that decreasing the fin pitch and longitudinal tube pitch was not as effective as decreasing the transverse fin pitch. The latter showed promising results within the constraints of the RS model type and could be implemented as an easier design alternative to a wavy fin model. More research has to be done to confirm this finding by comparison using a wavy fin model incorporating a variation of waviness heights and a different set of geometrical parameters before a final confirmation can be made.

Chapter 6 : Conclusion

The focus of this study was to investigate whether a TTI FCHX model could be geometrically simplified into a RS model; whilst still yielding an acceptable level of accuracy of the air-side heat transfer and pressure drop with regards to a trusted reference's TTI FCHX's experimental data.

Thereafter, whilst employing the outcome of a geometrically simplified model, the study further determined the validity of simulating a geometrically modified plain fin model as a representation of a wavy fin model. This was done after concluding that a plain fin RS model would not yield results of acceptable accuracy with reference to an otherwise geometrically identical wavy fin RS model. The air-side heat transfer and pressure drop data of the wavy fin RS model was used as reference to determine the validity of geometrically modifying a plain fin model.

Kays and London, *Compact heat exchangers, 3rd ed. (1998)* was implemented as the experimental data reference for heat transfer and pressure drop data. This was done as a measure of validation, as the resource is an internationally recognised book and the flagship of various compact HX test data as described in section 1.1.2. This reference supported the purpose of this study by providing accurate experimental test data.

Concluding Chapter 4, it was seen that both the model predictions of the heat transfer coefficient and pressure drop, and in return the Colburn- and Fanning friction factors were acceptably accurate for an air flow of $Re > 800$. The TTI model showed a minor improvement of the heat transfer and pressure drop predictions by only 1.18% and 1.83%, respectively. When compared to the much faster simulation convergence of the RS model, the TTI model's extra time and computational expense was not defensible. Hence, the RS model proved to be an excellent alternative to the TTI FCHX model to save computational expense and, therefore, simulation time. The RS model predictions would be deemed adequate and suffice in the requirements as a representation of the TTI FCHX and was implemented for the simulations to follow in Chapter 5.

Concluding Chapter 5, it was found that a plain fin RS model did not satisfy the requirements to predict a wavy fin RS model's results on an acceptable level of accuracy, as mentioned earlier. Therefore, geometrical modifications had to be made to the plain fin model in order to achieve more accurate results with reference to a wavy fin model.

It was found that decreasing the fin pitch and longitudinal tube pitch was not as effective as decreasing the transverse fin pitch. The latter showed promising results within the constraints of the RS model type and could be implemented as an easier design alternative to a wavy fin model. The average prediction accuracy for the entire flow range (for the transverse tube pitch variation test Case study) was found for the heat transfer performance to be predicted with an error deviation of 3.22% and pressure drop (and friction factor) of 4.44%; and was therefore acceptably accurate over the entire air flow range. Hence, this was achieved by decreasing the transverse tube pitch by

19.29% as a constant value over the total range of air flow. Although the variation in transverse tube pitch proved to be acceptable for this study, more research has to be done in the future to confirm this finding using a wavy fin model incorporating a variation of waviness heights (and waviness angles) and a different set of geometrical parameters before a final conformation can be made. Whilst a RS model approach is deemed as acceptable, the simulation of a wavy fin is RS model is recommended over the geometrically modified plain fin RS model until any further concluding research is done.

As a final conclusion to the study, in the field of CFD simulations and FCHXs, computational expenses can be limited using a RS model type and yield acceptable accuracy. If reasonable accuracy is of utmost importance, it is recommended to implement a RS model type incorporating the precise fin profile.

Bibliography

Achenbach, E. (1968). Distribution of local pressure and skin friction around a circular cylinder in cross-flow up to Re = 5 × 10 6. Journal of Fluid Mechanics, 34(04), p.625.

Aslam Bhutta, M., Hayat, N., Bashir, M., Khan, A., Ahmad, K. and Khan, S. (2012). CFD applications in various heat exchangers design: A review. Applied Thermal Engineering, 32, pp.1-12.

Ay, H., Jang, J. and Yeh, J. (2002). Local heat transfer measurements of plate finned-tube heat exchangers by infrared thermography. *International Journal of Heat and Mass Transfer*, 45(20), pp.4069-4078.

Borrajo-Peláez, R., Ortega-Casanova, J. & Cejudo-López, J. (2010). A three-dimensional numerical study and comparison between the air side model and the air/water side model of a plain fin-and-tube heat exchanger. Applied Thermal Engineering. 30(13):1608-1615.

Bergles, A., Webb, R. and Junkan, G. (1979). Energy conservation via heat transfer enhancement. Energy, 4(2), pp.193-200.

Bhuiyan, A., Amin, M. and Islam, A. (2013). Three-dimensional performance analysis of plain fin tube heat exchangers in transitional regime. Applied Thermal Engineering, 50(1), pp.445-454.

Bououd, M., Hachchadi, O. and Mechaqrane, A. (2018). Plate flat finned tubes heat exchanger: Heat transfer and pressure drop modeling. *IOP Conference Series: Earth and Environmental Science*, 161, p.012001.

Capital Coil & Air. (2018). Why do HVAC Coils Copper Tube & Aluminum Fin?. http://www.capitalcoil.com/why-are-coils-copper-tube-aluminum-fin/. Date of access: 31 Oct. 2018.

CD-Adapco (2012). STAR South East Asian Conference 2012.

Chin Ngo, C. (2018). Fluids eBook: Flow between Parallel Plates. http://www.ecourses.ou.edu/cgi-bin/ebook.cgi?topic=fl&chap_sec=08.1&page=theory. Date of access: 7 Sep. 2018.

Darvish Damavandi, M., Forouzanmehr, M. and Safikhani, H. (2017). Modeling and Pareto based multi-objective optimization of wavy fin-and-elliptical tube heat exchangers using CFD and NSGA-II algorithm. Applied Thermal Engineering, 111, pp.325-339.

Engineering.com. (2018). 3 Criteria for Assessing CFD Convergence. [online] Available at: https://www.engineering.com/DesignSoftware/DesignSoftwareArticles/ArticleID/9296/3-Criteria-for-Assessing-CFD-Convergence.aspx. Date of access: 31 Oct. 2018.

Erek, A., Özerdem, B., Bilir, L. and İlken, Z. (2005). Effect of geometrical parameters on heat transfer and pressure drop characteristics of plate fin and tube heat exchangers. Applied Thermal Engineering, 25(14-15), pp.2421-2431.

Fchart. (2018). Finned circular tubes, surface 8.0-3/8T. www.fchart.com/ees/heat_transfer_library/compact_hx/hs1050.htm. Date of access: 15 Oct. 2018.

Ferguson, M. P. a. S., (2005). *semanticscholar.* https://pdfs.semanticscholar.org/51ae/90047ab44f53849196878bfec4232b291d1c.pdf Date of access: 16 May 2018.

Fjallman, J. (2013). Unsteady simulations of the turbulent flow in the exhaust system of an IC-engine for optimal energy utilization. Royal Institute of Technology, Sweden.

Fugmann, H., Laurenz, E. and Schnabel, L. (2019). Multi-Dimensional Performance Evaluation of Heat Exchanger Surface Enhancements. Energies, 12(7), p.1406.

Garimella et al. (2018). Boundary Layer Meshing for Viscous Flows in Complex Domains. https://pdfs.semanticscholar.org/65e3/bb765f374b4857edfbc18d206d74591ec86a.pdf. Date of access: 30 Aug. 2018.

Gholami, A., Wahid, M. and Mohammed, H. (2017). Thermal–hydraulic performance of fin-and-oval tube compact heat exchangers with innovative design of corrugated fin patterns. International Journal of Heat and Mass Transfer, 106, pp.573-592.

Gu, L., Min, J., Wu, X. & Yang, L. (2017). Airside heat transfer and pressure loss characteristics of bare and finned tube heat exchangers used for aero engine cooling considering variable air properties. International Journal of Heat and Mass Transfer. 108:1839-1849.

Hansen, A. (2008). CFD simulation of a fin-and-tube heat exchanger: Heat transfer, fluid flow, and turbulence model analysis using 3D open-source CFD code. Master of Science Thesis. Aalborg University Esbjerg.

Jabbour, J., Russeil, S., Mobtil, M., Bougeard, D., Lacrampe, M. and Krawczak, P. (2019). High performance finned-tube heat exchangers based on filled polymer. *Applied Thermal Engineering*, 155, pp.620-630.

Jang, J., Wu, M. and Chang, W. (1996). Numerical and experimental studies of three-dimensional plate-fin and tube heat exchangers. *International Journal of Heat and Mass Transfer*, 39(14), pp.3057-3066.

Jang, J. and Chen, L. (1997). Numerical analysis of heat transfer and fluid flow in a three-dimensional wavy-fin and tube heat exchanger. International Journal of Heat and Mass Transfer, 40(16), pp.3981-3990.

Jousef, M. (2019). What is y+ (yplus)?. https://www.simscale.com/forum/t/what-is-y-yplus/82394. Date of access: 16 Jan. 2019.

Kapoor, A. (2018). A Quick Approach to Boundary Layer meshing - For Beginners. https://www.linkedin.com/pulse/quick-approach-boundary-layer-meshing-beginners-awadh-kapoor- Date of access: 30 Aug. 2018.

Kakaç, S., Shah, R. and Aung, W. (1987). Handbook of single-phase convective heat transfer. New York: Wiley.

Kakaç, S., Liu, H. and Pramuanjaroenkij, A. (2012). Heat exchangers. Boca Raton, FL: CRC Press.

Kármán, T. (1911). ther den Mechanismus des Widerstands, den ein bewegter Korper in einer Fliissigkeit erfiihrt. Ciittinger Nachrichten, Math. Phys. Kl. :509-517.

Karmo, D., Ajib, S. and Khateeb, A. (2013). New method for designing an effective finned heat exchanger. Applied Thermal Engineering, 51(1-2), pp.539-550.

Kays, W. & London, A. (1950). Heat-Transfer and Flow-Friction Characteristics of Some Compact Heat-Exchanger Surfaces. Transactions of the ASME. 72:1075 - 1085.

Kays, W. and London, A. (1998). Compact heat exchangers. 3rd ed. Malabar, Fla: Krieger.

Khalil, E. (2012). CFD History and Applications. *CFD letters*, 4(2).

Khudheyer, A. and Mahmoud, M. (2011). Numerical analysis of fin-tube plate heat exchanger by using cfd technique. ARPN Journal of Engineering and Applied Sciences, 6(7).

Kong, Y., Yang, L., Du, X. and Yang, Y. (2016). Impacts of geometric structures on thermo-flow performances of plate fin-tube bundles. *International Journal of Thermal Sciences*, 107, pp.161-178.

Kurganov, V. (2019). Heat transfer coefficient. http://www.thermopedia.com/content/841/.

Kuron, M. (2019). 3 Criteria for Assessing CFD Convergence. Engineering.com. URL https://www.engineering.com/DesignSoftware/DesignSoftwareArticles/ArticleID/9296/3-Criteria-for-Assessing-CFD-Convergence.aspx.

Leap Australia. (2019). Tips & Tricks: Convergence and Mesh Independence. https://www.computationalfluiddynamics.com.au/convergence-and-mesh-independent-study/. Date of access: 15 Apr. 2019.

Lewis, F. (1933). The Significance of Cells as Revealed by Their Polyhedral Shapes, with Special Reference to Precartilage, and a Surmise concerning Nerve Cells and Neuroglia. Proceedings of the American Academy of Arts and Sciences, 68(8), p.251.

Lilek, Ž., Muzaferija, S., Perić, M. and Seidl, V. (1997). Computation of unsteady flows using nonmatching blocks of structured grid. *Numerical Heat Transfer, Part B: Fundamentals*, 32(4), pp.403-418.

Liu, X., Yu, J. and Yan, G. (2016). A numerical study on the air-side heat transfer of perforated finned-tube heat exchangers with large fin pitches. *International Journal of Heat and Mass Transfer*, 100, pp.199-207.

Lu, C., Huang, J., Nien, W. and Wang, C. (2011). A numerical investigation of the geometric effects on the performance of plate finned-tube heat exchanger. Energy Conversion and Management, 52(3), pp.1638-1643.

Lytron. (2019). https://www.lytron.com/product-support/resource.cfm?aid=1237. Date of access: 24 Sep. 2019.

Martynenko, O. and Polijakov, A. (n.d.). Free convection. http://www.thermopedia.com/content/786/. Date of access: 13 May 2019.

Mavriplis, D. (1995). Three-dimensional multigrid Reynolds-averaged Navier-Stokes solver for unstructured meshes. *AIAA Journal*, 33(3), pp.445-453.

Panse, S. (2005). A Numerical Investigation of Thermal-hydraulic Characteristics in Three-Dimensional Plate and Wavy Fin-tube Heat Exchangers for Laminar and Transitional Flow Regimes. Master of Science. Montana State University.

Patel, M. (2013). *Computational Fluid Dynamics (CFD) Simulation Benefits Practical Applications*. https://www.hitechcfd.com/cfd-knowledgebase/cfd-simulation-benefits-practical-applications.html. Date of access: 2 Jul. 2018.

Peric and Ferguson (2018). The advantage of polyhedral meshes. https://pdfs.semanticscholar.org/51ae/90047ab44f53849196878bfec4232b291d1c.pdf. Date of access: 3 Sep. 2018.

Prandtl, L. (1904). Verhandlung des III Internationalen Mathematiker-Kongresses. Heidelberg. :484-491.

Pretechnologies. (2019). Advantages of CFD. http://www.pretechnologies.com/services/computational-fluid-dynamics/advantage. Date of access: Feb. 2019.

Richardson, L. (1910). On the Approximate Arithmetical Solution by Finite Differences of Physical Problems Involving Differential Equations, with an Application to the Stresses in a Masonry Dam. Proceedings of the Royal Society A: Mathematical, Physical and Engineering Sciences. 83(563):335-336.

Romero-Méndez, R., Sen, M., Yang, K. and McClain, R. (2000). Effect of fin spacing on convection in a plate fin and tube heat exchanger. International Journal of Heat and Mass Transfer, 43(1), pp.39-51.

Rossetti, A., Minetto, S. and Marinetti, S. (2015). A simplified thermal CFD approach to fins and tube heat exchanger: Application to maldistributed airflow on an open display cabinet. *International Journal of Refrigeration*, 57, pp.208-215.

Sadrehaghighi, I. (2019). *Mesh Generation in CFD.*

Schlichting, H. 1955. Boundary Layer Theory, etc. Pergamon Press: London; Verlag G. Braun: Karlsruhe; Karlsruhe printed.

Shah, R. and Sekuliâc, D. (2012). Fundamentals of heat exchanger design. Hoboken, NJ: John Wiley & Sons.

Simscale.com. (2018). What is the Reynolds Number?
https://www.simscale.com/docs/content/simwiki/numerics/what-is-the-reynolds-number.html. Date of access: 8 Sep. 2018.

SODJA, J. (2019). *Turbulence models in CFD*. University of Ljubljana.

Solmaz, S. (2019). *Turbulence Models: Which Should I Select for My CFD Analysis?*
https://www.simscale.com/blog/2017/12/turbulence-cfd-analysis/ Date of access: 8 Jul. 2019.

Sosnowski, M., Krzywanski, J., Grabowska, K. & Gnatowska, R. (2018). Polyhedral meshing in numerical analysis of conjugate heat transfer. EPJ Web of Conferences. 180:02096.

Southampton.ac.uk. (2018). What is the Prism Layer Meshing Model?
http://www.southampton.ac.uk/~zxie/SESS6021/CCMP/online1/072-workingWithPrismMesh-02.html Date of access: 30 Aug. 2018.

Stone, K. (1996). *Review of Literature on Heat Transfer Enhancement in Compact Heat Exchangers*. Investigation of Wavy Fins for Heat Transfer. Urbana,IL 61801: The Air Conditioning and Refrigeration Center.

Sun, L. and Zhang, C. (2014). Evaluation of elliptical finned-tube heat exchanger performance using CFD and response surface methodology. International Journal of Thermal Sciences, 75, pp.45-53.

Symscape. (2019). Polyhedral, Tetrahedral, and Hexahedral Mesh Comparison.
https://www.symscape.com/polyhedral-tetrahedral-hexahedral-mesh-comparison Date of access: 16 Apr. 2019.

Tahseen, T., Ishak, M. and Rahman, M. (2015). An overview on thermal and fluid flow characteristics in a plain plate finned and un-finned tube banks heat exchanger. *Renewable and Sustainable Energy Reviews*, 43, pp.363-380.

Thulukkanam, K. (2013). Heat exchanger design handbook, second edition. 2nd ed. Boca Raton: Taylor & Francis Group.

Tobe, F. (2019). CFD software saves 75% in prototype build costs. Design World. URL https://www.designworldonline.com/cfd-software-saves-75-prototype-build-costs/. Date of access: 15 October 2018.

Tutar, M. and Akkoca, A. (2004). Numerical analysis of fluid flow and heat transfer characteristics in three-dimensional plate fin-and-tube heat exchangers. *Numerical Heat Transfer, Part A: Applications*, 46(3), pp.301-321.

Ünal, U., Atlar, M. and Gören, Ö. (2010). Effect of turbulence modelling on the computation of the near-wake flow of a circular cylinder. *Ocean Engineering*, 37(4), pp.387-399.

Volume Meshers Overview. (2016). CD-Adapco.

von Kármán, T. (1937). Turbulence. The Journal of the Royal Aeronautical Society. 41(324):1109-1143.

Wall treatment reference. (2018). CD-Adapco.

White, F. (1991). Viscous Fluid Flow. [s.l.]: McGraw-Hill Education.

Y+ Calculator - Compute Wall Spacing for CFD. (2019). Pointwise.com. URL http://www.pointwise.com/yplus/.

Yaïci, W., Ghorab, M. and Entchev, E. (2016). 3D CFD study of the effect of inlet air flow maldistribution on plate-fin-tube heat exchanger design and thermal–hydraulic performance. International Journal of Heat and Mass Transfer, 101, pp.527-541.

Yashar, D., Domanski, P. and Cho, H. (2011). An experimental and computational study of approach air distribution for a finned-tube heat exchanger. HVAC&R Research, 17(1), pp.76-85.

Yuan, Z. (2000). Numerical study of periodically turbulent flow and heat transfer in a channel with transverse fin arrays. International Journal of Numerical Methods for Heat & Fluid Flow, 10(8), pp. 842-861.

S.D.G.